Università degli Studi Roma TRE

e

Consorzio Nazionale Interuniversitario per le Scienze Fisiche della Materia

Dottorato di Ricerca in Scienze Fisiche della Materia
XXV ciclo

Resonant Bose-Fermi Mixtures:
a T-matrix and Quantum Monte Carlo Study

Tesi di dottorato di Elisa Fratini

Relatore
Dott. Pierbiagio Pieri

Coordinatore Dottorato
Prof. Settimio Mobilio

a. a. 2011/2012

E se dormiste, e se nel sonno sognaste,
e se nel sogno andaste in paradiso
e là coglieste un fiore strano e bellissimo
e se svegliandovi, aveste il fiore in mano?
Che direste allora?

S.T. Coleridge

Anche il viandante dal pendio della cresta del monte,
non porta a valle una manciata di terra,
terra a tutti indicibile, ma porta una parola conquistata,
pura, la genziana
gialla e blu. Forse noi siamo qui per dire: casa,
ponte, fontana, porta, brocca, albero da frutti, finestra,
al più: colonna, torre... Ma per dire comprendilo bene
oh, per dirle le cose così, che a quel modo, esse stesse,
nell'intimo,
mai intendevano d'essere.

R. M. Rilke, *Elegie duinesi, Nona elegia*

Contents

Introduction

At very low temperatures, when the thermal wavelength becomes comparable to the interparticle distance, the matter shows its quantum nature. In this quantum regime all the particles can be distinguished between bosons, obeying Bose-Einstein statistics, and fermions, obeying Fermi-Dirac statistics. These different statistics determine a very different behavior for bosons and fermions. At sufficiently low temperature, bosons condense in a single quantum state, with all particles sharing the same wave function. For fermions this is strictly forbidden by Pauli principle: two identical fermions cannot share the same wave function. The first phenomenon (Bose-Einstein condensation) is at the heart of superfluidity and superconductivity. Fermi statistics, on the other hand, is at the basis of the structure and stability of atoms and solids (in other words, of the world as we know it). Such quantum phenomena are the topics at the basis of the field of ultracold gases, in which this thesis work sets in.

There are several reasons behind the recent great interest in the ultracold gases. Ultracold quantum models and simulators allow to test theories and to address fundamental issues of quantum mechanics as well as to reproduce physical systems relevant to other areas in physics, with a flexibility and a degree of tunability of parameters unimaginable in the original system of interest. Furthermore ultracold gases offer the possibility to construct novel many-body systems, expanding the exploration of the quantum behavior of matter beyond what the physical world commonly shows in nature.

In this thesis we develop the theoretical study of a novel physical system, in the context of ultracold gases. We investigate the physical behavior of a resonant Bose-Fermi mixture,

namely, an ultracold gas made of both bosons and fermions, with a strong attractive interaction between these two components.

For weak attraction, the system is a weakly-interacting Bose-Fermi mixture: at sufficiently low temperature the bosons condense, while the fermions behave as a Fermi liquid, with a sharp Fermi surface determined by the fermion number; perturbative calculations in the BF coupling are possible in this regime [Viv02, Alb02]. For sufficiently strong attraction, instead, bosons and fermions pair into molecules. In particular, for a fermion density n_F larger than the boson density n_B one expects all bosons to pair with fermions: a boson condensate should be absent in such a regime and the system becomes a weakly interacting Fermi-Fermi mixture, with one component consisting of molecules, with density $n_M = n_B$, and the other component of unpaired fermions, with density $n_F - n_B$.

How does the system evolves at zero temperature between the two above physical regimes? Several scenarios could be imagined in principle:

(i) a continuous quantum-phase transition, with the condensate fraction vanishing smoothly at a certain critical value of the BF coupling;

(ii) a first-order quantum phase transition, with phase separation between a condensed phase and a molecular phase without condensate;

(iii) the collapse of the system in the intermediate coupling region, with no thermodynamically stable state connecting the two different regimes.

We study in detail such competing scenarios comparing the results obtained with two different theoretical approaches, a many-body diagrammatic approach (the T-matrix approximation) and Quantum Monte Carlo method. The T-matrix approximation is developed within the Green's function formalism. The Green's function diagrammatic theory allows to study a many-body problem beyond simple mean-field solutions or perturbative expansions, which are not reliable in the strongly interacting regime. The propagators are dynamical quantities, strictly connected to the observables describing the system rather than to its wave function and can be calculated to derive the thermodynamical properties both at finite and zero-temperature. The T-matrix plays the role of the many-body scattering matrix and

contains all the terms relevant to catch in a more intuitive way the physics of the system. On the other hand the Fixed-Node Quantum Monte Carlo method starts from a guess on the ground state wave function. The first result obtained is the energy, calculated making the system evolve with its Hamiltonian from a trail wave function to the ground state. The closer the trial wave function is to the real solution of the Schrödinger equation, the faster and more reliable the convergence to the ground-state energy. If the initial guess on the wave function is good, the Quantum Monte Carlo simulation allows to obtain the equation of state of the system, but not the exact ground-state wave function, even if we can assume that the trial wave function contains already the main features of the real solution of the problem.
Another important difference between the two approaches can be find in the calculation of the physical observables. The T-matrix approximation removes some terms (which are supposed to be negligible) in the Dyson expansion and allows to calculate directly using a particular collection of diagrams, the thermodynamic quantities. If the behavior of the system is well described by such approximated particle-propagators, the values of the thermodynamic quantities obtained can be considered very close to the exact ones. The mean values of the observables calculated by the Quantum Monte Carlo method in general may not be exact (unless the estimators are pure, as for the energy), but the system is supposed to evolve with its proper Hamiltonian towards the exact ground state. In our diagrammatic calculation we have restricted our equations to the normal phase, approaching the phase transition only from temperatures or couplings larger than the critical ones. The Quantum Monte Carlo study is developed at zero-temperature from the weak to the strong-coupling limit, providing a good description of the system both in the condensed and in the normal phase.

By using many-body diagrammatic methods we first obtain the finite-temperature phase diagram and the thermodynamic properties of the system. Developing the zero-temperature limit of the same Green's function formalism we study the effect of density and mass im-

balances for the Bose-Fermi mixture. For a vanishingly small boson density we derive the asymptotic expressions for the critical coupling in the limits of small and large mass ratios. These expressions are relevant also for the polaron-molecule transition in a strongly-imbalanced Fermi mixture, thus bridging two quite distinct physical systems. The analysis of the momentum distribution functions at sufficiently large density imbalances shows an interesting effect in the bosonic momentum distribution, due to the simultaneous presence of composite fermions and unpaired bosons. By using the corresponding retarded propagators we calculate the spectral weight functions and the dispersions of the bosons and of the fermions. We obtain a wide collection of single-particle intensity plots, for several values of the density and mass imbalances, which could be compared in the near future with experimental data, obtained e.g. with radio-frequency spectroscopy. The analysis of the spectral weight allows to understand the single-particle behavior, highlighting the role of interaction close to the quantum phase transition. While a fraction of fermions shows a coherent single-particle behavior and can still be considered as freely-propagating with an infinite lifetime, all the bosons are dressed by the interaction, with a finite lifetime.

We use for the first time the Quantum Monte Carlo method with Fixed-Node approximation to investigate resonant Bose-Fermi mixture, from weak to the strong boson-fermion attraction. Two different nodal surfaces are used as trial wave functions in the two regimes. We obtain the equation of state of a density imbalanced mixture and we observe the presence of the quantum phase transition through the crossing of the energies, calculated with their respective trial wave functions. By fitting the Quantum Monte Carlo data, we can write the expressions for the energy in the superfluid and in the normal phase. A phase diagram in the coupling and boson-fermion concentration variables is then derived and the occurrence of phase separation is discussed. We compare Quantum Monte Carlo results to T-matrix calculations, finding an interesting agreement between the two results for the bosonic momentum distribution.

This thesis is organized as follows: in chapter 1 we introduce the reader into the field of ultracold gases, paying particular attention to the phenomenon of Feshbach resonances and to the recent theoretical and experimental interest in Bose-Fermi mixtures. In chapter 2 the finite-temperature diagrammatic formalism within the T-matrix approximation is developed to describe resonant Bose-Fermi mixtures with different density and mass imbalances. The main results, as the condensation temperatures and the chemical potentials, are shown to elucidate the competition between pairing and condensation. Chapter 3 treats the zero-temperature limit of the previuos formalism and reports the results for the dependence of critical coupling on mass ratio and density imbalance, the corresponding chemical potentials and momentum distribution functions. In chapter 4 we calculate the zero-temperature bosonic and fermionic spectral weights and dispersions, for mixtures from the quantum critical point to the strong-coupling regime and with different density and mass imbalances. In chapter 5 the Quantum Monte Carlo method with Fixed-Node approximation is applied to a resonant Bose-Fermi mixture. The equation of state, the phase diagram and other interesting physical quantities are obatained and some conclusions about the quantum phase transition and the phase separation are explained. The results shown in chapters 2 and 3 of this thesis have been published in the papers [Fra10] and [Fra12], while the results reported in chapters 4 have yet to be published. The QMC study reported in chapter 5 (see the preprint [Ber12]) has been realized in collaboration with G. Bertaina, V. Savona (from the Institute of Theoretical Physics, Ecole Polytechnique Fédérale de Lausanne EPFL, Switzerland) and S. Giorgini (from INO-CNR BEC Center and Dipartimento di Fisica, Università di Trento, Povo, Italy). In particular my personal contribution in the development of this work was given by the choice of the trial wave functions and the derivation of the phase diagram.

Chapter 1

Ultracold Bose-Fermi mixtures

1.1 Ultracold Gases

The physics of ultracold gases studies atomic systems with low densities and temperatures: the particle density of a Bose-Einstein condensed atomic cloud is typically $10^{13} - 10^{15}\ cm^{-3}$ at temperatures of the order of the microkelvin. Three length scales define the physical regime of ultracold gases: the range of the interaction r_0, the mean interparticle distance $l \approx n^{-d}$ (where n is the particle density of a d-dimensional system) and the thermal de Broglie wavelength $\lambda_T = \sqrt{2\pi\hbar/mk_BT}$ (being k_B the Boltzmann constant, m the atomic mass and T the temperature).

The quantum degeneracy regime is achieved when $l \lesssim \lambda_T$ and the statistics of particles start to play a relevant role. The de Broglie wavelength λ_T represents the size of the wavepacket associated to a particle: when it becomes comparable to the interparticle distance, nearby particles are losing distinguishability and can no longer be described by the classical Maxwell-Boltzmann statistics.

The diluteness condition of the quantum gas is expressed by the inequality $r_0 \ll \lambda_T$ and the low temperature regime is reached when $r_0 \ll \lambda_T$. These two conditions guarantee universality in the description of the scattering of particles: the scattering problem does not depend on the features of the interatomic potential, but only on the lowest angular

momentum scattering length a. In this physical regime ultracold gases show interesting quantum phenomena, such as Bose-Einstein condensation and the superfluidity, depending on the nature of the gas components.

After the work of Bose on the statistics of photons, in 1925 Einstein, studying an ideal gas of non-interacting massive bosons, predicted the phenomenon of condensation, namely the existence of a new phase, below a certain critical temperature, in which a macroscopic fraction of the particles occupies the single-particle state with zero momentum. Only in 1995, this theoretical prediction was realized experimentally with the creation of the first Bose-Einstein condensate, in the laboratories of Boulder with atoms of ^{87}Rb and at MIT with ^{23}Na. The experimental discovery of Bose-Einstein condensation in trapped atomic clouds marked the beginning of a very rapid devolopment in the study of ultracold gases. The powerful methods for cooling alkali metal atoms by using laser and evaporative cooling, together with the improvements in the atomic trapping techniques, based the way to exploration of quantum phenomena in the new physical regime of ultracold gases. Furthermore interactions between atoms may be varied either by using different atomic species or, for species that have a Feshbach resonance, by changing the strength of an applied magnetic field. The possibility of tuning the interatomic interaction by varying the magnitude of the external magnetic field makes it possible to study experimentally also the regime where the scattering length is comparable to or much larger than the interparticle distance and the atomic cloud constitute a strongly-interacting many-body system.

1.2 Feshbach Resonances

In a multi-channel scattering problem the elastic scattering in one channel can be altered dramatically if there is a low-energy bound state in a second channel which is closed. This phenomenon is generally known as Feshbach resonance. It occurs when the total energy of two scattering particles in an open channel is approaching the energy of the bound state in the closed channel. Two particles in an open channel can scatter to an intermediate state in

a closed channel, which subsequently decays to give two particles in one of the open channels. This second-order process modifies the scattering length a, introducing terms of the type:

$$a \propto \frac{1}{E - E_{res}}, \tag{1.1}$$

where E is the energy of the particles in the open channel and E_{res} is the energy of a state in the closed channels. The closer the state of the bound energy is to the energy of the incoming particles in the open channels, the greater the effect of the coupling between channels on the scattering length. The energies of the atomic states can be varied by changing external parameters, such as the magnetic field, therefore these resonances make it possible to tune the effective interactions between atoms.

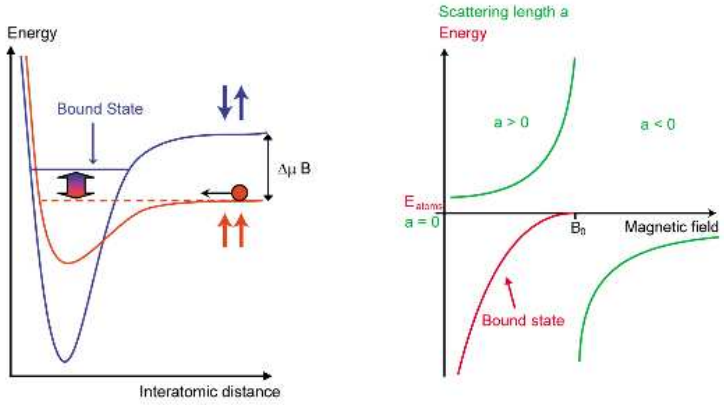

Figure 1.1: On the left: schematic plot of the potential energy curves for two different channels that illustrate the formation of the Feshbach resonance. On the right: curves of the scattering length and of the binding energy versus the external magnetic field.

We apply to the system an external magnetic field B and we call B_0 the value of the field at which the threshold energy of the open channel matches the bound-state energy in the closed channel. The magnetic moments of the two particles in the open channel are different from the magnetic moment of the bound-state in the closed one: by tuning the value of B it is possible to bring the bound-state energy closer to the threshold energy of the open

channel (see the left panel of Fig. 1.2). The expression for the scattering length in presence of a Feshbach resonance is given by:

$$a = a_{bg}\left(1 - \frac{\Delta B}{B - B_0}\right), \tag{1.2}$$

where a_{bg} is the background scattering length far from the resonance and ΔB is the width parameter. The scattering length a is changed by the resonance for variations of the magnetic field of the order of ΔB, which represents the width of the resonance. This parameter depends on the coupling between the channels and on the different magnetic moments in the channels. As we can see from the right panel of Fig. 1.2, for magnetic fields $B \gg B_0$ the scattering length assumes negative values close to zero: this means that it is possible to obtain a weakly-interacting system with no bound-states. From the expression 1.2 we observe that when $B = B_0$ the scattering length has a divergence. This particular part has been named the *unitarity limit* in the context of ultracold gases. When the magnetic field $B \ll B_0$, the scattering length is positive and small and the corresponding strong attractive interaction supports deep bound states with a binding energy $\epsilon_0 = 1/(2m_r a^2)$, where m_r is the reduced mass. This corresponds to the strongly-coupled Bose-Fermi mixture in the molecular limit.

1.3 Bose-Fermi Mixtures

The recent increasing interest in the field of the ultracold atomic gases started from the realization of the first Bose-Einstein Condensation in 1995, using a gas of Rubidium at the University of Colorado in Boulder [And95] and with atoms of Sodium at MIT [Dav95]. In the years that followed, the fascinating phenomenon of the Bose-Einstein Condensation was explored in great detail by a series of beautiful experiments. Later, looking for an analogous description in the field of the condensed matter and in particular for the electron gas, the focal point of the research in ultracold atoms spontaneously shifted from bosons to fermions. In the last years the introduction of a new technique exploiting the Feshbach resonances

has opened the possibility to tune the interaction between the atoms by simply controlling an external magnetic field applied to the system. Among the prominent results sprung from this powerful technique there are the achievement of BCS superfluidity in ultracold Fermi gases, the exploration of the BCS-BEC crossover, and the study of the properties of a strongly-interacting two-component Fermi gas. After an exploration of a rich variety of systems, entirely composed by the same species of bosons or fermions, today the attention is focusing on a new interesting kind of systems, the mixtures, which includes gases composed by bosons and fermions, or by bosons of two different atomic species, or by multi-component fermions (for example fermions of the same atomic species in two or more different hyperfine levels). Also in these new systems, thanks to Feshbach resonances, it is possible to tune the interaction between the different particles and a lot of experiments with mixtures of atoms are carried out at present. The first heteronuclear boson-fermion Feshbach molecules were obtained in Hamburg [Osp06] and later in Boulder [Zir08], with a Bose-Fermi mixture of ^{40}K-^{87}Rb in presence of a Feshbach resonance. At the same time, in Boulder [Pap06] and in Florence [Web08], boson-boson heteronuclear Feshbach molecules were obtained respectively with a ^{85}Rb-^{87}Rb and with a ^{41}K-^{87}Rb mixture. At this time two interesting experiments on resonant Bose-Fermi mixtures are carried out at MIT, with a mixture of ^{23}Na-^{6}Li [Heo12] and with a mixture of ^{23}Na-^{40}K [Wu12].

In the recent research works, the theory of the ultracold atomic mixtures is going hand in hand with the experiments. The initial works on boson-fermion or boson-boson mixtures studied mainly with a mean-field approach the problem of the instability (for collapse or phase-separation) of the systems. Non-resonant Bose-Fermi mixtures were initially studied theoretically and experimentally in Refs. [Viv00, Yi01, Alb02, Viv02, Rot02, Liu03, Lew04] and [Mod02], respectively. Then the following works started to consider what happens in presence of a Feshbach resonance and to study strongly interacting systems, approaching the problem in several ways: in the mean-field approximation or with the diagrammatic formalism or with fully numerical methods. Bose-Fermi mixtures in presence of a narrow Feshbach resonance were then considered in the theoretical works of Refs. [Pow05, Dic05,

Avd06, Bor08]. For a narrow resonance one has to take into account explicitly the molecular state forming in the closed channel, leading to a Hamiltonian which includes three different species (bosons, fermions, and molecules) from the outset.

Both cases of narrow or broad resonance are, however, relevant to current experiments in Bose-Fermi mixtures [Gun06, Osp06, Osp06b, Zir08, Ni08, Wu11, Park12, Heo12], depending on the mixture and/or the resonance actually chosen in the experiment. A broad Fano-Feshbach resonance is characterized by the smallness of the effective range parameter r_0 of the boson-fermion scattering amplitude with respect to both the average interparticle distance and the boson-fermion scattering length a [Sim05]. Under these conditions, the system can be described by a Hamiltonian made just by bosons and fermions mutually interacting via an attractive contact potential.

Initial works studying Bose-Fermi mixtures in the presence of a broad resonance focused on lattice models [Kag04, Bar08, Pol08, Riz08, Tit09, Mar09], or considered separable interactions, as inspired by nuclear-physics models [Sto05]. The continuum case in the presence of an attractive contact potential was first tackled in Ref. [Wat08], which concentrated on the thermodynamic properties of the condensed phase of a Bose-Fermi mixture at zero temperature.

A first study of the competition between Bose-Fermi pairing and boson condensation in a broadly resonant Bose-Fermi mixture has been presented in the first work by the author of this thesis [Fra10]. By using many-body diagrammatic theory, with a T-matrix approximation for the bosonic and fermionic self-energies, we were able to show that, for increasing Bose-Fermi attraction, the boson-fermion pairing correlations progressively reduce the boson condensation temperature and make it eventually vanish at a critical coupling above which the condensate is completely depleted (thus revealing the presence of a quantum phase transition at zero temperature). The development and the results of this study are described in chapter 2. In the following paper [Fra12], we extended the work of Ref. [Fra10] by analyzing the effect of a mass imbalance between the bosonic and fermionic species. The effect of mass imbalance in a broadly resonant Bose-Fermi mixture has been studied recently also in

Ref. [Lud11], within a path-integral approach which is complementary to our approach and that was limited to zero temperature only. A comparison between our results and those of Ref. [Lud11] will be discussed later on in chapter 3.

Before starting a detailed description of the calculations and results developed in this thesis' work, we will summarize how such great series of experimental and theoretical works address the issue of the evolution of the system from a weakly-interacting Bose-Fermi mixture to a weakly interacting Fermi-Fermi mixture (with molecules and unpaired fermions). As previously described in the introduction the three possible scenarios connecting the two above physical regimes are the occurrence of a continuous quantum-phase transition, of a first-order quantum phase transition or the collapse of the system.

Initial experiments [Mod02, Osp06c] with ultracold Bose-Fermi mixtures, as well as first theoretical studies [Viv00, Yi01, Rot02] of the problem supported the collapse scenario, with the instability occurring already for moderate BF coupling. In the first experiments, however, only a limited region of the parameter space was explored (e.g., a boson number N_B considerably greater than the fermion number N_F and given nonresonant values of the scattering lengths a_{BB} and a_{BF}). The first theoretical works, on the other hand, were based only on mean-field or perturbative results.

The continuous quantum-phase transition scenario was instead first supported by Ref. [Pow05], albeit within a "two-channel model" for the BF coupling that introduces further degrees of freedoms (the so-called closed-channel molecules) and parameters on top of the minimal set of parameters mentioned above (and which is relevant for ultracold-gas experiments with *narrow* Fano-Feshbach resonances [Gio08]). We will explore the same scenario for the single-channel model within a T-matrix diagrammatic approach, which focuses on the normal ("molecular") phase and finds its stability border with respect to the formation of a condensate, assuming the transition to be continuous. The alternative scenario of a first order transition, with a rather vast region of phase-separation occurring between the "molecular" region and the condensed one, was instead found in [Lud11] and in [Mar08] (for a broad resonance, with field-theoretic methods or a narrow resonance within mean-field, respectively).

A recent variational calculation has indicated finally that a sufficiently strong boson-boson (BB) repulsion should prevent the collapse scenario [Yu11].

Chapter 2

Competition between pairing and condensation in resonant Bose-Fermi mixtures: T-matrix approximation at finite temperature

As we have seen in section 1.3, resonant Bose-Fermi mixtures constitute an interesting class of novel systems in the recent scenario of ultracold gases. With the diagrammatic method introduced and developed in this chapter, we approach the study of a resonant Bose-Fermi mixture starting with a very simple model, in order to catch the essential features of the system and provide a qualitative analysis of its physical behavior. In particular, by calculating the condensation temperature, the chemical potentials and the momentum distributions in the normal phase, i.e. above the critical temperature, we address the issue of the competition between pairing and condensation.

2.1 T-matrix approximation

We consider a homogeneous mixture, composed by single-component fermions and bosons. The boson-fermion interaction is assumed to be tuned by a broad Fano-Feshbach resonance, as in most of current experiments on Bose-Fermi mixtures [Gun06, Osp06, Osp06b, Zir08, Ni08, Wu11, Park12]. Under this condition, the boson-fermion interaction can be adequately described by an attractive point-contact potential.

We consider then the the following (grand-canonical) Hamiltonian:

$$H = \sum_s \int d\mathbf{r}\psi_s^\dagger(\mathbf{r})(-\frac{\nabla^2}{2m_s} - \mu_s)\psi_s(\mathbf{r}) + v_0 \int d\mathbf{r}\psi_{\rm B}^\dagger(\mathbf{r})\psi_{\rm F}^\dagger(\mathbf{r})\psi_{\rm F}(\mathbf{r})\psi_{\rm B}(\mathbf{r}). \qquad (2.1)$$

Here $\psi_s^\dagger(\mathbf{r})$, creates a particle of mass m_s and chemical potential μ_s at spatial position $\mathbf{r}$, where s=B,F indicates the boson and fermion atomic species, respectively, while v_0 is the bare strength of the contact interaction (we set $\hbar = k_{\rm B} = 1$ throughout this thesis). As for two-component Fermi gases [Pie00], the ultraviolet divergences associated with the contact interaction in (2.1) are eliminated by expressing the bare interaction v_0 in terms of the boson-fermion scattering length a:

$$\frac{1}{v_0} = \frac{m_r}{2\pi a} - \int \frac{d\mathbf{k}}{(2\pi)^3}\frac{2m_r}{\mathbf{k}^2}\,, \qquad (2.2)$$

where $m_r = m_{\rm B}m_{\rm F}/(m_{\rm B} + m_{\rm F})$ is the reduced mass of the boson-fermion system.

We have not considered in the Hamiltonian (2.1) an explicit boson-boson interaction term. In the physical systems relevant to experiments, the corresponding nonresonant scattering length is normally small and positive. In the homogeneous and normal system we are going to consider, it yields then only a mean-field shift of the boson chemical potential. Note however that, according to the variational analysis of Ref. [Yu11], the assumption of having a homogeneous system actually requires the boson-boson scattering length to exceed a certain value, in order to guarantee the mechanical stability of the Bose-Fermi mixture against collapse. We thus implicitly assume to work in this stable regime. Note finally that a Fermi-Fermi $s-$wave scattering length is excluded by Pauli principle.

A natural length scale for the system is provided by the average interparticle distance $n^{-1/3}$ (where $n = n_{\rm B} + n_{\rm F}$ is the total particle-number density, $n_{\rm B}$ and $n_{\rm F}$ being the individual boson and fermion particle-number density, respectively). We thus introduce a fictitious Fermi momentum of the system $k_{\rm F} \equiv (3\pi^2 n)^{1/3}$ (as for an equivalent two-component Fermi gas with a density equal to the total density of the system), and use the dimensionless coupling parameter $g = (k_{\rm F} a)^{-1}$ to describe the strength of the interaction. In the weak-coupling limit, where the scattering length a is small and negative and $g \ll -1$, the two components behave essentially as Bose and Fermi ideal gases. In the opposite, strong-coupling, limit where a is small and positive and $g \gg 1$, the system is expected to be described in terms of composite fermions, i.e. boson-fermion pairs with a binding energy $\epsilon_0 = 1/(2m_r a^2)$, and excess fermions. We restrict our analysis to mixtures where the number of bosons never exceeds the number of fermions. This is because only in this case a quantum phase transition associated with the disappearance of the condensate is possible. In addition, mixtures with $n_{\rm B} > n_{\rm F}$ are expected to be severely affected by three-atom losses. Three-body losses are dominated by processes involving two bosons and one fermion with a rate proportional to $n_B^2 n_F$ [Zir08]. They can thus be controlled by keeping n_B sufficiently small with respect to n_F. A predominance of fermions should also reduce the tendency to collapse, because of the stabilizing effect of Fermi pressure. As a matter of fact, we have verified that the compressibility matrix $\partial\mu_s/\partial n_{s'}$ remained positive definite for all couplings, temperatures, and densities $n_F \geq n_B$ considered in our calculations. Apparently, pairing correlations act to protect the system from the mean field instabilities dominating the phase diagram of non-resonant Bose-Fermi mixtures.

The physical behavior of a Bose-Fermi mixture across all the resonance is captured by the T-matrix set of diagrams for the boson and fermion self-energies represented in Fig.2.1. In analogy with the BCS-BEC crossover problem in a two-component Fermi gas [Pie00], the choice of the self-energy diagrams will be guided by the criterion that a single set of diagrams should recover the correct physical description of the above two opposite limits. As we will show in the following section, this set of diagrams is able to recover the expected

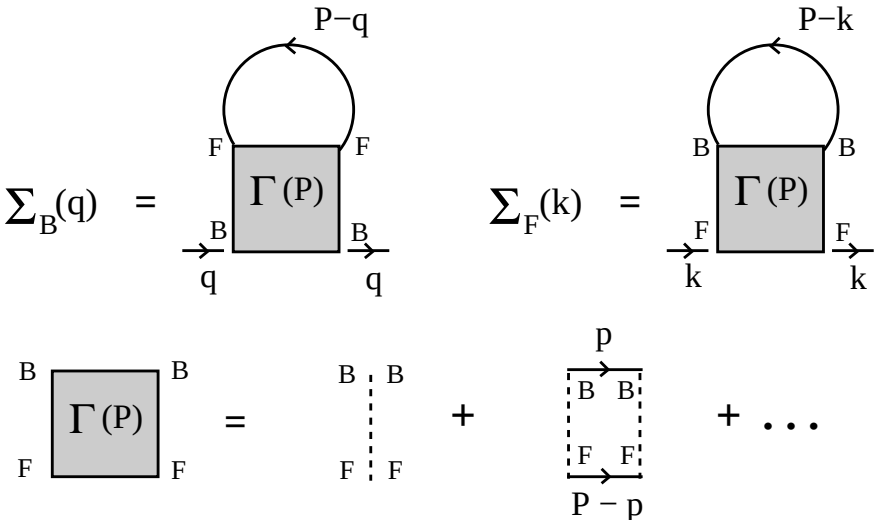

Figure 2.1: T-matrix diagrams for the bosonic and fermionic self-energies in the normal phase. Full lines represent bare bosonic (BB) and fermionic (FF) Green's functions. Broken lines represent bare boson-fermions interactions v_0.

physical behavior in both the weak- and strong-coupling limits, thus providing a meaningful theoretical framework for the whole resonance.

The corresponding equations for the bosonic and fermionic self-energies $\Sigma_{\rm B}$ and $\Sigma_{\rm F}$ and many-body $T-$matrix Γ read:

$$\Sigma_{\rm B}(q) = -T\int\frac{d\mathbf{P}}{(2\pi)^3}\sum_m G^0_{\rm F}(P-q)\Gamma(P), \tag{2.3}$$

$$\Sigma_{\rm F}(k) = T\int\frac{d\mathbf{P}}{(2\pi)^3}\sum_m G^0_{\rm B}(P-k)\Gamma(P), \tag{2.4}$$

$$\Gamma(\mathbf{P},\Omega_m) = -\left\{\frac{m_r}{2\pi a}+\int\frac{d\mathbf{p}}{(2\pi)^3}\times\left[\frac{1-f[\xi_{\rm F}(\mathbf{P}-\mathbf{p})]+b[\xi_{\rm B}(\mathbf{p})]}{\xi_{\rm F}(\mathbf{P}-\mathbf{p})+\xi_{\rm B}(\mathbf{p})-i\Omega_m}-\frac{2m_r}{\mathbf{p}^2}\right]\right\}^{-1}. \tag{2.5}$$

Here $q=(\mathbf{q},\omega_\nu)$, $k=(\mathbf{k},\omega_n)$, $P=(\mathbf{P},\Omega_m)$, where $\omega_\nu=2\pi\nu T$ and $\omega_n=(2n+1)\pi T$, $\Omega_m=(2m+1)\pi T$ are bosonic and fermionic Matsubara frequencies, respectively, (ν,n,m being integer numbers), while $f(x)$ and $b(x)$ are the Fermi and Bose distribution functions at temperature T, and $\xi_s(\mathbf{p})=\mathbf{p}^2/(2m_s)-\mu_s$.

The self-energies (2.3) and (2.4) determine the dressed Green's functions G_s via the Dyson's equation $G_s^{-1} = G_s^{0\,-1} - \Sigma_s$ (with the bare Green's functions given by $G_{\rm B}^0(q) = [i\omega_\nu - \xi_{\rm B}(\mathbf{q})]^{-1}$ and $G_{\rm F}^0(k) = [i\omega_n - \xi_{\rm F}(\mathbf{k})]^{-1}$). The dressed Green's functions G_s allow to calculate the boson and fermion momentum distribution functions through the equations:

$$n_{\rm B}(\mathbf{q}) = -T\sum_\nu G_{\rm B}(\mathbf{q},\omega_\nu)\, e^{i\omega_\nu 0^+} \tag{2.6}$$

$$n_{\rm F}(\mathbf{k}) = T\sum_n G_{\rm F}(\mathbf{k},\omega_n)\, e^{i\omega_n 0^+}\,, \tag{2.7}$$

which in turn determine the boson and fermion number densities:

$$n_{\rm B} = \int\frac{d\mathbf{q}}{(2\pi)^3} n_{\rm B}(\mathbf{q}) \tag{2.8}$$

$$n_{\rm F} = \int\frac{d\mathbf{k}}{(2\pi)^3} n_{\rm F}(\mathbf{k}). \tag{2.9}$$

At fixed densities and temperature, the two coupled equations (2.8) and (2.9) fully determine the boson and fermion chemical potentials, and therefore the thermodynamic properties of the Bose-Fermi mixture in the normal phase.

Coming from the normal phase, the condensation of bosons starts when the condition

$$\mu_{\rm B} - \Sigma_{\rm B}(q=0) = 0 \tag{2.10}$$

is first met. Eq. (2.10) corresponds to the requirement of a divergent occupancy of the boson momentum distribution at zero momentum: $\lim_{\mathbf{q}\to\mathbf{0}} n_{\rm B}(\mathbf{q}) = \infty$. [Pop87]

Analytic results can be obtained in the two opposite limits of the boson-fermion coupling. For weak-coupling $\Gamma(P) \simeq -\frac{2\pi a}{m_r}$, yielding $\Sigma_B \simeq \frac{2\pi n_F a}{m_r}$ and $\Sigma_F \simeq \frac{2\pi n_B a}{m_r}$, in accordance with the expected mean-field shifts. For strong-coupling $\Gamma(P)$ gets instead proportional to the molecular propagator:

$$\Gamma(P) \simeq -\frac{2\pi}{m_r^2 a}\frac{1}{i\Omega_m - \frac{\mathbf{P}^2}{2M} + \mu_M} \tag{2.11}$$

where $\mu_M \equiv \mu_B + \mu_F + \epsilon_0$ defines the molecular chemical potential and $M = m_B + m_F$. Insertion of this propagator in Eqs. (2.3−2.9) leads, for $n_B < n_F$, to $\mu_M \simeq (6\pi^2 n_B)^{2/3}/2M$, $\mu_F \simeq [6\pi^2(n_F - n_B)]^{2/3}/2m_F$ and $\mu_B \simeq -\epsilon_0$, as expected when all bosons pair with fermions.

For intermediate values of the boson-fermion coupling Eqs. (2.3−2.9) need to be solved numerically. The results for the condensation critical temperature T_c versus the boson-fermion dimensionless coupling $(k_F a)^{-1}$ and the corresponding chemical potentials and momentum distribution functions are presented in the following sections.

2.2 Critical temperature for density and mass imbalanced mixtures

The theoretical approach developed in section 2.1 can be used to explore the normal phase of a homogeneous Bose-Fermi mixture at arbitrary values of boson and fermion masses and densities. In this section, where we present finite-temperature results, we consider two possible cases: a mixture with balanced masses ($m_B = m_F$) and a system with a specific mass ratio $m_{\rm B}/m_{\rm F} = 87/40$, relevant for the ^{87}Rb $-^{40}$K mixture. More general mass ratios will be considered at zero temperature.

Mass balanced mixtures The results for the condensation critical temperature T_c versus the boson-fermion dimensionless coupling $(k_F a)^{-1}$ are presented in Fig.2.2 for a mixture with $m_B = m_F$ at several values of density imbalance. All curves start in weak-coupling from the corresponding noninteracting values, and decrease monotonically for increasing coupling due to the growing pairing correlations, which tend to deplete the zero momentum mode and distribute the bosons over a vast momentum region, as required to build the internal molecular wave-function. The critical temperature vanishes eventually at a critical coupling, corresponding to a quantum critical point which separates a phase with a condensate from a phase where molecular correlations are so strong to deplete the condensate completely.

Remarkably, the critical coupling value depends very weakly on the degree of density imbalance: all curves terminate in the narrow region $1.6 < (k_F a)^{-1} < 1.8$. In this respect, it is interesting to consider the limit $n_B \to 0$, where the critical coupling can be calculated independently by solving the problem of a single boson immersed in a Fermi sea. This is

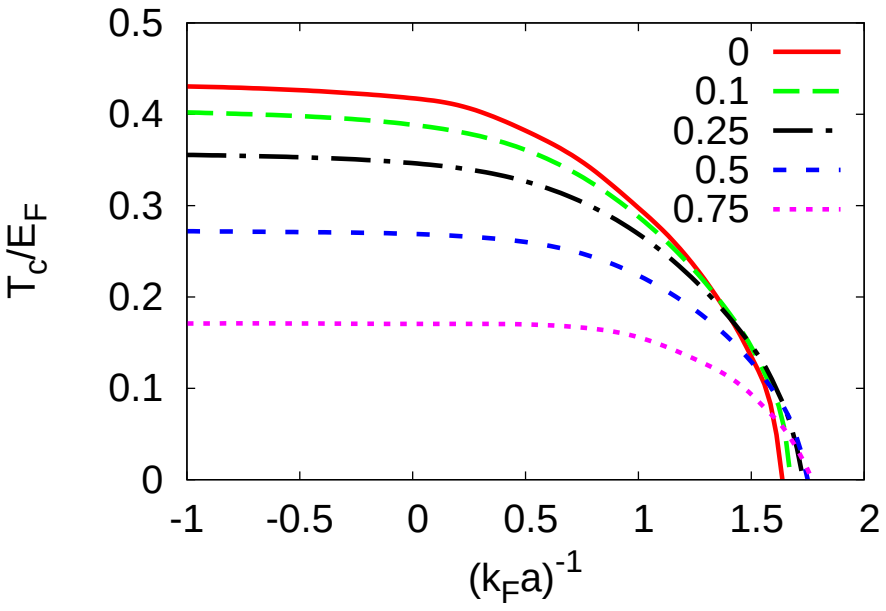

Figure 2.2: Critical temperature (in units of $E_F = k_F^2/2m_F$) for condensation of bosons vs the boson-fermion coupling $(k_F a)^{-1}$ for different values of the density imbalance $(n_F - n_B)/n$ in a mixture with $m_B = m_F$.

actually the same as a spin-down fermion sorrounded by a Fermi sea of spin-up fermions, since for a single particle the statistics is immaterial. The critical coupling reduces thus to that for the polaron-to-molecule transition, recently studied in the context of strongly imbalanced *two-component Fermi gases* [Pro08, Vei08, Com09, Sch09]. In particular, we have verified analytically that our equations coincide in this limit with those of [Com09] for the polaron-to-molecule transition, yelding the value $(k_F a)^{-1} = 1.60$ for the critical coupling calculated within a corresponding T-matrix approximation. Quantum Monte Carlo calculations [Pro08] and refined diagrammatic approximations [Com09] for the single spin-down problem yield the value $(k_F a)^{-1} = 1.11$ for the polaron-to-molecule transition, a 30% off the T-matrix prediction. This difference is due to the overestimate of the molecule-fermion repulsion by the T-matrix approximation, which yields $8/3a$ for the molecule-fermion scattering length

in place of the exact value $1.18a$ [Sko56], thus making the molecule formation in a Fermi sea environment less convenient. The value 1.60 for the critical coupling in the limit $n_B \to 0$ is reached with a weak reentrant behavior of the critical coupling vs. imbalance, occurring at imbalances larger than those reported in Fig. 2.2. For instance, at imbalance 0.95, T_c vanishes at $(k_F a)^{-1} \simeq 1.63$. The meeting of the properties of a Bose-Fermi mixture with those of a two-component Fermi mixture at this point of the phase diagram is quite remarkable, especially because this "universal" point sets the scale for the quantum phase transition for *all* boson densities $n_B \leq n_F$. The problem of the one-boson limit will be discussed in detail in section 3.4.

Mass imbalanced mixtures Figure 2.3 presents the dependence of the condensation critical temperature on the boson-fermion coupling $(k_{\rm F}a)^{-1}$ for a ^{87}Rb $-^{40}$K mixture, at different values of the density imbalance $(n_{\rm F} - n_{\rm B})/(n_{\rm F} + n_{\rm B})$. The critical temperature was obtained by solving numerically Eqs. (2.3)-(2.9), supplemented by the condition (2.10), while the ending point at $T = 0$ was calculated independently by solving the equations (3.1)-(3.6) (with the condition (2.10) defining now the critical coupling g_c at zero temperature). The matching between finite-temperature and zero-temperature results confirms the validity of the equations derived in the zero-temperature limit (see section 3.1), while providing simultaneously a check of the numerical calculations.

The overall behavior of the critical temperature as a function of coupling is similar to what found for equal masses. The critical temperature starts from the noninteracting value ($T_0 = 3.31 n_{\rm B}^{2/3}/m_{\rm B}$) in the weak-coupling limit and eventually vanishes at a critical coupling g_c, when the effect of the boson-fermion coupling is so strong that the Bose-Einstein condensate is completely depleted, in favor of the formation of molecules. The weak dependence of the critical coupling on the density imbalance previously found for equal masses is confirmed also for this case with different masses. In this case, the critical coupling varies in the range $1.3 \div 1.4$, to be compared with the range $1.6 \div 1.8$ found for $m_{\rm B} = m_{\rm F}$.

A minor difference with respect to the case with equal masses is finally the presence of a

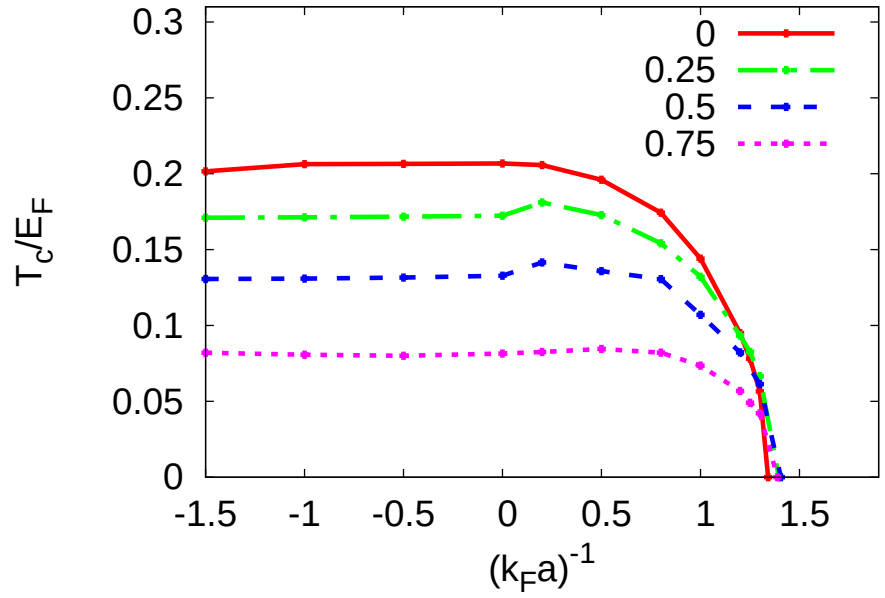

Figure 2.3: Critical temperature (in units of $E_{\rm F} = k_{\rm F}^2/2m_{\rm F}$) for condensation of bosons as a function of the boson-fermion coupling $(k_{\rm F}a)^{-1}$ for different values of the density imbalance $(n_{\rm F} - n_{\rm B})/(n_{\rm F} + n_{\rm B})$ in a mixture with $m_{\rm B}/m_{\rm F} = 87/40$.

weak maximum in the critical temperature, which reaches a value slightly above the noninteracting value T_0 before its final decrease. This feature is more pronounced for intermediate values of the density imbalance. We attribute this feature to the delicate balance between the effects of the boson-fermion interaction on the boson dispersion, and the condensate depletion due to molecular correlations. The boson dispersion may in fact be hardened by the interaction (similarly to what one finds for a dilute repulsive Bose gas [Hol03]), thus leading to an increase of the critical temperature. The predominance of one effect over the other one depends on a fine tuning of the mass ratio and density imbalance, and may explain the different behavior found for different values of these parameters.

2.3 Chemical potentials and momentum distribution functions

Chemical potentials The chemical potentials μ_B and μ_F for the mass balanced mixture at the critical temperatures of Fig. 2.2 are reported in Fig. 2.4 as a function of $(k_F a)^{-1}$, for different values of the density imbalance. The two chemical potentials behave quite differently. The fermion chemical potential remains almost constant in the whole range of coupling considered; the boson chemical potential, on the other hand, diminishes quite rapidly with increasing coupling while depending little on the density imbalance. This different behavior results from the concurrence of several factors. For weak-coupling, the increasing (negative) mean-field shift of the fermion chemical potential for increasing coupling is partially compensated by the decrease of the temperature when moving along the critical line. On the molecular side, the fermion chemical potential is instead determined by the Fermi energy of the unpaired fermions plus a mean-field shift caused by interaction with molecules. Pauli repulsion makes this interaction repulsive [Kag04] thus keeping the fermion chemical potential positive. The boson chemical potential, on the other hand, interpolates between the mean-field value $2\pi n_F a/m_r$ in weak coupling and $\mu_B \approx -\epsilon_0$ in strong coupling, as required by molecule formation.

Figure 2.5 reports the coupling dependence of the chemical potentials $\mu_{\rm B}$ and $\mu_{\rm F}$ at the critical temperature for a ^{87}Rb $-^{40}$K mixture at the same values of the density imbalance considered in Fig. 2.3. In this case, the critical boson and fermion chemical potentials present the same qualitative behavior already found for a mixture with equal masses. The boson chemical potential decreases markedly with increasing coupling, and changes from $\mu_{\rm B} \approx 2\pi n_{\rm F} a/m_r$ for weak coupling to $\mu_{\rm B} \approx -\epsilon_0$ for strong coupling, with a small dependence on the density imbalance. The fermion chemical potential (reported in the inset) remains instead almost constant across the whole resonance. The decrease of the chemical potential due to the attractive interaction with the bosons is, in fact, partially compensated

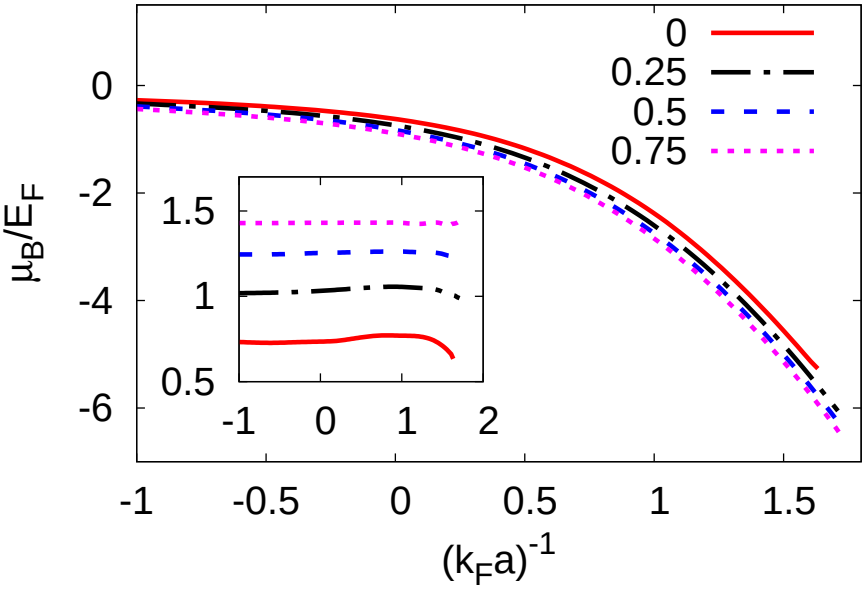

Figure 2.4: Boson chemical potential at the critical temperature T_c (in units of E_F) vs the boson-fermion coupling $(k_F a)^{-1}$ for different values of the density imbalance $(n_F - n_B)/n$ in a mixture with $m_B = m_F$. The corresponding fermion chemical potential is reported in the inset.

by the decreasing of the temperature when moving along the critical line (which increases μ_F) and by the Pauli repulsion between unpaired fermions and Bose-Fermi pairs.

Momentum distribution functions Figure 2.6 reports the momentum distributions $n_B(\mathbf{k})$ and $n_F(\mathbf{k})$ (as obtained before momentum integration in Eqs. (2.8)-(2.9)) at T_c, for a mixture with $m_B = m_F$ and $n_B = n_F$, at the coupling value $(k_F a)^{-1} = 1.63$ (approximately at the quantum critical point). The two distributions are markedly different at low momenta, consistently with their different statistics, but coalesce into the same behavior just after the step in the fermion momentum distribution. This common behavior corresponds to the function $n_M |\phi(\mathbf{k})|^2$ (dashed line in Fig.2.6), where $\phi(\mathbf{k}) = (8\pi a^3)^{1/2}/(\mathbf{k}^2 a^2 + 1)$ is the normalized two-body internal wave function of the molecules, while the coefficient n_M represents

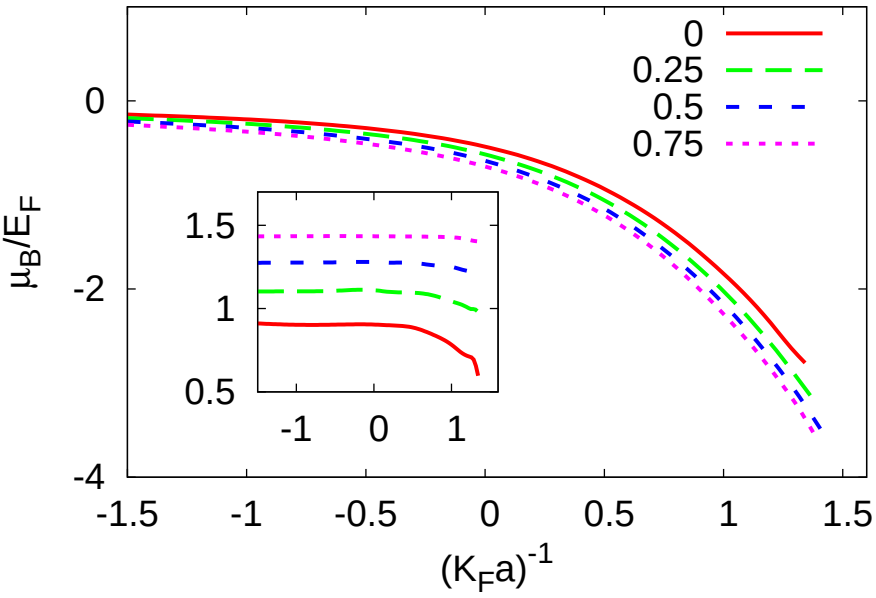

Figure 2.5: Bosonic chemical potential at the critical temperature T_c as a function of the boson-fermion coupling $(k_{\mathrm{F}}a)^{-1}$ for different values of the density imbalance $(n_{\mathrm{F}}-n_{\mathrm{B}})/(n_{\mathrm{F}}+n_{\mathrm{B}})$ in a mixture with $m_{\mathrm{B}}/m_{\mathrm{F}} = 87/40$. The corresponding fermionic chemical potential is reported in the inset.

their density. In the present case $n_M = 0.89\, n_B$, showing that a fraction of bosons remains unpaired but still does not condense even at such a low temperature. The extrapolation of these results at exactly zero temperature seems to indicate the existence (in a coupling range starting right after the quantum critical point) of quite an unconventional Bose liquid, corresponding to the unpaired bosons, which do not condense even at zero temperature. As we will see in the following chapter, the zero-temperature calculation of the contact constant suggests that the presence of this unexpected fraction of not condensed bosons might be fictious. We explain this result as an effect of the use of the strong-coupling approximation in the region of critical couplings, where the system has not yet completely reached the strong-coupling regime. The fraction of unpaired fermions is instead more conventional and

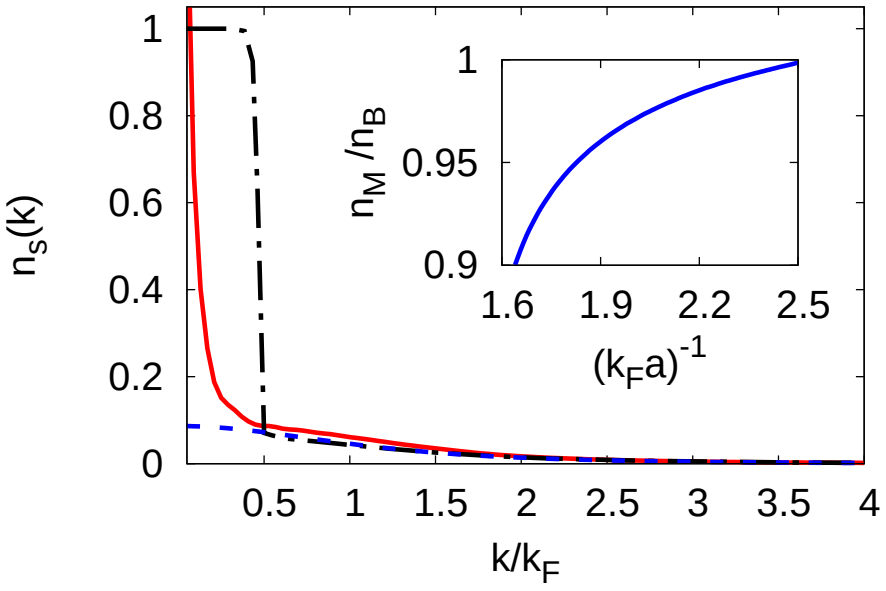

Figure 2.6: Boson (full line) and fermion (dashed-dotted) momenta distribution curves for $n_B = n_F$, $m_B = m_F$, $(k_F a)^{-1} = 1.63$ and $T = T_c \simeq 0.015 E_F$. See text for the meaning of the dashed curve. The inset reports the fraction of molecules vs $(k_F a)^{-1}$ for the same mixture at $T = 0.1 E_F$.

consists in a Fermi liquid, which is responsible for the jump in the fermion momentum distribution. In particular, the position of the jump in Fig. 2.6 at $|\mathbf{k}| \simeq 0.47\, k_F$, corresponds to an "enclosed" density of $0.10\, n_F$, in good numerical agreement with the value $0.11\, n_F$ obtained from the Luttinger theorem [Lut60] for the fraction $(n_F - n_M)$ of unpaired fermions (using the value $n_M = 0.89\, n_B$ extracted independently above). Note finally that the number of unpaired bosons progressively decreases by increasing the coupling, as expected on physical grounds, reaching eventually a 100% conversion of bosons into molecules, as shown in the inset of Fig. 2.6, where the ratio n_M/n_B is reported vs coupling at a constant temperature.

Chapter 3

Quantum Phase Transition in resonant Bose-Fermi mixtures: zero-temperature limit of the T-matrix approach

The behavior of the critical temperature as a function of the boson-fermion coupling discussed in the section 2.2, evidenced the presence of a quantum phase transition at zero temperature associated with a transition between a superfluid phase with a boson condensate to a normal phase, where the condensate is completely depleted. In this chapter we examine in more detail this quantum phase transition by solving numerically the equations formulated at exactly zero temperature.

3.1 The zero-temperature limit

We pass now to consider the zero-temperature limit of the previous finite-temperature formalism of the section 2.1. When $T \to 0$, the spacing $2\pi T$ between two consecutive Matsubara frequencies tends to zero. The sums over discrete Matsubara frequencies can then be replaced by integrals over continuous frequencies, provided the corresponding integrands are not too singular [Fet71, Lut60]. Problems in the replacement of the frequency sums with integrals,

in the zero-temperature limit, normally arise in the presence of double (or higher) poles of the summands in the complex frequency plane. We have not met these type of singularities in our case. In any case, the good matching of the finite temperature results with those obtained at zero temperature verify *a posteriori* the validity of the procedure.
We have then the equations

$$\Sigma_{\rm B}(q) = -\int\frac{d\mathbf{P}}{(2\pi)^3}\int\frac{d\Omega}{2\pi}G^0_{\rm F}(P-q)\Gamma(P) \tag{3.1}$$

$$\Sigma_{\rm F}(k) = \int\frac{d\mathbf{P}}{(2\pi)^3}\int\frac{d\Omega}{2\pi}G^0_{\rm B}(P-k)\Gamma(P), \tag{3.2}$$

for the bosonic and fermionic self-energies, where $q=(\mathbf{q},\omega_{\rm B})$, $k=(\mathbf{k},\omega_{\rm F})$, $P=(\mathbf{P},\Omega)$ while the frequencies $\omega_{\rm B}$, $\omega_{\rm F}$ and Ω are now continuous variables.

Similarly, the equations (2.6) and (2.7) for the momentum distribution functions are changed to

$$n_{\rm B}(\mathbf{q}) = -\int\frac{d\omega_{\rm B}}{2\pi}G_{\rm B}(\mathbf{q},\omega_{\rm B})e^{i\omega_{\rm B}0^+} \tag{3.3}$$

$$n_{\rm F}(\mathbf{k}) = \int\frac{d\omega_{\rm F}}{2\pi}G_{\rm F}(\mathbf{k},\omega_{\rm F})e^{i\omega_{\rm F}0^+}, \tag{3.4}$$

from which the number densities can be calculated as before.

A closed-form expression can be finally derived for the many-body T-matrix $\Gamma(P)$ at zero temperature, when the Fermi and Bose distribution functions appearing in Eq. (2.5) are replaced by step functions. We report in particular the expression for $\Gamma(P)$ when $\mu_{\rm F}>0$ and $\mu_{\rm B}<0$, which is in practice the only one relevant to our calculations at zero temperature.

We have

$$\Gamma(P) = -\left[\frac{m_r}{2\pi a} - \frac{m_r^{\frac{3}{2}}}{\sqrt{2}\pi}\sqrt{\frac{\mathbf{P}^2}{2M}-2\mu-i\Omega} - I_{\rm F}(P)\right]^{-1}, \tag{3.5}$$

where we have defined $M=m_{\rm B}+m_{\rm F}$ and $\mu=(\mu_{\rm B}+\mu_{\rm F})/2$, while $I_{\rm F}(P)$, which results from the integration of the term with the Fermi function in Eq. (2.5), is given by

$$\begin{aligned} I_{\rm F}(P) &= \frac{m_{\rm B}\left(k^2_{\mu_{\rm F}}-k^2_{\mathbf{P}}-k^2_\Omega\right)}{8\pi^2|\mathbf{P}|}\ln\left[\frac{(k_{\mu_{\rm F}}+k_{\mathbf{P}})^2-k^2_\Omega}{(k_{\mu_{\rm F}}-k_{\mathbf{P}})^2-k^2_\Omega}\right] \\ &- \frac{m_r k_\Omega}{4\pi^2}\left\{\ln\left[\frac{(k_{\mu_{\rm F}}+k_\Omega)^2-k^2_{\mathbf{P}}}{k^2_{\mathbf{P}}-(k_{\mu_{\rm F}}-k_\Omega)^2}\right]-i\pi{\rm sgn}(\Omega)\right\}+\frac{m_r k_{\mu_{\rm F}}}{2\pi^2}, \end{aligned} \tag{3.6}$$

where $k_{\mu_{\rm F}} \equiv \sqrt{2m_{\rm F}\mu_{\rm F}}$, $k_{\mathbf{P}} \equiv \frac{m_{\rm F}}{M}P$, while

$$k_\Omega \equiv (2m_r)^{\frac{1}{2}}\sqrt{-\frac{\mathbf{P}^2}{2M}+2\mu+i\Omega}. \tag{3.7}$$

Equations (3.1)-(3.6) determine the thermodynamic properties of a Bose-Fermi mixture at zero temperature in the absence of boson condensation. They are thus relevant for a sufficiently strong coupling g, such that the system remains in the normal phase even at zero temperature. In particular, upon lowering the coupling constant g, the condensation will start at a critical coupling g_c, when the condition (2.10) is first satisfied.

3.2 The quantum critical point (QCP): density and mass imbalance effect

Figure 3.1 reports the critical coupling g_c as a function of the mass ratio $m_{\rm B}/m_{\rm F}$, with two distinct panels for the cases $m_{\rm B}/m_{\rm F} \leq 1$ and $m_{\rm B}/m_{\rm F} \geq 1$. The different curves reported in Fig. 3.1 correspond to different values of the density imbalance, ranging from the density-balanced case to the fully imbalanced one $(n_{\rm F}-n_{\rm B})/(n_{\rm F}+n_{\rm B}) = 1.0$, which represents the system with just one boson immersed in a Fermi sea. This is actually the same as a spin-down fermion sorrounded by a Fermi sea of spin-up fermions, since for a single particle the statistics is irrelevant. The critical coupling reduces thus to that for the polaron-to-molecule transition, recently studied in the context of strongly imbalanced two-component Fermi gases [Pro08, Vei08, Mas08, Mor09, Pun09, Com09, Sch09]. The equations governing the one boson limit are reported in the section 3.4

The critical coupling is strongly influenced by the mass ratio, especially for $m_{\rm B}/m_{\rm F} < 1$. In this case, for all values of the density imbalance, g_c increases very rapidily as $m_{\rm B}/m_{\rm F}$ is decreased. For the single boson problem, an asymptotic expansion of the equations deter-

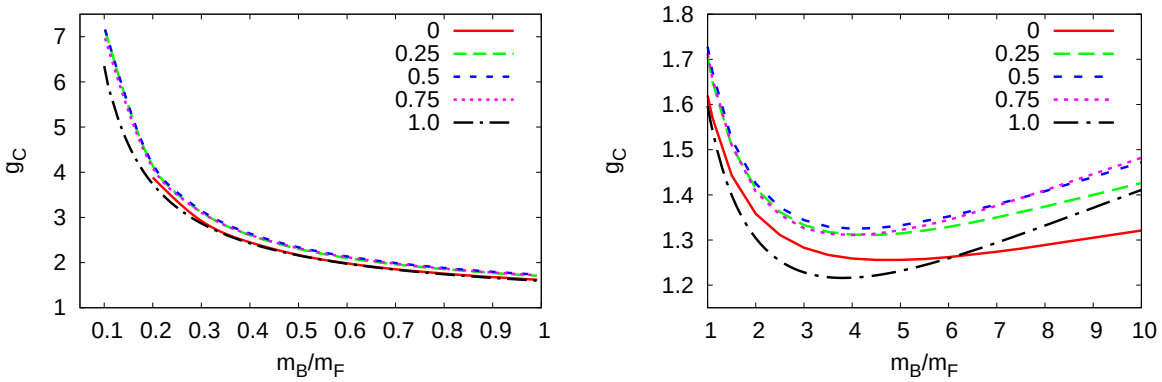

(a) $m_{\rm B}/m_{\rm F} \leq 1$ (b) $m_{\rm B}/m_{\rm F} \geq 1$

Figure 3.1: Critical coupling g_c as a function of the mass ratio $(m_{\rm B}/m_{\rm F})$ for different values of the density imbalance $(n_{\rm F} - n_{\rm B})/(n_{\rm F} + n_{\rm B})$. Panels (a) and (b) correspond to the ranges $m_{\rm B}/m_{\rm F} \leq 1$ and $m_{\rm B}/m_{\rm F} \geq 1$, respectively.

mining g_c for $m_{\rm B}/m_{\rm F} \to 0$ yields the result

$$g_c \approx \frac{4 \cdot 2^{1/3}}{3\pi}\frac{m_{\rm F}}{m_{\rm B}} + \frac{32 \cdot 2^{1/3}}{15\pi} \tag{3.8}$$

$$\approx 0.535\frac{m_{\rm F}}{m_{\rm B}} + 0.856 \tag{3.9}$$

which proves quite accurate even before the asympotic regime is reached (the deviation from the numerical solution is 15% for $m_{\rm B}/m_{\rm F} = 1$ and 2% for $m_{\rm B}/m_{\rm F} = 0.1$). [See the section 3.4 for the details of the derivation of Eq. (3.8).]

The rapid increase of the critical coupling for the polaron-to-molecule transition when $m_\downarrow \to 0$ was already noticed in Ref. [Com09], even though no asymptotic expression was reported there. Note however that, according to the analysis of the polaron-to-molecule transition of Ref. [Mat11], for a mass ratio $m_\downarrow/m_\uparrow \lesssim 0.15$ the molecular state acquires a finite momentum in its ground state. Similar results were obtained in Ref. [Song11]. The equations for the single boson problem here adopted assume that the formation of the molecule occurs at zero center of mass momentum (as in Refs. [Pro08, Vei08, Mas08, Mor09, Pun09, Com09, Sch09]). The curve corresponding to the single boson problem in Fig. 3.1 may thus change

for $m_B/m_F \lesssim 0.15$, after taking into account the possibility of pairing at finite momentum. We expect however this change to be minor on the basis of our calculations with a finite boson density, which allow for pairing at finite momentum and yield results close to the single-boson curve also for $m_B/m_F < 0.15$.

Note further that the study of the three body system with two equal fermions with mass m_F and one different particle with mass m_B interacting through a zero-range potential, shows that for $m_B/m_F < 0.0735 = (13.607)^{-1}$ the system is unstable due to a sequence of three-body bound states with energy $\to -\infty$ [Bra06]. A similar instability is expected to occur also in the many-body system with N equal fermions plus one different particle (a recent work has proven indeed that the above critical value for the three-body system provides a lower bound for the location of the instability in the many-body system [Cor12]). We note, however, that the unboundness from below of the Efimov spectrum (and the associated global instability) occurs only for a pure zero-range interaction. In a real system, physical two-body interactions will provide a natural cut-off at distances of the order of the van-der-Waals length r_{vdW}, thus limiting the position of the lowest Efimov level at an energy $\sim -1/r_{vdW}^2$. The global mechanical instability is thus avoided by the real system, even though the presence of Efimov states is expected to lead to an enhancement of three-body losses when they lie close to the three-particle or atom-dimer continuum. We further note in this context that the presence of the (non-universal) three-body bound-states recently found by Kartavtsev and Malykh [Kar07] for $(8.2)^{-1} > m_B/m_F > (13.607)^{-1}$ could also lead to enhanced three-body losses in this mass-ratio range.

We observe in any case that since our calculations were taken for $m_B/m_F \geq 0.1$ ($m_B/m_F \geq 0.2$ for equal densities, due to numerical difficulties), the above three-body effects (which are out of the scope of the present theory) should affect our study only marginally.

Consistently with our previous results, we observe a weak dependence of g_c on the density imbalance. Such a weak dependence on the densities remains valid also for $m_B > m_F$. In this case, all curves reach a minimum value of g_c ($=1.2\div1.3$) for mass ratios m_B/m_F in the range $3.5\div5$, after which they increase slowly with the mass ratio. For the single boson problem

with a large mass we have obtained the asymptotic expression (see section 3.4):

$$g_c \approx A(m_{\rm B}/m_{\rm F}) - \frac{2^{2/3}}{A(m_{\rm B}/m_{\rm F})} + \frac{16}{3\pi}\frac{1}{A(m_{\rm B}/m_{\rm F})^2} \tag{3.10}$$

where

$$A(m_{\rm B}/m_{\rm F}) = \frac{2^{4/3}}{\pi}\left(\ln\frac{4m_{\rm B}}{m_{\rm F}} - 2\right). \tag{3.11}$$

One can see from Eqs. (3.10) and (3.11) that at large mass ratios g_c increases very slowly, with a logarithmic dependence on the mass ratios. Due to this log-dependence the leading behavior, $g_c \approx (2^{4/3}/\pi)\ln\frac{4m_{\rm B}}{m_{\rm F}}$, is reached only at extremely large mass ratios. Equation (3.10), which includes the first two corrections to the leading behavior, provides a better approximation, the deviation from the numerical solution being 15% for $m_{\rm B}/m_{\rm F} = 20$ and 1.5% for $m_{\rm B}/m_{\rm F} = 100$.

The increasing behavior of g_c at both small and large mass ratios implies the existence of a minimum in the curve for g_c at intermediate mass ratios, consistently with the results of Fig. 3.1. Note however that in earlier work for the polaron-molecule transition, the critical coupling for the transition was found to move away from the BEC limit for increasingly heavier impurities. In particular, Ref. [Com09] reported that the critical coupling should approach the unitary limit for an infinitely heavy impurity. Similar results were also found in two-dimensions by M. Parish [Par11] (with the critical coupling approaching the weak-coupling limit in this case). A reason for such a difference may be that our theory in the limit of a single boson reduces to the "first level approximation" of Ref. [Com09], with no particle-hole dressing of the molecule (while the polaron is described with the same accuracy obtained with the variational wave-function introduced by Chevy [Che06], which is deemed quite accurate for the polaron energy [Com09]). The "second level approximation" of Ref. [Com09] includes instead a particle-hole dressing of the molecule. This inclusion is sufficient to recover in the strong-coupling limit the correct dimer-fermion scattering length, and shifts the position of the critical coupling for equal masses from the value $(k_{\rm F}a)^{-1} = 1.27c(= 1.60)$ to the value $0.88c(= 1.11)$ (the factor $c = 2^{1/3}$ appears here because of a different definition of $k_{\rm F}$ between us and the above references). The eventual (slow) increase of g_c at large mass

ratios could then be an artifact of the "first order approximation". Calculations at large mass ratios with alternative methods (such as fixed-node or diagrammatic Quantum Monte-Carlo methods) could definitively clarify this issue.

At equal densities, our results for g_c as a function of the mass ratio agree well with the results reported in Ref. [Lud11] for the same case. This is because the equations used in Ref. [Lud11] for calculating g_c correspond, in a diagrammatic formalism, to the same choice of the self-energy as ours, but with the Dyson's equation expanded: $G = G_0 + G_0 \Sigma G_0$, instead of $G^{-1} = G_0^{-1} - \Sigma$. Even though such an expansion is justified only when Σ is small, apparently it leads only to minor differences in the values for g_c. For instance, for equal masses and densities we obtained $g_c = 1.62$, to be compared with $g_c = 1.66$ in Ref. [Lud11].

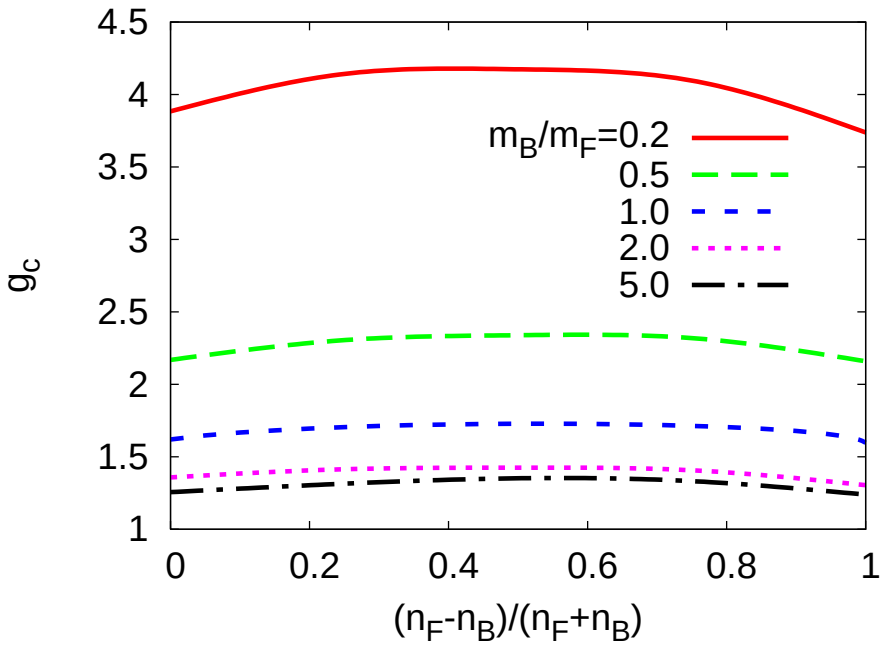

Figure 3.2: Critical coupling g_c as a function of the density imbalance $(n_\mathrm{F} - n_\mathrm{B})/(n_\mathrm{F} + n_\mathrm{B})$, for different values of the mass ratio $m_\mathrm{B}/m_\mathrm{F}$.

According to the analysis of Ref. [Lud11], however, only for sufficiently large values of the boson-boson scattering length a_B, the critical coupling g_c lies in a stable region of the

phase diagram. For small values of a_{B}, the second-order quantum phase transition between a condensed phase and a normal phase is in fact superseded by a phase separation between the two phases. According to our calculations, the compressibility matrix $\partial n_s/\partial \mu_{s'}$ is always positive in the normal phase, indicating that the second order phase transition here explored lies, at worst, in a metastable region of the phase diagram. In order to examine its absolute stability within our approach, one should extend our study to the superfluid phase and make a comparison of the free energies for the normal and superfluid phases. We observe however, that if ratios a_{B}/a of the order of 0.2-0.3 are sufficient to suppress phase separation in most of the phase diagram (as the results of Ref. [Lud11] seem to indicate), then the effect of a_{B} on g_c will be minor. In chapter 5 a phase diagram for the resonant Bose-Fermi mixture is obtained thanks to the Quantum Monte Carlo simulations. The discussion about the nature of the present quantum phase transition and the existence of a separated phase, will be developed in chapter 5.

The weak dependence of the critical coupling on the density imbalance is emphasized in Fig. 3.2, which presents g_c as a function of the density imbalance for some representative values of the mass ratio $m_{\mathrm{B}}/m_{\mathrm{F}}$. All curves show a weak dependence on the density imbalance, with a weak maximum at an intermediate imbalance (=0.55 for equal masses, and similarly for the other mass ratios considered here).

3.3 Chemical potentials and momentum distribution functions at the QCP

Chemical potentials Figure 3.3 reports the chemical potentials at g_c as a function of the mass ratio $m_{\mathrm{B}}/m_{\mathrm{F}}$, for different density imbalances. As it can be seen from the main panel, the (negative) bosonic chemical potential increases very rapidly in absolute value for $m_{\mathrm{B}}/m_{\mathrm{F}} \to 0$. This is because at g_c the bosonic chemical potential is already close to its strong-coupling limit, $\mu_{\mathrm{B}} \approx -\epsilon_0$, such that the dimensionless ratio $|\mu_{\mathrm{B}}|/E_{\mathrm{F}} \approx 2g^2 m_{\mathrm{F}}/m_r$.

Since $g_c \sim m_F/m_B$ for $m_B \to 0$, we have $|\mu_{\rm B}|/E_{\rm F} \sim (m_{\rm F}/m_{\rm B})^3$ in this limit.

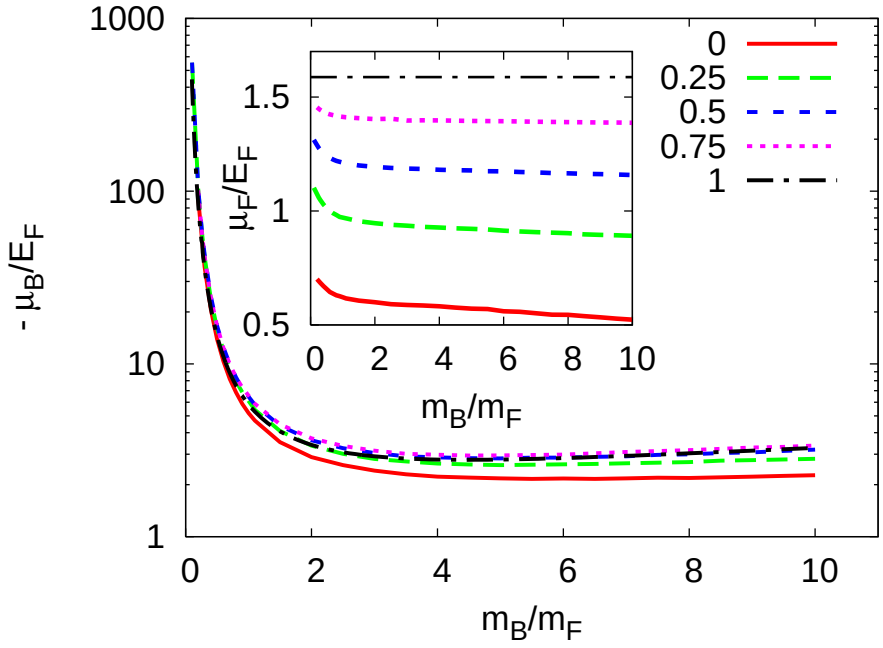

Figure 3.3: Bosonic chemical potential at the critical coupling g_c as a function of the mass ratio $m_{\rm B}/m_{\rm F}$ for different values of the density imbalance $(n_{\rm F} - n_{\rm B})/(n_{\rm F} + n_{\rm B})$. The corresponding fermionic chemical potential is reported in the inset.

In the opposite limit of large $m_{\rm B}/m_{\rm F}$, the ratio $m_{\rm F}/m_r$ slowly increases and eventually saturates to 1 for large $m_{\rm B}$, such that $|\mu_{\rm B}|/E_{\rm F}$ follows the slow logarithmic increase of g_c in this limit.

The fermionic chemical potential (reported in the inset) depends weakly on the mass imbalance, reflecting the weak dependence on g_c. As a matter of fact, the fermion chemical potential is determined essentially by the fermion density $n_{\rm F}$, independently from the coupling value or mass ratio.

Momentum distribution functions We pass now to study the momentum distribution functions $n_{\rm B}(|\mathbf{q}|)$ and $n_{\rm F}(|\mathbf{k}|)$ for the bosons and fermions, as obtained from Eqs. (3.3) and (3.4), respectively. We present results for a density imbalance $(n_{\rm F} - n_{\rm B})/(n_{\rm F} + n_{\rm B}) = 0.75$, as

to emphasize an interesting behavior of the bosonic momentum distribution function, which occurs only for a sufficiently large imbalance.

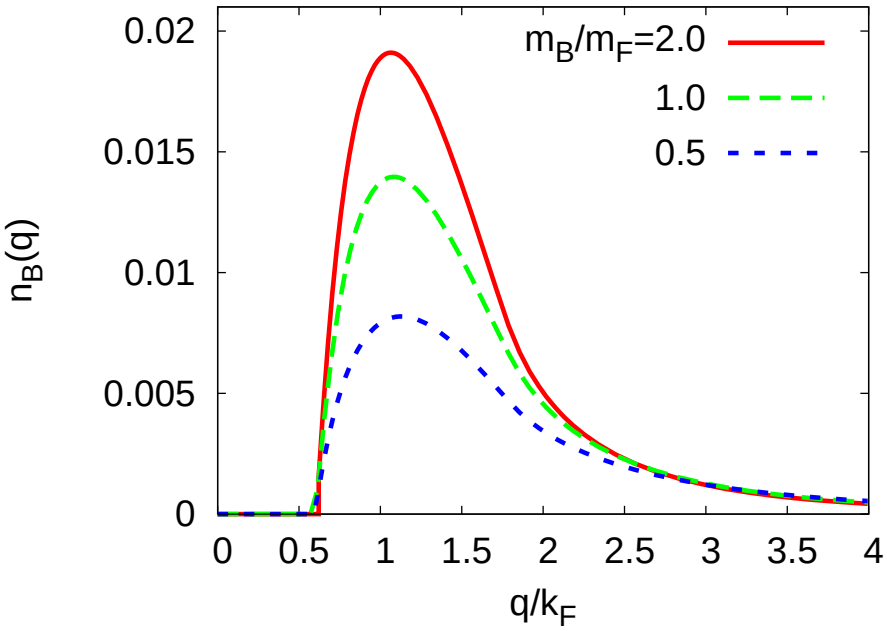

Figure 3.4: Bosonic momentum distribution curves at g_c for a fixed density imbalance $(n_F - n_B)/(n_F + n_B) = 0.75$ and different values of the mass ratio (m_B/m_F).

One can see, indeed, from Fig. 3.4 that the bosonic momentum distribution function vanishes identically at low momenta. This empty region extends from $|\mathbf{q}| = 0$ up to a certain value $|\mathbf{q}| = q_0$, which is determined essentially only by the density imbalance (for the specific case of Fig. 3.4, $q_0 \simeq 0.55$).

The presence of the empty region can be interpreted as follows. For $n_F \gg n_B$, most of fermions remain unpaired and fill a Fermi sphere of radius $k_{UF} \simeq [(n_F - n_B)/6\pi^2]^{1/3}$, as Fig. 3.5 for the fermionic distribution clearly shows. At g_c and larger couplings, the bosons are instead bound into molecules that, being composite fermions, fill a Fermi sphere with a radius $P_{CF} \simeq (n_B/6\pi^2)^{1/3}$. Now, as the region $|\mathbf{k}| < k_{UF}$ is already occupied by the unpaired fermions, only fermions with $|\mathbf{k}| > k_{UF}$ participate to the molecule. Since the momentum of

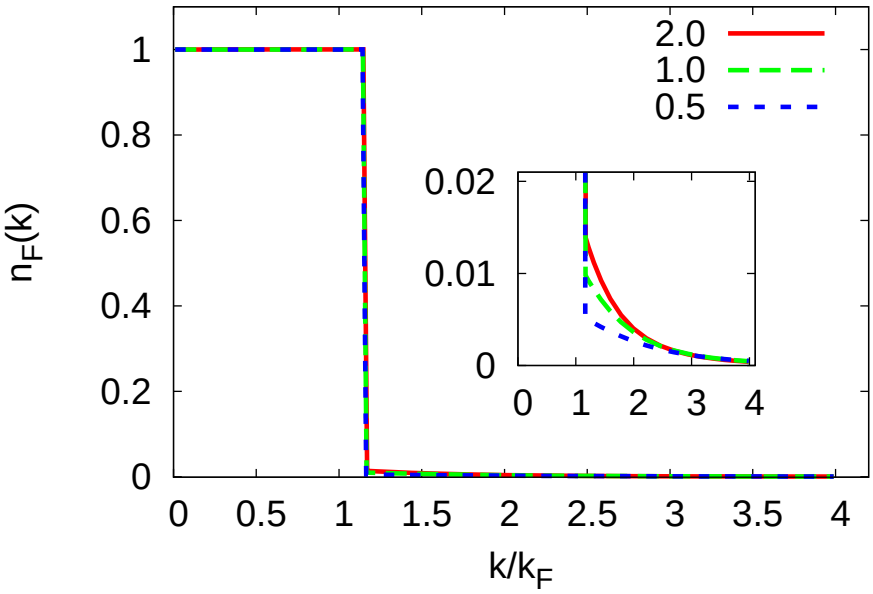

Figure 3.5: Fermionic momentum distribution curves at g_c for a fixed density imbalance $(n_{\rm F} - n_{\rm B})/(n_{\rm F} + n_{\rm B}) = 0.75$ and different values of the mass ratio $m_{\rm B}/m_{\rm F}$. The inset corresponds to a cut of the vertical scale.

the molecule is given by the sum $\mathbf{P} = \mathbf{q} + \mathbf{k}$, the constraints $|\mathbf{P}| < P_{\rm CF}$ and $|\mathbf{k}| > k_{\rm UF}$ then imply that only bosons with $|\mathbf{q}| > q_0 = k_{\rm UF} - P_{\rm CF}$ participate to the molecule, leaving thus empty the region $|\mathbf{q}| < q_0$.

We have verified that the equation $q_0 = k_{\rm UF} - P_{\rm CF}$ reproduces rather accurately the values of q_0 obtained numerically. In particular, the empty region does not exist at small density imbalance, when $k_{\rm UF} < P_{\rm CF}$ and it is expected to occur for a density imbalance greater than 1/3, which corresponds to a boson concentration $n_B/n_F = 0.5$. Note also that the initial rise of $n_{\rm B}(|\mathbf{q}|)$ after the threshold q_0 is due to the progressive increase of the phase-space volume corresponding to the $\mathbf{q}$'s satisfying the above constraints at a given $\mathbf{k}$. The saturation volume in phase-space is reached for $|\mathbf{q}|$ of the order of $k_{\rm UF}$, after which $n_{\rm B}(|\mathbf{q}|)$ starts to decrease, following eventually at sufficiently large wave-vectors a molecular-

like internal wave-function $n_{\rm B}(|\mathbf{q}|) \simeq n_{\rm M}|\phi(|\mathbf{q}|)|^2$, where $|\phi(|\mathbf{q}|)|^2$ can be approximated by the two-body normalized wave-function $\phi(|\mathbf{q}|) = (8\pi a^3)^{1/2}/(\mathbf{q}^2a^2+1)$, while the coefficient $n_{\rm M} \simeq n_{\rm B}$ can be interpreted as the molecular density.

The above approximate expression for $n_{\rm B}(|\mathbf{q})$ accounts for the main difference in the curves calculated at different mass ratios (namely, the decreasing height of the curves when the mass ratio is lowered) due to the strong dependence of g_c, and then of a, on the mass ratio. Note further that the same kind of beaviour is seen in the fermionic distribution function at momenta $|\mathbf{k}| > k_{\rm UF}$, as it can be evinced from the inset in Fig. 3.5. The comparison between the inset of Fig. 3.5 and Fig. 3.4 shows indeed that the bosonic and fermionic distribution functions become identical as the momentum increases; at large momenta $n_{\rm F}(|\mathbf{k}|) \sim n_{\rm B}(|\mathbf{k}|) \sim C/\mathbf{k}^4$, consistently with the universal large momenta behavior established in Ref. [Tan08]. In particular, within our approximation, one can prove by taking the large $|\mathbf{k}|$ limit in our expressions that the "contact" constant C is given by $C = -4m_r^2 \int \frac{d^4P}{(2\pi)^4}\Gamma(P)e^{i\Omega 0^+}$. In the strong-coupling limit, where all bosons are bound into molecules, a comparison with the expression for the molecular internal wave-function then leads to the equation $C = 8\pi n_{\rm B}/a$.

Figure 3.6 reports the contact constant C at g_c normalized to its strong-coupling limit value $8\pi n_{\rm B}/a$, as a function of the mass ratio $m_{\rm B}/m_{\rm F}$ for different values of the density imbalance. One can see that the constant C at g_c is close to its strong-coupling limit expression for all cases considered, with the largest deviations occuring at intermediate values of the mass ratio, as expected, since this is the region where g_c reaches its minimum and consequently the strong-coupling condition is less respected

3.4 The one boson limit

In this section we consider the "one boson" limit $(n_{\rm F} - n_{\rm B})/(n_{\rm F} + n_{\rm B}) \to 1$ of our equations. In this limit the fermions become free due to the vanishing boson density. One has then $\Sigma_{\rm F} = 0$ and $\mu_{\rm F} = (6\pi^2 n_{\rm F})^{2/3}/(2m_{\rm F}) = 2^{2/3}E_{\rm F}$. The boson self-energy $\Sigma_{\rm B}$ remains instead

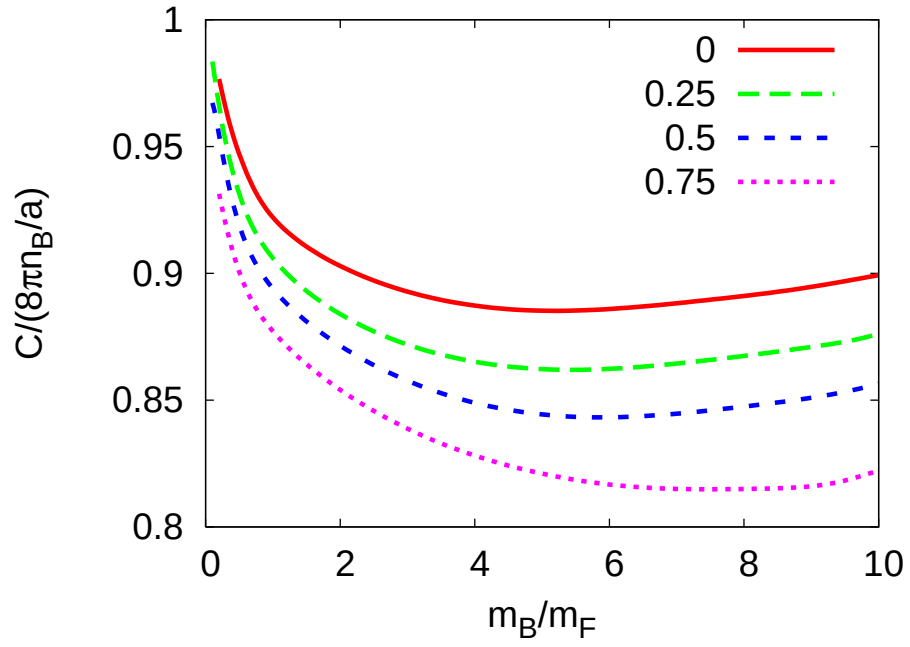

Figure 3.6: Contact constant C, normalized to its strong-coupling limit $8\pi n_{\mathrm{B}}/a$, at g_c vs. the mass ratio $m_{\mathrm{B}}/m_{\mathrm{F}}$ for different values of the density imbalance $(n_{\mathrm{F}} - n_{\mathrm{B}})/(n_{\mathrm{F}} + n_{\mathrm{B}})$.

finite and is determined by Eq. (3.1), with no simplifications with respect to the case at finite boson density. The full knowledge of Σ_{B} is however not necessary to calculate μ_{B} in the limit $n_{\mathrm{B}} \to 0$. A study of the analytic structure of Σ_{B} in the complex frequency space along the lines of Ref. [Com09] shows that the limit $n_{\mathrm{B}} \to 0$ corresponds, for $g > g_c$, to the requirement that the minimum of the composite fermion dispersion $\Omega_0(\mathbf{P})$ occurs exactly at zero frequency. By introducing the retarded composite-fermion propagator via the replacement $\Gamma^{\mathrm{R}}(\mathbf{P}, \omega) \equiv \Gamma(\mathbf{P}, i\Omega \to \omega + i0^+)$, the dispersion $\Omega_0(\mathbf{P})$ is determined by the pole of $\Gamma^{\mathrm{R}}(\mathbf{P}, \omega)$ in the complex plane. By assuming the minimum of $\Omega_0(|\mathbf{P}|)$ to occur at $\mathbf{P} = 0$, one has then the equation $\Gamma^{\mathrm{R}}(0,0)^{-1} = 0$, which determines μ_{B} at a given coupling and mass ratio. The critical coupling g_c, on the other hand, is determined by the equation $\mu_{\mathrm{B}} = \Sigma_{\mathrm{B}}(0,0)$, as for finite density. In the limit $n_{\mathrm{B}} \to 0$ only the pole of the fermionic

Green's function contributes to the frequency integral in Eq. (3.1), yielding:

$$\Sigma_{\rm B}(0,0) = -\int \frac{d\mathbf{P}}{(2\pi)^3}\Theta[-\xi_{\rm F}(\mathbf{P})]\Gamma^{\rm R}(\mathbf{P},\xi_{\rm F}(\mathbf{P})), \tag{3.12}$$

where

$$\Gamma^{\rm R}(\mathbf{P},\xi_{\rm F}(\mathbf{P})) = \left[-\frac{m_r}{2\pi a} + \frac{m_r^{3/2}}{\sqrt{2}\pi}\sqrt{|\mu_{\rm B}| - \frac{m_{\rm B}\mathbf{P}^2}{2m_{\rm F}M}} + I_{\rm F}(\mathbf{P})\right]^{-1} \tag{3.13}$$

and

$$I_{\rm F}(\mathbf{P}) \equiv \int \frac{d\mathbf{p}}{(2\pi)^3}\frac{\Theta[-\xi_{\rm F}(\frac{m_{\rm F}}{M}\mathbf{P}-\mathbf{p})]}{\frac{\mathbf{p}^2}{2m_r} - \frac{m_{\rm B}}{m_{\rm F}}\frac{\mathbf{P}^2}{2M} + |\mu_{\rm B}|}. \tag{3.14}$$

A calculation of the above integral yields

$$\begin{aligned} I_{\rm F}(\mathbf{P}) &= \frac{m_r k_{\mu_{\rm F}}}{2\pi^2} + \frac{m_{\rm B}L_{\mathbf{P}}}{4\pi^2}\frac{k_{\mu_{\rm F}}^2 + 2m_r|\mu_{\rm B}| - 2(\frac{\bar{m}}{M}|\mathbf{P}|)^2}{2|\mathbf{P}|} \\ &- \frac{m_r R_{\mathbf{P}}}{2\pi^2}\left[\arctan\left(\frac{k_{\mu_{\rm F}} + \frac{m_{\rm F}}{M}|\mathbf{P}|}{R_{\mathbf{P}}}\right) + \arctan\left(\frac{k_{\mu_{\rm F}} - \frac{m_{\rm F}}{M}|\mathbf{P}|}{R_{\mathbf{P}}}\right)\right], \end{aligned} \tag{3.15}$$

where $R_{\mathbf{P}} \equiv [2m_r|\mu_{\rm B}| - (|\mathbf{P}|m_{\rm B}/M)^2]^{1/2}$, while

$$L_{\mathbf{P}} \equiv \ln\left[\frac{(k_{\mu_{\rm F}} + |\mathbf{P}|)(k_{\mu_{\rm F}} + \frac{\delta m}{M}|\mathbf{P}|) + 2m_r|\mu_{\rm B}|}{(k_{\mu_{\rm F}} - |\mathbf{P}|)(k_{\mu_{\rm F}} - \frac{\delta m}{M}|\mathbf{P}|) + 2m_r|\mu_{\rm B}|}\right], \tag{3.16}$$

where $\delta m = m_{\rm F} - m_{\rm B}$ and $\bar{m}^2 = (m_{\rm F}^2 + m_{\rm B}^2)/2$. By using the expressions (3.13) to (3.16), the self-energy $\Sigma_{\rm B}(0,0)$ can then be calculated easily by a simple one-dimensional integral over $|\mathbf{P}|$. At g_c the equation $\mu_{\rm B} = \Sigma_{\rm B}(0,0)$ then yields:

$$\mu_{\rm B} = -\int_0^{k_{\mu_{\rm F}}} \frac{d|\mathbf{P}|}{2\pi^2}\Gamma^{\rm R}(|\mathbf{P}|,\xi_{\rm F}(|\mathbf{P}|)). \tag{3.17}$$

The equation $0 = \Gamma^{\rm R}(0,0)^{-1}$ yields finally

$$0 = -\frac{m_r}{2\pi a} + \frac{m_r^{3/2}}{\pi}\sqrt{|\mu|} + \frac{m_r}{\pi^2}\left[k_{\mu_{\rm F}} - 2\sqrt{m_r|\mu|}\arctan\left(\frac{k_{\mu_{\rm F}}}{2\sqrt{m_r|\mu|}}\right)\right]. \tag{3.18}$$

The simultaneous solution of Eqs. (3.17) and (3.18) allows to obtain g_c and $\mu_{\rm B}$ for a given mass ratio. Note finally that, even though we have derived Eqs. (3.17) and (3.18) as a

limiting case of our equations for a Bose-Fermi mixture, they describe also the polaron-to-molecule transition in a Fermi-Fermi mixture, since in this limit the statistics of the minority species becomes immaterial. We have verified, indeed, that our results for g_c in this limit agree with the results reported in Ref. [Com09] for the "first-level approximation".

Asymptotic expressions for g_c at small and large mass ratios We conclude this section by presenting the derivation of the asymptotic expressions (3.8) and (3.10). We assume μ_{B} to be large and negative as it occurs when g is large. The validity of this assumption is verified by the asymptotic expressions for g_c that are obtained accordingly. The chemical potential $\mu = (\mu_{\mathrm{B}} + \mu_{\mathrm{F}})/2$ is then also large and negative. By expanding Eq. (3.18) in powers of $k_{\mu_{\mathrm{F}}}/\sqrt{m_r|\mu|}$ one obtains

$$2\mu \approx -\epsilon_0 + \frac{2}{3\pi m_r} k_{\mu_{\mathrm{F}}}^3 a, \tag{3.19}$$

or, equivalently

$$\mu_{\mathrm{B}} \approx -\epsilon_0 - \mu_{\mathrm{F}} + \frac{2}{3\pi m_r} k_{\mu_{\mathrm{F}}}^3 a. \tag{3.20}$$

Note that the subleading term $\frac{2}{3\pi m_r} k_{\mu_{\mathrm{F}}}^3 a$ in Eq. (3.19) describes the mean-field repulsion between the molecule forming in the strong-coupling limit and the fermions, as it can be seen by casting it in the form $n_{\mathrm{F}} \frac{2\pi}{m_{\mathrm{MF}}} a_{\mathrm{MF}}$, where $m_{\mathrm{MF}} = M m_{\mathrm{F}}/(m_{\mathrm{F}} + M)$ is the reduced mass of a molecule and one fermion, while

$$a_{\mathrm{MF}} = \frac{(1 + m_{\mathrm{F}}/m_{\mathrm{B}})^2}{1/2 + m_{\mathrm{F}}/m_{\mathrm{B}}} a \tag{3.21}$$

is the molecule-fermion scattering length within the Born approximation [Isk07].

The large and negative value of μ_{B} then implies $I_{\mathrm{F}}(\mathbf{P}) \approx n_{\mathrm{F}}/|\mu_{\mathrm{B}}| \approx n_{\mathrm{F}}/\epsilon_0$, as it can be seen more easily directly from Eq. (3.14). The expansion of (3.13) for $|\mu_{\mathrm{B}}|$ large then yields

$$\Gamma^{\mathrm{R}}(\mathbf{P}, \xi_{\mathrm{F}}(\mathbf{P})) \approx \frac{2\pi}{m_r^2 a} \frac{1}{\mu_{\mathrm{F}} - \alpha \mathbf{P}^2} \tag{3.22}$$

where we have used Eq. (3.19), and $\alpha \equiv m_{\rm B}/(2Mm_{\rm F})$. By using Eq. (3.12) we obtain

$$\begin{aligned}\Sigma_{\rm B}(0,0) &\approx \frac{1}{\alpha\pi m_r^2 a}\left[k_{\mu_{\rm F}} + \frac{\sqrt{\mu_{\rm F}/\alpha}}{2}\ln\frac{\sqrt{\mu_{\rm F}/\alpha}-k_{\mu_{\rm F}}}{k_{\mu_{\rm F}}+\sqrt{\mu_{\rm F}/\alpha}}\right] \\ &= \frac{k_{\mu_{\rm F}}}{\alpha\pi m_r^2 a}\left[1+\frac{\sqrt{1+\frac{m_{\rm F}}{m_{\rm B}}}}{2}\ln\frac{\sqrt{1+\frac{m_{\rm F}}{m_{\rm B}}}-1}{\sqrt{1+\frac{m_{\rm F}}{m_{\rm B}}}+1}\right]. \end{aligned} \tag{3.23}$$

By expanding the expression (3.23) for a *small* mass ratio $m_{\rm B}/m_{\rm F} \ll 1$, we obtain

$$\begin{aligned}\Sigma_{\rm B}(0,0) &\approx \frac{k_{\mu_{\rm F}}}{\alpha\pi m_r^2 a}\left[-\frac{1}{3}\frac{m_{\rm B}}{m_{\rm F}}+\frac{2}{15}\left(\frac{m_{\rm B}}{m_{\rm F}}\right)^2\right] \\ &\approx -\frac{2^{4/3}}{3\pi}\frac{k_{\rm F}}{am_{\rm B}}\frac{m_{\rm F}}{m_{\rm B}}\left(1+\frac{8}{5}\frac{m_{\rm B}}{m_{\rm F}}\right). \end{aligned} \tag{3.24}$$

The equation $\mu_{\rm B} = \Sigma_{\rm B}(0,0)$ then yields

$$\epsilon_0 = \frac{2^{4/3}}{3\pi}\frac{k_{\rm F}}{am_r}\frac{m_{\rm F}}{m_{\rm B}}\left(1+\frac{8}{5}\frac{m_{\rm B}}{m_{\rm F}}\right), \tag{3.25}$$

where we have kept only the leading term in the expression (3.20) for $\mu_{\rm B}$ (the term $\mu_{\rm F}$ would give a correction of order $(m_{\rm B}/m_{\rm F})^2$ to the asymptotic expression for g_c, with the last term in (3.20) contributing an even smaller correction).
By substituting $\epsilon_0 = 1/(2m_r a^2)$ we obtain then

$$\frac{1}{k_F a} = \frac{4\cdot 2^{1/3}}{3\pi}\frac{m_{\rm F}}{m_{\rm B}}\left(1+\frac{8}{5}\frac{m_{\rm B}}{m_{\rm F}}\right), \tag{3.26}$$

which coincides with the expression (3.8) and gives a large value of g_c for small mass ratios, consistently with our starting assumption. The asymptotic expression (3.26) is compared with the full numerical calculation of g_c in Fig. 3.7 (a).

The expansion of Eq. (3.23) for a *large* mass ratio $m_{\rm B}/m_{\rm F} \gg 1$ yields instead

$$\Sigma_{\rm B}(0,0) \approx \frac{k_{\mu_{\rm F}}}{\alpha\pi m_r^2 a}\left(1+\frac{1}{2}\ln\frac{m_{\rm F}}{4m_{\rm B}}\right) \tag{3.27}$$

$$\approx \frac{2^{4/3}}{\pi}\frac{k_{\rm F}}{am_{\rm F}}\left(1+\frac{1}{2}\ln\frac{m_{\rm F}}{4m_{\rm B}}\right) \tag{3.28}$$

where we have disregarded corrections to (3.28) smaller at least by a factor $m_{\rm F}/m_{\rm B}$. By equating (3.28) to (3.20) we get then

$$\epsilon_0 + \mu_{\rm F} - \frac{2k_{\mu_{\rm F}}^3 a}{3\pi m_r} = \frac{2^{\frac{4}{3}}}{\pi}\frac{k_{\rm F}}{a m_{\rm F}}\left(-1 + \frac{1}{2}\ln\frac{4m_{\rm B}}{m_{\rm F}}\right) \tag{3.29}$$

yielding

$$\frac{1}{2a^2 m_{\rm F}} = \frac{2^{\frac{1}{3}}k_{\rm F}}{\pi a m_{\rm F}}\left(\ln\frac{4m_{\rm B}}{m_{\rm F}} - 2\right) - \frac{2^{\frac{2}{3}}k_F^2}{2m_{\rm F}} + \frac{4k_{\rm F}^3 a}{3\pi m_{\rm F}} \tag{3.30}$$

from which, by multiplying both sides of Eq. (3.30) by $2am_{\rm F}/k_{\rm F}$, we obtain

$$\frac{1}{k_{\rm F}a} = \frac{2^{\frac{4}{3}}}{\pi}\left(\ln\frac{4m_{\rm B}}{m_{\rm F}} - 2\right) - 2^{\frac{2}{3}}k_{\rm F}a + \frac{8(k_{\rm F}a)^2}{3\pi} \tag{3.31}$$

which shows that, to leading order, $g_c \approx \frac{2^{\frac{4}{3}}}{\pi}\ln\frac{m_{\rm B}}{m_{\rm F}}$ at large mass ratios. The slow log-dependence of g_c on $m_{\rm B}/m_{\rm F}$ makes however significant to keep also a few subleading corrections to the leading behavior. The solution of Eq. (3.31) by iteration yields then

$$\frac{1}{k_{\rm F}a} = \frac{2^{\frac{4}{3}}}{\pi}\left(\ln\frac{4m_{\rm B}}{m_{\rm F}} - 2\right) - \frac{2^{\frac{2}{3}}}{\frac{2^{\frac{4}{3}}}{\pi}\left(\ln\frac{4m_{\rm B}}{m_{\rm F}} - 2\right)} + \frac{8}{3\pi}\frac{1}{\left[\frac{2^{\frac{4}{3}}}{\pi}\left(\ln\frac{4m_{\rm B}}{m_{\rm F}} - 2\right)\right]^2} \tag{3.32}$$

which ignores corrections of order $1/(\ln\frac{m_{\rm B}}{m_{\rm F}})^3$ or higher, and coincides with the expression (3.10) reported in Sec. IV. The asymptotic expression (3.32) is compared with the full numerical calculation of g_c in Fig. 3.7 (b).

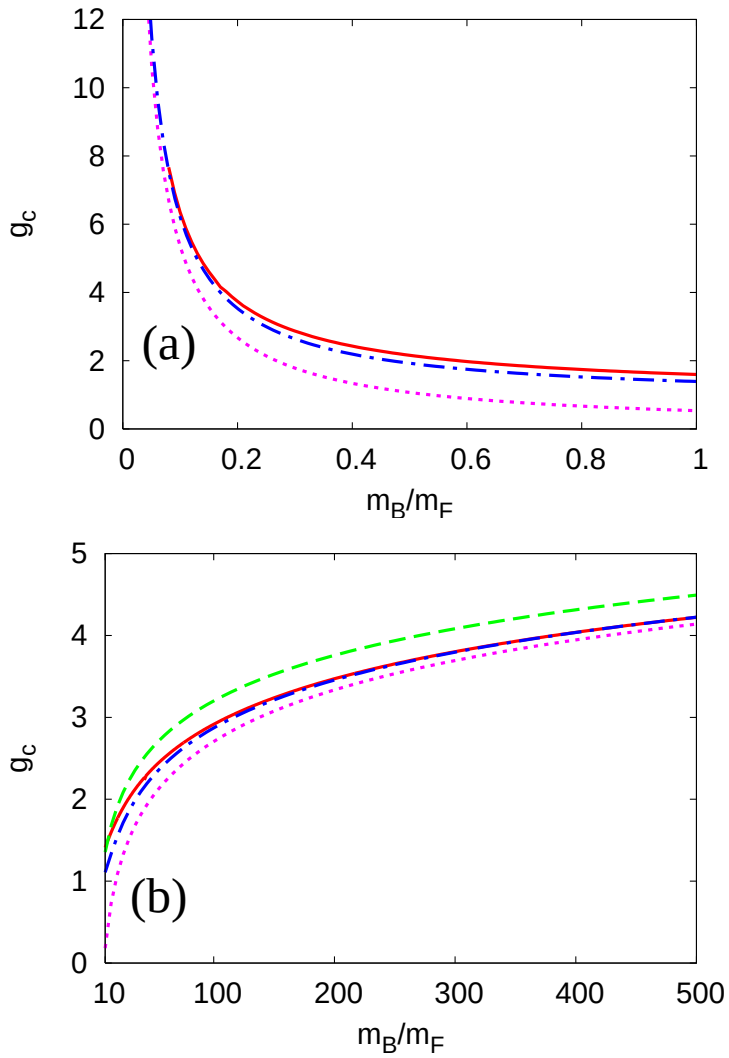

Figure 3.7: (a) The asymptotic expression (3.26) for g_c at small mass ratios (dashed-dotted line) is compared with the full numerical solution (full line). The dotted curve is obtained by neglecting the subleading term within the brackets in (3.26). (b) The asymptotic expression (3.32) for g_c at large mass ratios (dashed-dotted line) is compared with the full numerical solution (full line). The dashed curve is obtained by neglecting the second and third terms on the right-hand side of (3.32), while the dotted curve neglects only the third term.

Chapter 4

Spectral Weights and Dispersions at zero-temperature

The single-particle excitation spectrum can be predicted by many-body theory (see [Fet71]) and is a fundamental property of any interacting system. As the interaction between particles is increased, the single-particle eigenstates of the non-interacting case become quasi-particles and the excitation spectrum may qualitatively change, providing, for example, the appearence of energy gaps. For this reason the study of the single-particle spectral weight functions and dispersions is essential to understand the behavior of strongly-interacting systems. The use of the experimental technique of photoemission spectroscopy allows to probe the elementary excitations and energy dispersions in ultracold matter. Recently, radio-frequency spectroscopy has been used very successfully to investigate strongly interacting Fermi gases [Ste08, Gae10]. We believe that this powerful technique may be applied to explore also resonant Bose-Fermi mixtures in the near future. In experiments, a radio-frequency photon changes the internal state of an atom from a state which strongly interacts with the surroundings atoms to a state which is weakly- (or not) interacting. By measuring the energy and momentum of the outcoupled atoms it is possible to extract information on the quasi-particle excitations and their dispersion relation. On the other hand the technique of the inverse radio-frequency spectroscopy allows to measure the excitation spectrum of a

particle added to the system, whose behavior is described by the positive frequency range of the single-particle spectral weight function.

4.1 Formalism

Spectral Weight Functions The bosonic and the fermionic spectral weight functions are expressed in terms of the corresponding imaginary parts of the retarded Green's functions as:

$$A_B(\mathbf{q},\omega) = -\frac{1}{\pi}\Im G_B^R(\mathbf{q},\omega) \tag{4.1}$$

$$A_F(\mathbf{k},\omega) = -\frac{1}{\pi}\Im G_F^R(\mathbf{k},\omega). \tag{4.2}$$

The bosonic and fermionic retarded Green's functions are obtained by the analytic continuation to the real axis of the Matsubara Green's functions.

$$G_B^R(\mathbf{q},\omega) = \left[\omega - \frac{q^2}{2m_B} + \mu_B - \Sigma_B^R(\mathbf{q},\omega) + i\eta\right]^{-1} \tag{4.3}$$

$$G_F^R(\mathbf{k},\omega) = \left[\omega - \frac{k^2}{2m_F} + \mu_F - \Sigma_F^R(\mathbf{k},\omega) + i\eta\right]^{-1}, \tag{4.4}$$

where η is a positive infinitesimal quantity.
The same analytic continuation is performed to obtain the retarded T-matrix in order to introduce its spectral representation

$$\Gamma^R(\mathbf{P},\omega') = \Gamma(\mathbf{P}, i\Omega_m \to \omega' + i\eta) \tag{4.5}$$

$$\Gamma(\mathbf{P}, i\Omega_m) = -\int_{-\infty}^{\infty} \frac{d\omega'}{\pi} \frac{\Im\Gamma^R(\mathbf{P},\omega')}{i\Omega_m - \omega'}. \tag{4.6}$$

The Matsubara self-energies are defined as

$$\Sigma_B(\mathbf{q}, i\omega_\nu) = -\frac{1}{\beta}\int \frac{d\mathbf{P}}{(2\pi)^3} \sum_m G_F^0(\mathbf{P}-\mathbf{q}, i\Omega_m - i\omega_\nu)\Gamma(\mathbf{P}, i\Omega_m) \tag{4.7}$$

$$\Sigma_F(\mathbf{k}, i\omega_n) = \frac{1}{\beta}\int \frac{d\mathbf{P}}{(2\pi)^3} \sum_m G_B^0(\mathbf{P}-\mathbf{k}, i\Omega m - i\omega_n)\Gamma(\mathbf{P}, i\Omega_m), \tag{4.8}$$

where $\mathbf{q}$, $\mathbf{k}$, $\mathbf{P}$ and ω_ν, ω_n, Ω_m are respectively the momenta and the Matsubara frequencies of bosons, fermions and composite fermions.

By inserting the spectral representation (4.6) in the previous expressions we obtain

$$\Sigma_B(\mathbf{q}, i\omega_\nu) = \int \frac{d\mathbf{P}}{(2\pi)^3} \int_{-\infty}^{\infty} \frac{d\omega'}{\pi} \Im\Gamma^R(\mathbf{P}, \omega') \frac{f(\xi^F_{\mathbf{P}-\mathbf{q}}) - f(\omega')}{i\omega_\nu + \xi^F_{\mathbf{P}-\mathbf{q}} - \omega'} \tag{4.9}$$

$$\Sigma_F(\mathbf{k}, i\omega_n) = \int \frac{d\mathbf{P}}{(2\pi)^3} \int_{-\infty}^{\infty} \frac{d\omega'}{\pi} \Im\Gamma^R(\mathbf{P}, \omega') \frac{b(\xi^B_{\mathbf{P}-\mathbf{k}}) + f(\omega')}{i\omega_n + \xi^B_{\mathbf{P}-\mathbf{k}} - \omega'} \tag{4.10}$$

and continuing analitically on the real axis, we get the retarded self-energies:

$$\Sigma^R_B(\mathbf{q}, \omega) = \int \frac{d\mathbf{P}}{(2\pi)^3} \int_{-\infty}^{\infty} \frac{d\omega'}{\pi} \Im\Gamma^R(\mathbf{P}, \omega') \frac{f(\xi^F_{\mathbf{P}-\mathbf{q}}) - f(\omega')}{\omega - \omega' + \xi^F_{\mathbf{P}-\mathbf{q}} + i\eta} \tag{4.11}$$

$$\Sigma^R_F(\mathbf{k}, \omega) = \int \frac{d\mathbf{P}}{(2\pi)^3} \int_{-\infty}^{\infty} \frac{d\omega'}{\pi} \Im\Gamma^R(\mathbf{P}, \omega') \frac{b(\xi^B_{\mathbf{P}-\mathbf{k}}) + f(\omega')}{\omega - \omega' + \xi^B_{\mathbf{P}-\mathbf{k}} + i\eta}, \tag{4.12}$$

where $f(x)$ and $b(x)$ are respectively the Fermi and Bose functions, and we have defined $\xi^{B,F}_{\mathbf{k}} = \frac{\mathbf{k}^2}{2m_{B,F}} - \mu_{B,F}$.

Considering the zero-temperature limit of the retarded self-energies we have:

$$\Sigma^R_B(\mathbf{q}, \omega) = \int \frac{d\mathbf{P}}{(2\pi)^3} \int_{-\infty}^{\infty} \frac{d\omega'}{\pi} \Im\Gamma^R(\mathbf{P}, \omega') \frac{\Theta(\mu_F - \frac{(\mathbf{P}-\mathbf{q})^2}{2m_F}) - \Theta(-\omega')}{\omega - \omega' + \xi^F_{\mathbf{P}-\mathbf{q}} + i\eta}$$

$$\Sigma^R_B(\mathbf{q}, \omega) \equiv \Sigma^R_B(\mathbf{q}, \omega)^I + \Sigma^R_B(\mathbf{q}, \omega)^{II} \tag{4.13}$$

$$\Sigma^R_F(\mathbf{k}, \omega) = \int \frac{d\mathbf{P}}{(2\pi)^3} \int_{-\infty}^{\infty} \frac{d\omega'}{\pi} \Im\Gamma^R(\mathbf{P}, \omega') \frac{\Theta(-\omega')}{\omega - \omega' + \xi^B_{\mathbf{P}-\mathbf{k}} + i\eta} =$$

$$= \int \frac{d\mathbf{P}}{(2\pi)^3} \int_{-\infty}^{0} \frac{d\omega'}{\pi} \frac{\Im\Gamma^R(\mathbf{P}, \omega')}{\omega - \omega' + \xi^F_{\mathbf{P}-\mathbf{q}} + i\eta} \tag{4.14}$$

where we have splitted the bosonic self-energy in two expressions:

$$\Sigma^R_B(\mathbf{q}, \omega)^I = \int \frac{d\mathbf{P}}{(2\pi)^3}\ \Theta\left(\mu_F - \frac{(\mathbf{P}-\mathbf{q})^2}{2m_F}\right) \int_{-\infty}^{\infty} \frac{d\omega'}{\pi} \frac{\Im\Gamma^R(\mathbf{P}, \omega')}{\omega - \omega' + \xi^F_{\mathbf{P}-\mathbf{q}} + i\eta} \tag{4.15}$$

$$\Sigma^R_B(\mathbf{q}, \omega)^{II} = -\int \frac{d\mathbf{P}}{(2\pi)^3} \int_{-\infty}^{0} \frac{d\omega'}{\pi} \frac{\Im\Gamma^R(\mathbf{P}, \omega')}{\omega - \omega' + \xi^F_{\mathbf{P}-\mathbf{q}} + i\eta}. \tag{4.16}$$

Henceforth we will continue the calculation considering dimensionless expressions. We measure the momentum in unity of $k_F = (3\pi^2 n)^{1/3}$, the mass in unity of m_F and the energy in unity of E_F.

The fermionic self-energy has a simpler expression than the bosonic one and it is similar to the the second term of the bosonic self-energy (4.16). By calculating in spherical coordinates the integral in (4.13) we obtain

$$\Sigma_F^R(\mathbf{k},\omega) = -\frac{m_B}{8\pi^3 k}\int_0^{+\infty} dPP \int_{-\infty}^{0} d\omega' \Im\Gamma^R(\mathbf{P},\omega') \ln\left[\frac{\omega-\omega'+\frac{(\mathbf{P}-\mathbf{k})^2}{m_B}-\mu_B+i\eta}{\omega-\omega'+\frac{(\mathbf{P}+\mathbf{k})^2}{m_B}-\mu_B+i\eta}\right], \tag{4.17}$$

and similarly

$$\Sigma_B^R(\mathbf{q},\omega)^{II} = \frac{1}{8\pi^3 q}\int_0^{+\infty} dPP \int_{-\infty}^{0} d\omega' \Im\Gamma^R(\mathbf{P},\omega') \ln\left[\frac{\omega-\omega'+(\mathbf{P}-\mathbf{q})^2-\mu_F+i\eta}{\omega-\omega'+(\mathbf{P}+\mathbf{q})^2-\mu_F+i\eta}\right]. \tag{4.18}$$

By taking the limit $\eta \to 0^+$ and defining

$$\rho_F = \frac{\omega-\omega'+\frac{(\mathbf{P}-\mathbf{k})^2}{m_B}-\mu_B}{\omega-\omega'+\frac{(\mathbf{P}+\mathbf{k})^2}{m_B}-\mu_B} \tag{4.19}$$

$$\rho_B^{II} = \frac{\omega-\omega'+(\mathbf{P}-\mathbf{q})^2-\mu_F}{\omega-\omega'+(\mathbf{P}+\mathbf{q})^2-\mu_F}, \tag{4.20}$$

we get

$$\Sigma_F^R(\mathbf{k},\omega) = -\frac{m_B}{8\pi^3 k}\int_0^{+\infty} dPP \int_{-\infty}^{0} d\omega' \Im\Gamma^R(\mathbf{P},\omega') \left(\ln|\rho_F| + i\pi\Theta(-\rho_F)\right) \tag{4.21}$$

$$\Sigma_B^R(\mathbf{q},\omega)^{II} = \frac{1}{8\pi^3 q}\int_0^{+\infty} dPP \int_{-\infty}^{0} d\omega' \Im\Gamma^R(\mathbf{P},\omega') \left(\ln|\rho_B^{II}| + i\pi\Theta(-\rho_B^{II})\right), \tag{4.22}$$

while the expression for $\Sigma_B^R(\mathbf{q},\omega)^I$ will be derived below. We know that $\Im\Gamma^R(\mathbf{P},\omega')^{-1} \neq 0$ for $\omega' > \omega_0 > 0$, where ω_0 is a threshold frequency which can be obtained exactly. So the integrals on the frequency variable can be calculated analytically considering the delta-like contributions given by the poles $\omega_{p\Gamma}$ of the retarded T-matrix. Defining $\omega_{p\Gamma}$ the frequencies

given by the solutions of the equation: $\Re\Gamma^R(\mathbf{P},\omega')^{-1}=0$ (for $\omega'<0$) we obtain these final expressions from (4.21) and (4.22):

$$\begin{aligned}\Sigma_F^R(\mathbf{k},\omega) &= -\frac{m_B}{8\pi^2 k}\int_0^{k_\Gamma} dPP\left[\ln|\rho_F|+i\pi\Theta(-\rho_F)\right]_{\omega'=\omega_{p\Gamma}} \\ &\times \left|\frac{\partial\Re\left[\Gamma^R(\mathbf{P},\omega')^{-1}\right]}{\partial\omega'}\right|^{-1}_{\omega'=\omega_{p\Gamma}}. \end{aligned} \tag{4.23}$$

$$\begin{aligned}\Sigma_B^R(\mathbf{q},\omega)^{II} &= \frac{1}{8\pi^2 q}\int_0^{k_\Gamma} dPP\left[\ln|\rho_B^{II}|+i\pi\Theta(-\rho_B^{II})\right]_{\omega'=\omega_{p\Gamma}} \\ &\times \left|\frac{\partial\Re\left[\Gamma^R(\mathbf{P},\omega')^{-1}\right]}{\partial\omega'}\right|^{-1}_{\omega'=\omega_{p\Gamma}}. \end{aligned} \tag{4.24}$$

Finally we observe that the integrals on the momentum P of the "composite fermion" propagator are limited by the momentum k_Γ, which represents the last value accessible considering frequencies $\omega'\leq 0$. Actually k_Γ is the momentum at which the dispersion curve of the composite fermion $\omega_{CF}(k)$ reaches the zero and it corresponds to the jump in the momentum distribution function of the composite fermions (i.e. the Fermi momentum of the Fermi sphere of the composite fermions).

The first term of the bosonic self-energy (4.15) has a more complicated expression and cannot be reduced, as in the previous case, in such a compact form.

The step function $\Theta\left(\mu_F-\frac{(\mathbf{P}-\mathbf{q})^2}{2m_F}\right)$ restricts the domain of integration on the momentum $\mathbf{P}$ and gives two different expressions, according to the sign of $(k_{\mu_F}-q)$, where $k_{\mu_F}\equiv\sqrt{\mu_F}$, in unity of E_F. Then the order relation between the momenta k_Γ, $|k_{\mu_F}-q|$, $k_{\mu_F}+q$ has to be considered when calculating the frequency integral. Before writing the final expression for $\Sigma_B^R(\mathbf{q},\omega)^I$ we define the quantity

$$\rho_B^I=\frac{\omega-\omega'+(\mathbf{P}-\mathbf{q})^2-\mu_F}{\omega-\omega'}. \tag{4.25}$$

If $k_{\mu_F} < q$ we have

$$\begin{aligned}\Sigma_B^R(\mathbf{q},\omega)^I &= \frac{1}{(2\pi)^3 q}\int_{|k_{\mu_F}-q|}^{k_{\mu_F}+q} dPP \\ \times &\quad \left\{ \pi\left[\ln|\rho_B^I|^{-1} - i\pi\Theta(-\rho_B^I)\right]_{\omega'=\omega_{p\Gamma}} \times \left|\frac{\partial\Re\left[\Gamma^R(\mathbf{P},\omega')^{-1}\right]}{\partial\omega'}\right|^{-1}_{\omega'=\omega_{p\Gamma}} + \right. \\ + &\quad \left. \int_{\omega_0}^{+\infty} d\omega' \Im\Gamma^R(\mathbf{P},\omega')\left[\ln|\rho_B^I|^{-1} - i\pi\Theta(-\rho_B^I)\right] \right\}, \end{aligned} \tag{4.26}$$

where $\omega_{p\Gamma}$ is always defined as the the solution of the equation $\Re\left[\Gamma^R(\mathbf{P},\omega')^{-1}\right] = 0$ and has to belong to the interval $[0,\omega_0]$ when $k_\Gamma < |k_{\mu_F} - q| < k_{\mu_F} + q$. When $|k_{\mu_F} - q| < k_\Gamma < k_{\mu_F} + q$ and when $|k_{\mu_F} - q| < k_{\mu_F} + q < k_\Gamma$, we have respectively $\omega_{p\Gamma} \in (-\infty, \omega_0]$ and $\omega_{p\Gamma} \in (-\infty, 0]$.

If $k_{\mu_F} > q$ we have the general expression

$$\begin{aligned}\Sigma_B^R(\mathbf{q},\omega)^I &= \frac{1}{(2\pi)^3 q}\int_{0}^{|k_{\mu_F}-q|} dPP \\ \times &\quad \left\{ \pi\left[\ln|\rho_B^{II}| + i\pi\Theta(-\rho_B^{II})\right]_{\omega'=\omega'_{p\Gamma}} \times \left|\frac{\partial\Re\left[\Gamma^R(\mathbf{P},\omega')^{-1}\right]}{\partial\omega'}\right|^{-1}_{\omega'=\omega'_{p\Gamma}} + \right. \\ + &\quad \left. \int_{\omega_0}^{+\infty} d\omega' \Im\Gamma^R(\mathbf{P},\omega')\left[\ln|\rho_B^{II}| - i\pi\Theta(-\rho_B^{II})\right] \right\} \\ + &\quad \frac{1}{(2\pi)^3 q}\int_{|k_{\mu_F}-q|}^{k_{\mu_F}+q} dPP \\ \times &\quad \left\{ \pi\left[\ln|\rho_B^{I}| + i\pi\Theta(-\rho_B^{I})\right]_{\omega'=\omega''_{p\Gamma}} \times \left|\frac{\partial\Re\left[\Gamma^R(\mathbf{P},\omega')^{-1}\right]}{\partial\omega'}\right|^{-1}_{\omega'=\omega''_{p\Gamma}} + \right. \\ + &\quad \left. \int_{\omega_0}^{+\infty} d\omega' \Im\Gamma^R(\mathbf{P},\omega')\left[\ln|\rho_B^{I}| + i\pi\Theta(-\rho_B^{I})\right] \right\}. \end{aligned} \tag{4.27}$$

In this case we have introduced two different indices for the frequencies $\omega'_{p\Gamma}$ and $\omega''_{p\Gamma}$ to stress the fact that they arise from two different frequency integrals. Actually when $k_\Gamma < |k_{\mu_F} - q| < k_{\mu_F} + q$ we have $\omega'_{p\Gamma} \in (-\infty, \omega_0]$ and $\omega''_{p\Gamma} \in [0, \omega_0]$, when $|k_{\mu_F} - q| < k_\Gamma < k_{\mu_F} + q$ we have $\omega'_{p\Gamma} \in (-\infty, 0]$ and $\omega''_{p\Gamma} \in (-\infty, \omega_0]$, while when $|k_{\mu_F} - q| < k_{\mu_F} + q < k_\Gamma$ we have $\omega'_{p\Gamma} \in (-\infty, 0]$ and $\omega''_{p\Gamma} \in (-\infty, 0]$.

Now we can calculate the imaginary part of the Green's functions (4.3) and (4.4) in the limit $\eta \to 0^+$ and finally we can write the spectral weight functions (4.1) and (4.2) as a function of the retarded self-energies:

$$A_B(\mathbf{q},\omega) = -\frac{1}{\pi}\frac{\Im\Sigma_B^R(\mathbf{q},\omega)}{\left(\omega - \frac{\mathbf{q}^2}{m_B} + \mu_B - \Re\Sigma_B^R(\mathbf{q},\omega)\right)^2 + \Im\Sigma_B^R(\mathbf{q},\omega)^2} \tag{4.28}$$

$$A_F(\mathbf{k},\omega) = -\frac{1}{\pi}\frac{\Im\Sigma_F^R(\mathbf{k},\omega)}{\left(\omega - \mathbf{k}^2 + \mu_F - \Re\Sigma_F^R(\mathbf{k},\omega)\right)^2 + \Im\Sigma_F^R(\mathbf{k},\omega)^2}. \tag{4.29}$$

We observe that when the imaginary part of the retarded self-energy is zero, the spectral weight function, for fixed values of the momentum, can have a delta-function contribution: the bosonic one for $\omega - \frac{\mathbf{q}^2}{m_B} + \mu_B - \Re\Sigma_B^R(\mathbf{q},\omega) = 0$, while the fermionic one for $\omega - \mathbf{k}^2 + \mu_F - \Re\Sigma_F^R(\mathbf{k},\omega) = 0$. These delta-peaks of the spectral function correspond to quasi-particle exicitations with an infinite lifetime. On the other hand, when $\Im\Sigma \neq 0$, quasi-particles acquire a finite lifetime, or, alternatively, a fully incoherent spectral function occurs.

Momentum distribution functions The bosonic and the fermionic momentum distribution functions can be calculated by integrating the spectral weight functions:

$$n_B(\mathbf{q}) = \int_{-\infty}^{+\infty} d\omega \;\; b(\omega) A_B(\mathbf{q},\omega) \tag{4.30}$$

$$n_F(\mathbf{k}) = \int_{-\infty}^{+\infty} d\omega \;\; f(\omega) A_F(\mathbf{k},\omega). \tag{4.31}$$

In the zero-temperature limit the previous expressions become

$$n_B(\mathbf{q}) = -\int_{-\infty}^{0} d\omega \;\; A_B(\mathbf{q},\omega) \tag{4.32}$$

$$n_F(\mathbf{k}) = \int_{-\infty}^{0} d\omega \;\; A_F(\mathbf{k},\omega). \tag{4.33}$$

By considering the calculation of the integral around the poles of the spectral weight functions, we can distinguish the coherent and the incoherent contributions to the momentum distribution functions.

We define $\omega_{p_{A_B}}$ and $\omega_{p_{A_F}}$ the frequencies of the poles of the bosonic and fermionic spectral

weight functions, respectively, as the solutions of the two equations:

$$\omega - \frac{\mathbf{q}^2}{m_B} + \mu_B - \Re\Sigma_B^R(\mathbf{q},\omega) = 0 \tag{4.34}$$

$$\omega - \mathbf{k}^2 + \mu_F - \Re\Sigma_F^R(\mathbf{k},\omega) = 0. \tag{4.35}$$

Therefore, the polar contributions to the momentum distribution functions are given by

$$n_B^{\rm pol}(\mathbf{q}) = -\left|\frac{\partial}{\partial\omega}\Re G_B^{-1}(\mathbf{q},\omega)\right|^{-1}_{\omega_{p_{A_B}}} \tag{4.36}$$

$$n_F^{\rm pol}(\mathbf{k}) = \left|\frac{\partial}{\partial\omega}\Re G_F^{-1}(\mathbf{k},\omega)\right|^{-1}_{\omega_{p_{A_F}}}, \tag{4.37}$$

while the non-polar ones are

$$\begin{aligned} n_B^{\rm non-pol}(\mathbf{q}) &= -\int_D d\omega\ A_B(\mathbf{q},\omega) = \\ &= \frac{1}{\pi}\int_D d\omega\ \frac{\Im\Sigma_B^R(\mathbf{q},\omega)}{(\omega - \frac{\mathbf{q}^2}{m_B} + \mu_B - \Re\Sigma_B^R(\mathbf{q},\omega))^2 + \Im\Sigma_B^R(\mathbf{q},\omega)^2} \end{aligned} \tag{4.38}$$

$$\begin{aligned} n_F^{\rm non-pol}(\mathbf{k}) &= \int_D d\omega\ A_F(\mathbf{k},\omega) = \\ &= -\frac{1}{\pi}\int_D d\omega\ \frac{\Im\Sigma_F^R(\mathbf{k},\omega)}{(\omega - \mathbf{k}^2 + \mu_F - \Re\Sigma_F^R(\mathbf{k},\omega))^2 + \Im\Sigma_F^R(\mathbf{k},\omega)^2}, \end{aligned} \tag{4.39}$$

where $D = \Re^- - \left\{\omega_{p_{A_B}}\right\}$ or $D = \Re^- - \left\{\omega_{p_{A_F}}\right\}$ respectively.

Dispersions The dispersion relations of the bosons, fermions and composite fermions are obtained by considering the corresponding retarded propagators. By solving the equation $\Re\left[(G_S^R)^{-1}\right] = 0$ (where $S = B, F$) for bosons and fermions and $\Re\left[(\Gamma^R)^{-1}\right] = 0$ for composite fermions, we find the dispersion relation between the frequency and the momentum of the corresponding particle.

4.2 Spectral weight functions and dispersions

The formalism developed in the previous section allows us to calculate the spectral weight functions, the dispersions and the momentum distributions for any kind of density and mass

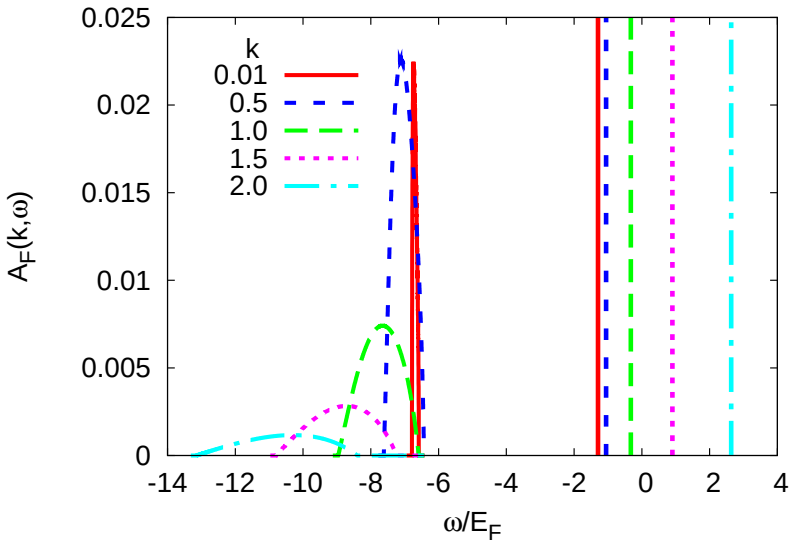

(a)

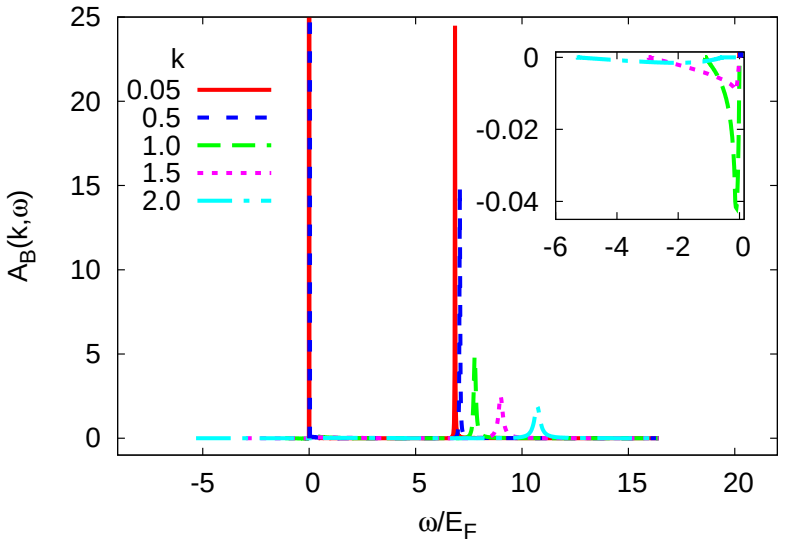

(b)

Figure 4.1: Curves of the fermionic (panel (a)) and bosonic (panel (b)) spectral weights as a function of the frequency, for different values of the momentum k, at the critical coupling $g_c = 1.713$, for $m_B/m_F = 1.0$ and fixed density imbalance $(n_F - n_B)/n = 0.75$. The inset in panel (b) shows a magnification of the negative frequency part.

imbalanced Bose-Fermi mixture, at zero temperature and couplings greater than or equal to the critical one. In this section we will show only a part of the numerical results obtained: we selected a few representative cases showing some interesting features.

Comparison of the spectral weights at the QCP We consider a Bose-Fermi mixture with equal bosonic and fermionic masses and with a density imbalance $(n_F - n_B)/n = 0.75$ at the quantum critical point $g_c = 1.713$. As we have seen in section 3.3, this system shows some remarkable features, like an empty region at small momenta in the bosonic momentum distribution and a value of the contact constant still far from the strong-coupling value. The fermionic and bosonic spectral weights, respectively represented in Fig. 4.1(a) and in Fig. 4.1(b), add more information about the behavior of this mixture close to the quantum phase transition. In Fig. 4.1(a) several curves of the fermionic spectral weights are represented as a function of the frequency, for some fixed values of the momentum. All the curves are characterized by two distinct components: the delta-like peaks, corresponding to the coherent dispersion, and the broad peaks at negative frequencies, corresponding to the incoherent part. We observe that for increasing momenta the width of the incoherent peaks increases and the delta-like peaks start to appear only in the region of positive frequencies, which does not contribute to the fermionic density. The fraction of fermions which can be considered freely propagating, i.e. associated to delta-like spectral weights, is therefore limited within a region of small momenta. By analyzing the corresponding dispersion curve we will see that this region corresponds exactly to the Fermi sphere of the unpaired fermions. The behavior of the bosonic spectral weight as a function of the frequency, for fixed values of the momentum, is shown in Fig. 4.1(b). Even if the coherent and incoherent components can still be distinguished, we observe that the delta-like peaks disappear at momenta larger than $0.5k_F$ and they are present only at positive frequencies close to zero. On the other hand the broad peaks are both in the negative and in the positive frequency regions. Contrary to the fermionic case, only the incoherent spectral weight contributes to the bosonic density, therefore no bosons propagates freely, at the quantum critical point. This result is an evidence

of the role played by the interaction in the suppression of the condensation of the bosons and of the dominant character of the statistics of the fermions, which preserve their Fermi sphere structure despite the strong interaction. Finally the inset of Fig. 4.1(b), where the negative frequency region is plotted, shows that only the curves corresponding to momenta larger than $0.5k_F$ contribute to the bosonic density, in agreement with the presence of the empty region in the momentum distribution discussed previously.

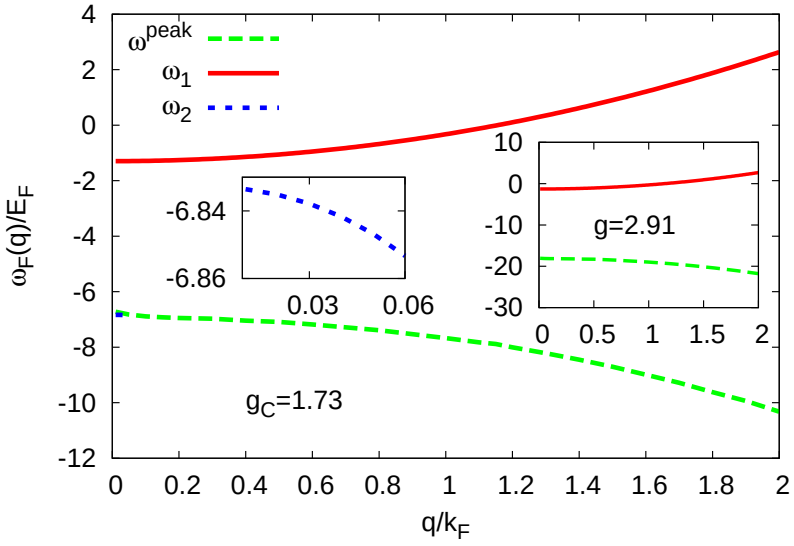

Figure 4.2: Curves of the fermionic dispersions at the critical coupling $g_c = 1.713$, for $m_B/m_F = 1$ and $(n_F - n_B)/(n_F + n_B) = 0.75$. The inset on the left is a magnification for small momenta. The inset on the right reports the fermionic dispersions for the same mixture at a larger coupling $g = 2.91$.

The curves of the fermionic dispersions for the same mixture at the critical point and in the strong coupling regime are shown in Fig. 4.2. In the main panel the three dispersion curves for the system at the critical coupling $g_C = 1.713$ are represented. The two polar dispersions ω_1 and ω_2 correspond to the poles of the spectral function at high and low frequencies, while the incoherent curve ω_{peak} is obtained by plotting the frequencies at the

maxima of the broad peaks of the spectral function. The coherent dispersion ω_1 is well fitted by the expression: $\omega(k) = \frac{k^2}{2m_F} - \mu_{UF}$, where μ_{UF} is the chemical potential of the unpaired fermions, with $k_{\mathrm{UF}} \simeq [(n_{\mathrm{F}} - n_{\mathrm{B}})/6\pi^2]^{1/3}$. The positive-frequency region of the plot describes the spectrum when a fermion is added to the system. The added fermion cannot pair with a boson, being all the bosons already paired with a fermion in such regime. For this reason the fermionic dispersion relation at $\omega > 0$ is well represented by the dispersion curve of a freely-propagating unpaired fermion (being the unpaired fermion-composite fermion interaction small with respect to μ_{UF}). The inset on the left shows the coherent dispersion ω_2 at low frequencies, which survives only in a limited region of very small momenta. When the coupling increases this secondary coherent dispersion at negative frequencies disappears. As a matter of fact, the inset on the right reports only one polar dispersion, for the system at $g = 2.91$ in the strong coupling regime.

Dispersions and weights from the critical point to strong-coupling In this paragraph we present the intensity plots for the fermionic and the bosonic spectral functions for a Bose-Fermi mixture with density imbalance $(n_F - n_B)/n = 0.75$ and equal masses, at two different values of the coupling: $g_C = 1.713$ and $g = 2.91$. We select these two coupling values to understand how the behavior of the single-particle spectral function changes when the interaction is increased from the quantum critical point towards the strong-coupling regime. The fermionic intensity plots in Fig. 4.3(a) and 4.3(b) have a simpler structure than the bosonic ones. They show a restricted region, always at negative frequencies, where the spectral weight assumes a finite value.

At small momenta the spectral weight is larger and the peaks are less broad (the intensity is always represented with a logarithmic scale). As we have seen in the previous figure, the polar dispersion is described by a parabolic curve in both the cases, and also by a second curve at very low momenta only for the system at the critical coupling. By increasing the interaction the curve of the polar dispersion does not change, while the continuum part is shifted to more negative frequencies. This is because the chemical potential of the unpaired

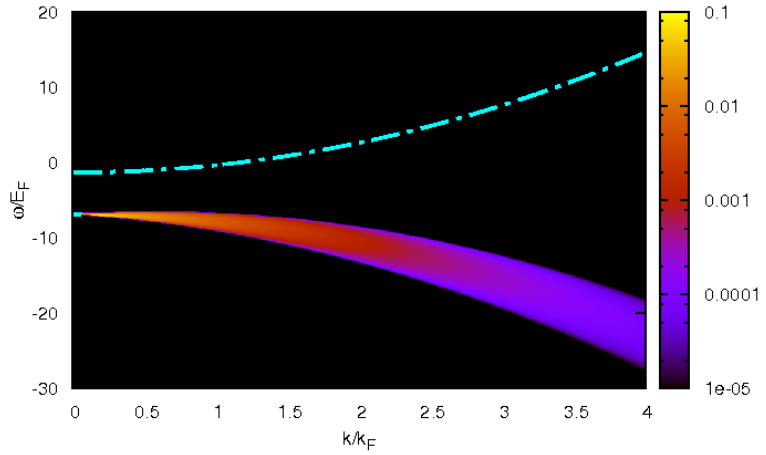

(a) $g = g_C = 1.713$

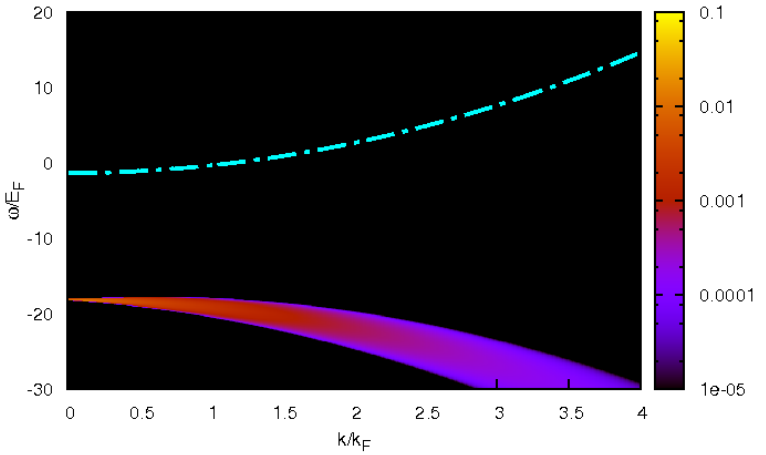

(b) $g = 2.91$

Figure 4.3: Intensity plots for the fermionic spectral function at zero temperature, for a mixture with density imbalance $(n_F - n_B)/(n_F + n_B) = 0.75$ and equal masses $m_B/m_F = 1$, at the critical coupling $g_C = 1.713$ (fig. 4.3(a)) and in the strong coupling regime at $g = 2.91$ (fig. 4.3(b)).

fermions, which determines the coherent dispersion, remains almost constant when the interaction increases (as all the bosons are already paired with a fermion at the critical coupling). Increasing the interaction determines instead an increase of the binding energy, which sets the energy scale of the incoherent part of the spectrum. Figure 4.4(a) and 4.4(b) report the intensity plots for the bosonic spectral functions for the same mixture, respectively at the critical coupling $g_C = 1.713$ and in the strong-coupling regime at $g = 2.91$. The region in which the spectral weight has a finite value is more extended than for the fermionic case. At positive frequencies we observe a well-defined curve (in yellow) corresponding to a collection of high intensity peaks in the spectral weight function. Such dispersion is associated to a well defined quasi-particle excitation which follows the free-particle dispersion function $\omega_B(k) = \frac{k^2}{2m_B} - \mu_B$ and it is therefore shifted up when the coupling increases and the absolute value of the bosonic chemical potential increases too. Another branch of coherent dispersion, but associated to delta-like peaks, is present for frequencies and momenta close to zero (with $\omega \geq 0$). It is limited to a range of very small momenta (which gets narrower when increasing the coupling). A boson added to the system with momentum close to zero and energy along this curve does not disperse. The dotted blue line that continues such a coherent curve in the continuum represents the solutions of $\Re[{G_B}^{-1}(k,\omega)] = 0$ with $\Im[\Sigma_B(k,\omega)] \neq 0$ at small frequencies. Also these low-energy peaks survive only in a small range of momenta, while the solution of $\Re[{G_B}^{-1}(k,\omega)] = 0$, which follows the free dispersion, exists for all momenta. The two remaining regions with finite weight have the same structure both in Fig. 4.4(a) and in Fig. 4.4(b), but the corresponding weights are decreasing with increasing coupling. The upper branch is a sort of continuation of the coherent dispersion, starting at $\omega = 0$, while the lower one, which bends down towards negative frequencies, is the unique part of the spectrum contributing to the bosonic density. It is associated to the removal of a single boson from the system and corresponds to the breaking of a molecule.

We can briefly summarize the behavior of a particle added to the system in this way. If a boson is added to the system, it has two possibilities: it may pair with a fermion or stay unpaired in a high-energy excited state. In the first case, at small momenta it occupies a

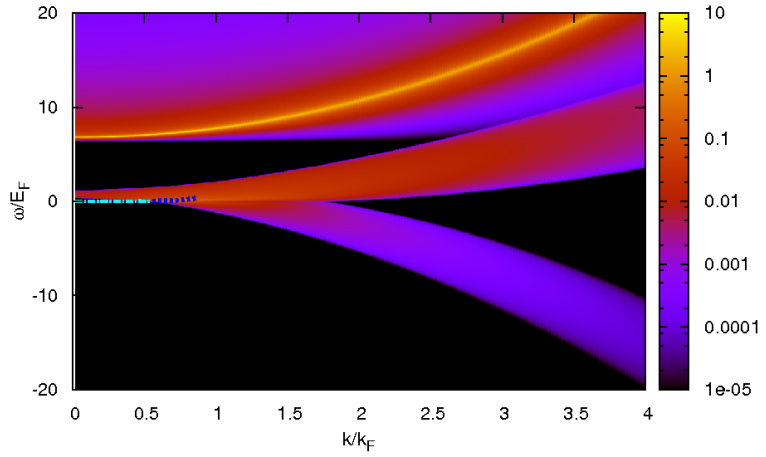

(a) $g = g_C = 1.713$ ($\mu_B(g) = \Sigma_B(0,0) = -6.42$)

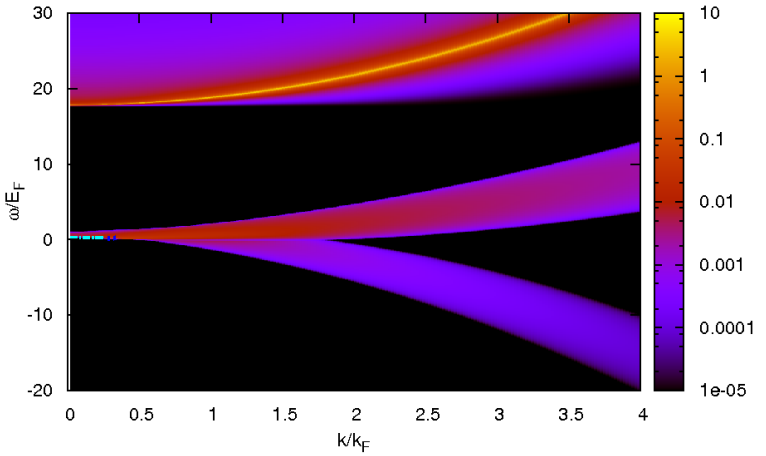

(b) $g = 2.91$ ($\mu_B(g) = -17.7,\ \Sigma_B(0,0) = -10.2$)

Figure 4.4: Intensity plots for the bosonic spectral function $\mathrm{sgn}(\omega)A_B(\mathbf{k},\omega)$ at zero temperature, for a mixture with density imbalance $(n_F - n_B)/n = 0.75$ and equal masses $m_B/m_F = 1$, at the critical coupling $g_C = 1.713$ (fig.4.4(a)) and in the strong coupling regime at $g = 2.91$ (fig.4.4(b)).

quasi-particle state with an infinite lifetime and energy close to zero. At higher momenta such quasi-particle state acquires a finite lifetime, showing then a completely inchorent dispersion. In the second case the unpaired boson disperses coherently occupying a quasi-particle state with the energy of the excitation of the (N_B+1) system. On the other hand a fermion added to the system cannot pair with a boson (because in this coupling regime we are assuming all the bosons already paired with a fermion). The added fermion will therefore occupy a quasi-particle state with an infinite lifetime and the energy of the excitation of the $(N_{UF}+1)$ system (being N_{UF} the initial number of unpaired fermions).

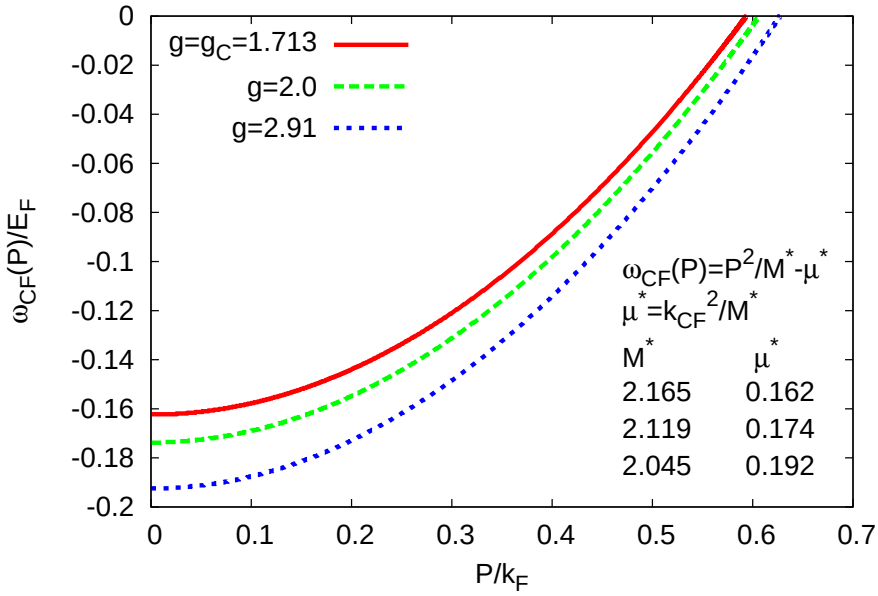

Figure 4.5: Curves of the dispersion of the composite fermion, i.e. the fermionic molecule, for different values of the coupling g, for $m_B/m_F = 1$ and for $(n_F - n_B)/n = 0.75$.

Figure 4.5 reports the dispersion of the fermionic molecules, i.e. the boson-fermion pairs, for the same mixture with $(n_F - n_B)/n = 0.75$ and $m_B/m_F = 1$, for three different values of the coupling, from the critical value to the strong-coupling regime. All curves have a parabolic dispersion, well fitted by $\omega_{CF}(P) = \frac{P^2}{2M^*} - \mu^*$, where M^* and μ^* are the effective mass and the effective chemical potential of the molecule. When increasing the coupling

strength the effective mass approaches the value of $M = 2$: the mass of the molecule is no longer dressed by the interaction and it is simply obtained by the sum of the masses of the two components. These curves have been obtained by calculating the poles of the many-body T-matrix, that reduces to the free-propagator of the molecule in the strong-coupling limit (see section 2.1). We conclude that within our formalism, in the strong-coupling regime the molecules show a free-particle dispersion.

Fermionic momentum distributions from the critical point to strong-coupling By integrating on the negative frequencies the different contributions of the spectral weight function, as described in paragraph 4.1, we can calculate the corresponding contribution to the momentum distributions separately. We consider the same Bose-Fermi mixture with $m_B/m_F = 1$ and $(n_F - n_B)/n = 0.75$ at the critical coupling $g = 1.713$, at $g = 2.0$ and at $g = 2.91$. Figure 4.6(a) and figure 4.6(b) report the contributions to the total fermionic momentum distribution coming from the "coherent" delta-like part of the spectral weight function. Panel (a) corresponds to the integration of the delta-like peak at low energy and momenta, panel (b) to the main peak, occurring at larger frequencies. The contribution coming from the incoherent part of the spectral weight function is represented in Figure 4.6(c). This part describes the momentum distribution of the fermions inside the molecules and determines the tail of the total fermionic momentum distribution function at large momenta. On the other hand, the sum of the two contributions in Fig. 4.6(a) and in Fig. 4.6(b) gives the momentum distribution of the unpaired fermions, dominated by the contribution of the coherent dispersion at higher energies. The contribution of the first coherent dispersion decreases with increasing coupling, until it disappears in the strong-coupling regime, the corresponding spectral weight being transferred to the dominant contribution.

Mass- and density-imbalance dependence at the critical point In this paragraph we analyze two sequencies of intensity plots at the quantum critical point: in the first sequence the plots for three mixtures with the same mass ratio $m_B/m_F = 1$ and different values of the

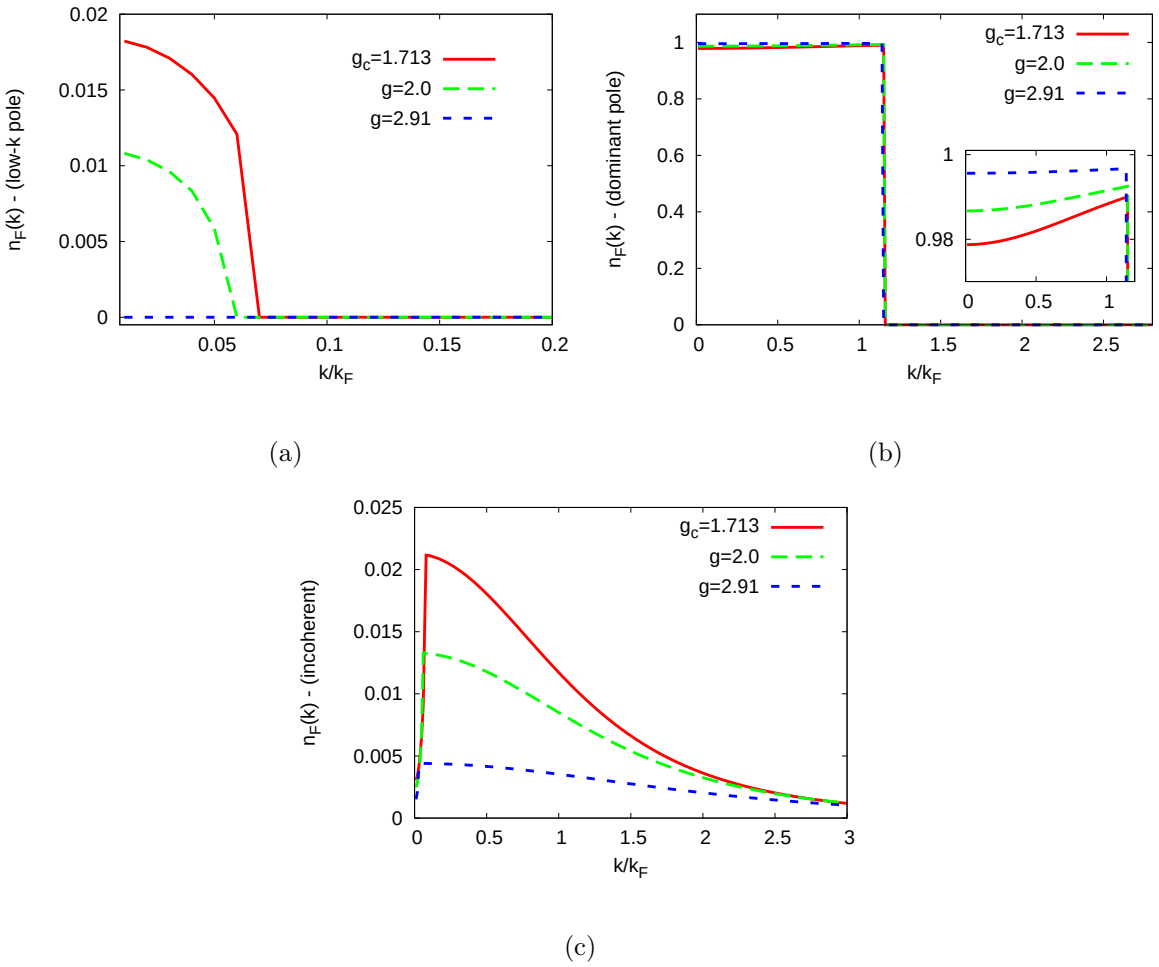

Figure 4.6: Fermionic momentum distribution functions for a mixture with density imbalance $(n_F - n_B)/n = 0.75$ and mass ratio $m_B/m_F = 1$, at three values of the coupling: the critical one $g_C = 1.713$, $g = 2.0$ and in the strong coupling regime $g = 2.91$. Three different contributions to the total momentum distribution are plotted separately: panels (a) and (b) represent the fraction of freely-propagating fermions, respectively corresponding to the low-energy and to the dominant high-energy poles of the single-particle spectral function; panel (c) represents the momentum distribution of the interacting fermions, originating from the non-polar part of the spectral function.

density imbalance $(n_F - n_B)/n = 0,\ 0.25,\ 0.5$ are presented (Fig. 4.7 and 4.8). In the second sequence we consider four mixtures with the same density imbalance $(n_F - n_B)/n = 0.75$ and different mass ratios: $m_B/m_F = 0.2,\ 0.5,\ 2.0,\ 5.0$ (Fig. 4.9, 4.10, 4.11 and 4.12). The fermionic and bosonic spectral weight functions present the same main features as for the representative intensity plots shown in the previous paragraph. We will focus thus only on the effect of the density and mass imbalances. The fermionic intensity plots represented in Fig. 4.7 do not present remarkable differences. The critical coupling and the binding energy have a weak dependence on the density imbalance, therefore the regions with a finite value of the spectral function are very similar, except for minor variations in intensity and width. The main curves of the coherent dispersion simply shift when the density imbalance is changed: they are well described by the function $\omega(k) = \frac{k^2}{2m_F} - \mu_{UF}$, where the chemical potential of the unpaired fermions μ_{UF} depends on the density imbalance as $(n_F - n_B)^{\frac{2}{3}}$.

The main difference between the bosonic intensity plots of the panels of Fig. 4.8 is the presence of one or two branches of the polar dispersion. For a density balanced mixture (Fig. 4.8(a)) a polar dispersion appears for $\omega \simeq |\mu_B|$. Close to zero frequency the blue dotted line contains the points, which are not true poles of the spectral function but satisfy the equation $\Re[G_B^{-1}(k,\omega)] = 0$ with $\Im[\Sigma_B(k,\omega)] \neq 0$. Increasing the number of fermions (see Fig. 4.8(b)) two polar branches appear, limited within a very narrow range of momenta. In Fig. 4.8(c), for a density imbalance of 0.5, the upper polar branch disappears but the lower one extends in a wider range of momenta close to zero. By increasing the density imbalance, we observe the same behavior reported in the intensity plot of Fig. 4.4(a), discussed in the previous paragraph.

Contrary to the previous sequence for the fermionic spectral function plots, which show a weak dependence on the density imbalance, the effect of the mass imbalance on the spectral weight is particularly evident in the fermionic intensity plots of Fig. 4.9 and 4.10. In the case of a mixture with a very small mass ratio of $m_B/m_F = 0.2$ (Fig. 4.9(a) and Fig. 4.9(b)) the region corresponding to the "molecular" part is shifted downwards up to frequencies of the order of $-100E_F$. This is because when decreasing the mass ratio the critical coupling

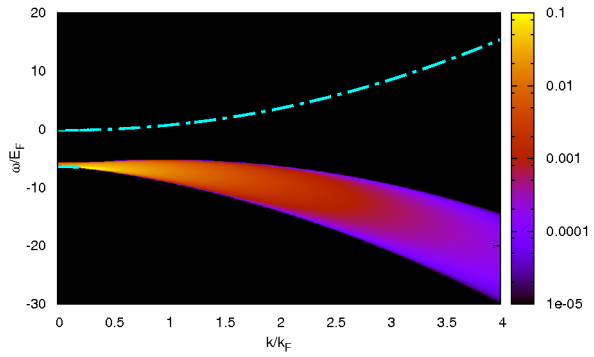

(a) $\frac{n_F - n_B}{n} = 0,\ g = g_C = 1.62$

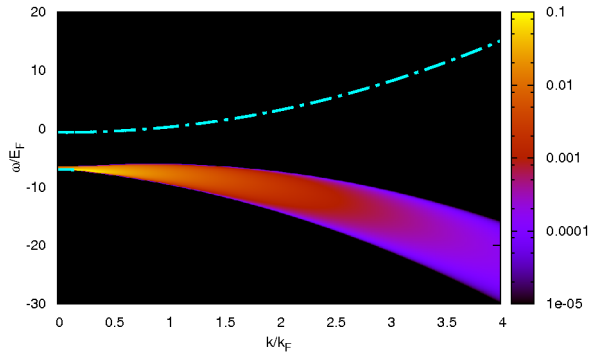

(b) $\frac{n_F - n_B}{n} = 0.25,\ g = g_C = 1.705$

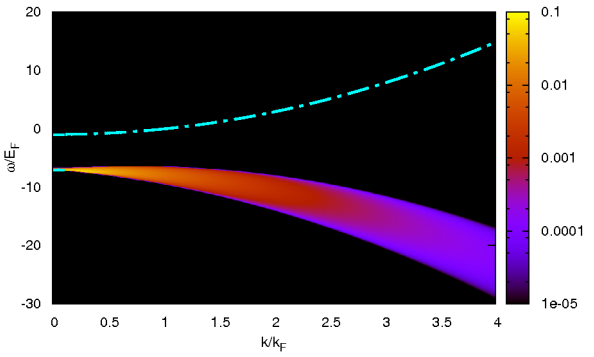

(c) $\frac{n_F - n_B}{n} = 0.5,\ g = g_C = 1.728$

Figure 4.7: Intensity plots for the fermionic spectral function at zero temperature at the QCP, for mixtures with equal masses $m_B/m_F = 1$ and different values of the density imbalance $(n_F - n_B)/n$.

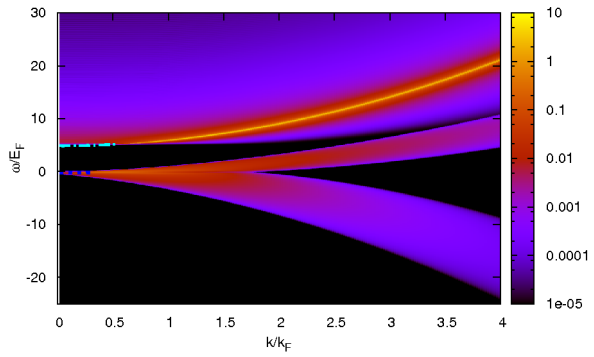

(a) $\frac{n_F - n_B}{n} = 0,\ g = g_C = 1.62,\ (\mu_B(g) = -5.19)$

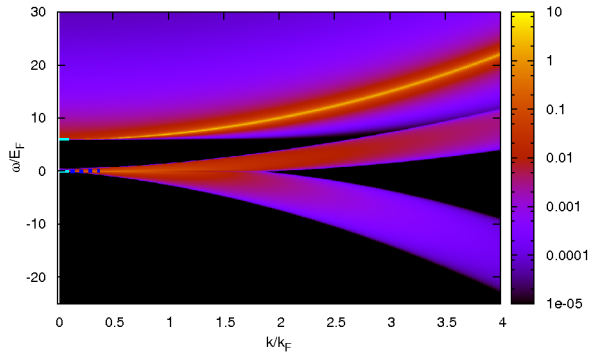

(b) $\frac{n_F - n_B}{n} = 0.25,\ g_C = 1.705,\ (\mu_B(g) = -6.01)$

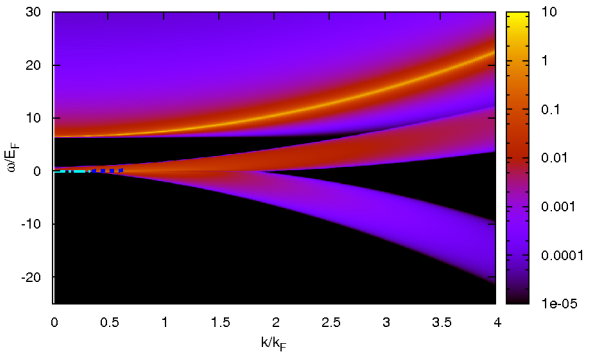

(c) $\frac{n_F - n_B}{n} = 0.5,\ g_C = 1.728,\ (\mu_B(g) = -6.36)$

Figure 4.8: Intensity plots for the bosonic spectral function $\mathrm{sgn}(\omega)A_B(\mathbf{k},\omega)$ at zero temperature at the QCP, for mixtures with equal masses $m_B/m_F = 1$ and different values of the density imbalance.

increases and consequently also the binding energy increases. The same effect can be observed in Fig. 4.9(c), where a mass ratio of $m_B/m_F = 0.5$ and a critical coupling of $g_C = 2.319$ determine a binding energy of the order of $16E_F$.

On the contrary when the mass ratio increases the critical coupling and the binding energy decrease: the incoherent weight region is shifted up to energies closer to zero (see Fig. 4.10). Also the width of the continuum part of the spectral function is strongly affected by the mass ratio. In particular this part of the spectrum gets narrower when the mass of the boson gets larger. This means that the fermion interacting with a heavy boson disperses more coherently than the fermion interacting with a light one. The dominant polar branch remains unchanged when changing the boson mass because the curve depends on the mass of the fermion and on the chemical potential of the unpaired fermions, which remains almost constant when the boson mass is changed. The mass imbalance has also an effect on the second branch of the polar dispersion. When the mass of the boson is lighter than the mass of the fermion it disappears, while it extends to larger momenta when the boson becomes heavier.

The incoherent part of the bosonic spectral weight mantains the complex structure described previously. When the mass ratio decreases the high intensity peak of the spectral function is shifted upward following the increasing value of the bosonic chemical potential. [It actually appears out of the range of frequencies plotted in Fig. 4.11(a), while it is apparent in Fig. 4.11(b).] The polar dispersion is always flat and close to zero-frequency within the same small range of momenta, which does not depend on the mass ratio.

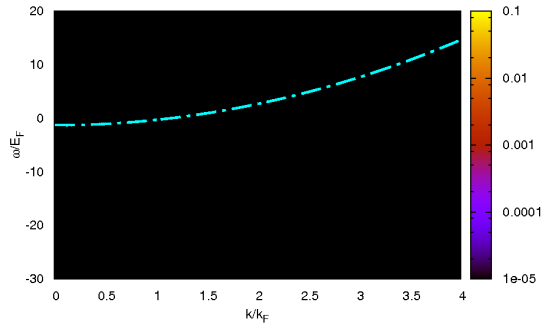

(a) $m_B/m_F = 0.2,\ g = g_C = 4.1$

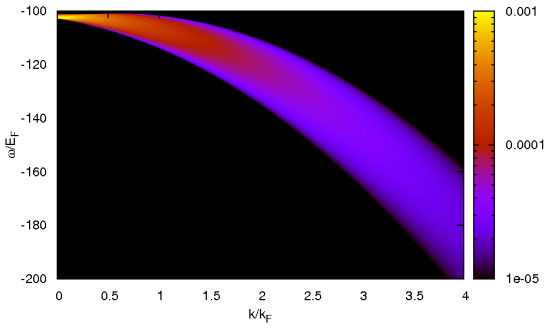

(b) $m_B/m_F = 0.2,\ g = g_C = 4.1$

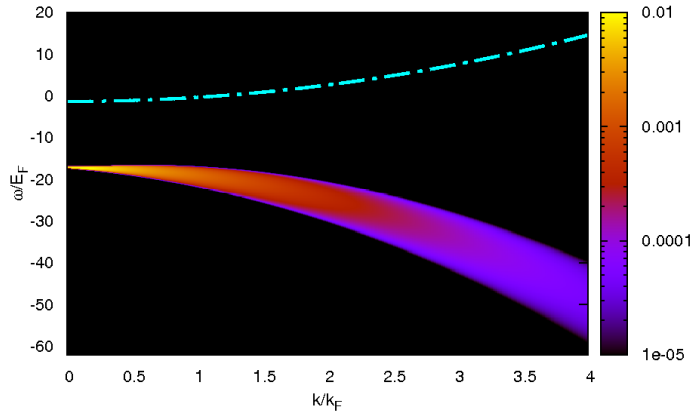

(c) $m_B/m_F = 0.5,\ g = g_C = 2.319$

Figure 4.9: Intensity plots for the fermionic spectral function at zero temperature at the QCP, for mixtures with fixed density imbalance $(n_F - n_B)/n = 0.75$ and different values of the mass ratio.

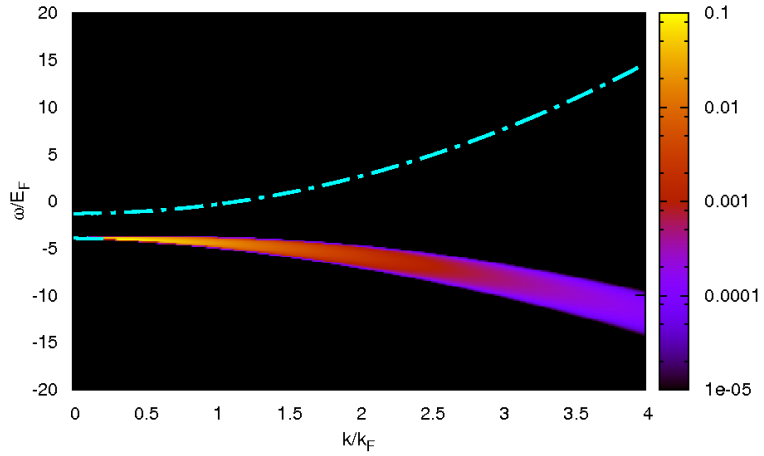

(a) $m_B/m_F = 2.0,\ g = g_C = 1.407$

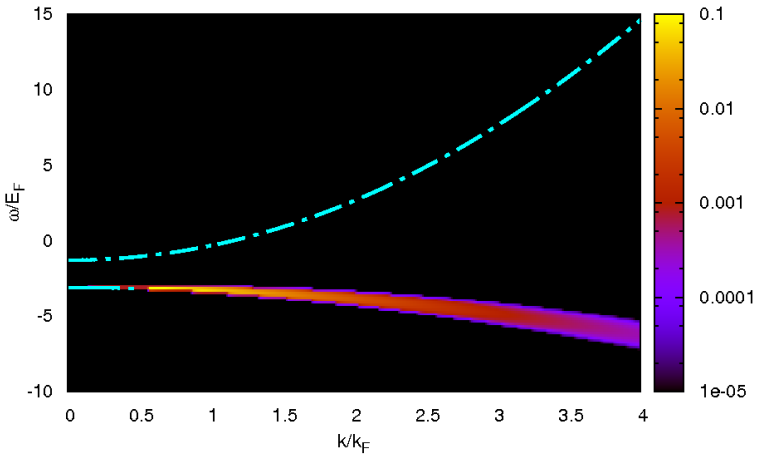

(b) $m_B/m_F = 5.0,\ g = g_C = 1.325$

Figure 4.10: Intensity plots for the fermionic spectral function at zero temperature at the QCP, for mixtures with fixed density imbalance $(n_F - n_B)/n = 0.75$ and different values of the mass ratio.

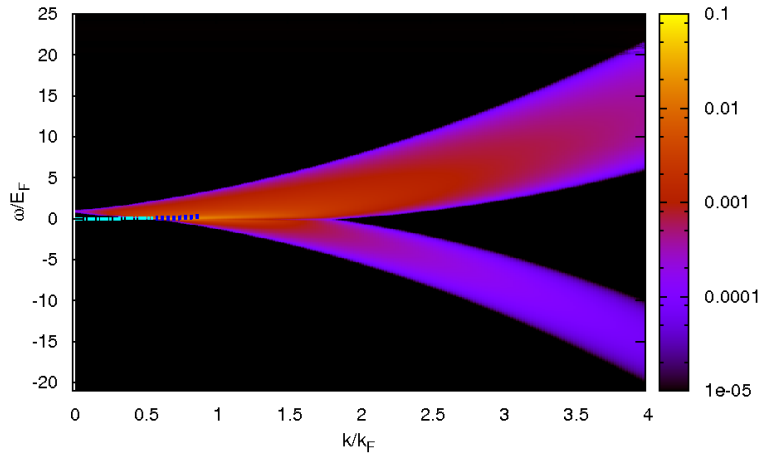

(a) $m_B/m_F = 0.2,\ g = g_C = 4.1,\ (\mu_B(g) = \Sigma_B(0,0) = -100.9)$

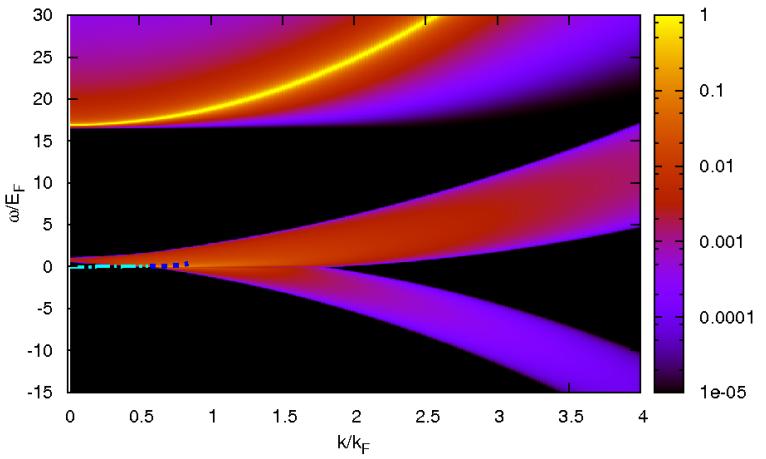

(b) $m_B/m_F = 0.5,\ g = g_C = 2.319,\ (\mu_B(g) = \Sigma_B(0,0) = -16.5)$

Figure 4.11: Intensity plots for the bosonic spectral function $\mathrm{sgn}(\omega)A_B(\mathbf{k},\omega)$ at zero temperature at the QCP, for mixtures with fixed density imbalance $(n_F - n_B)/n = 0.75$ and different values of the mass ratio.

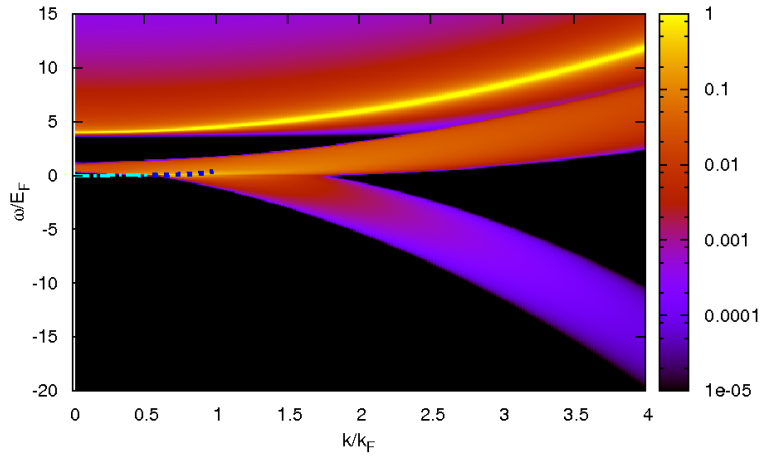

(a) $m_B/m_F = 2.0,\ g = g_C = 1.407,\ (\mu_B(g) = \Sigma_B(0,0) = -3.67)$

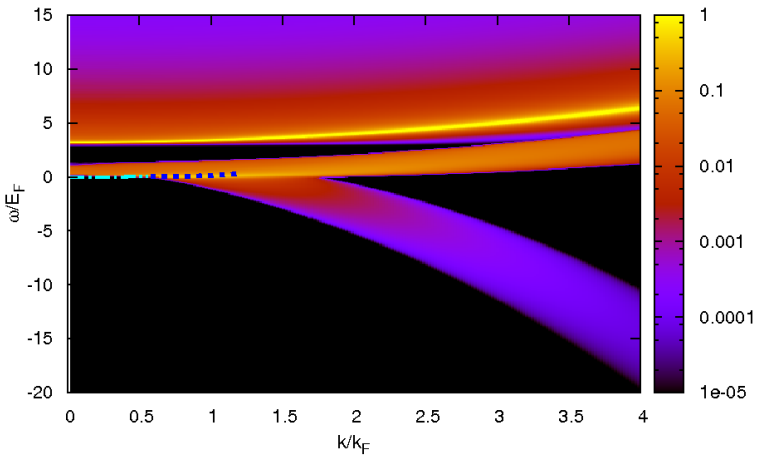

(b) $m_B/m_F = 5.0,\ g = g_C = 1.325,\ (\mu_B(g) = \Sigma_B(0,0) = -2.95)$

Figure 4.12: Intensity plots for the bosonic spectral function $\mathrm{sgn}(\omega)A_B(\mathbf{k},\omega)$ at zero temperature at the QCP, for mixtures with fixed density imbalance $(n_F - n_B)/n = 0.75$ and different values of the mass ratio.

Chapter 5

Quantum Monte Carlo study of a resonant Bose-Fermi mixture at zero-temperature

5.1 Quantum Monte Carlo method

Among all integration methods, when the dimensionality of a multiple integral is greater than some critical dimension, the Monte Carlo method is the fastest one. For this reason it is widely applied in the study of quantum many-body systems, for the calculation of the expectation values of observables which requires integration over many variables, as the energy or the correlation functions. In this case one speaks of Quantum Monte Carlo (QMC). The essence of the Monte Carlo method is to interpret multidimensional integrals as expectation values of some observables, associated to certain probability distribution functions. The observable depends on all the variables of the multidimensional integral, which are distributed in different configurations according to the probability distribution. By sampling a relevant number of points (called walkers) in the configuration space, the average of the observable calculated on the sampled walkers gives an estimate of the exact multidimensional

integral, with an intrinsic uncertainty. While the crude Monte Carlo is the plain application of the central limit theorem to the calculation of an integral with a uniform probability distribution, the importance-sampling Monte Carlo uses a non-uniform probability distribution introduced *ad hoc* (see [Gua98] for a general introduction on the method). In the latter case the integral of a generic function $h(x)$ can be written as:

$$\int h(x)dx = \int f(x)\frac{h(x)}{f(x)}dx, \tag{5.1}$$

where $f(x)$ is the probability distribution function and $\frac{h(x)}{f(x)}$ is the observable which has to be calculated on the sampled values. By using the importance sampling, it is possible to reduce the variance: if we choose a probability distribution $f(x)$ with a shape similar to the integrand $h(x)$, their ratio is smoother than the function itself.

Moreover the use of the Markov Chain Metropolis-Hastings acceptance/rejection technique [Met53, Has70] allows the sampling of arbitrary probability distribution functions. The application of the Monte Carlo method to quantum systems was developed and improved by the introduction of essentially three techniques: the Variational Monte Carlo [McM65], the Green's function Monte Carlo [Kal62, Kal70] and the Diffusion Monte Carlo [And75, Cep80, Rey82]. The Quantum Monte Carlo results that we will show in this chapter are obtained both with Variational and Diffusion Monte Carlo, therefore in the next section we will explain the essential features of these two techniques.

5.1.1 Variational and Diffusion Monte Carlo

Variational Monte Carlo (VMC) We consider a system composed by N particles: let $\mathbf{R}$ represent the set of all the coordinates of the many-body system (in dimension d, $\mathbf{R}$ will have dN components). The dynamics of the system is governed by the Hamiltonian operator $\hat{H}$, which is the sum of kinetic energy and potential energy operators. In general with the variational method, given a trial wave function $\mid \psi_c\rangle$, which can be parametrized in terms of some variational parameters c, we can find an approximate solution for the ground state of

the system:

$$E_V = \min_c \frac{\langle \psi_c \mid \hat{H} \mid \psi_c \rangle}{\langle \psi_c \mid \psi_c \rangle} \ . \tag{5.2}$$

The minimum of the expectation energy E_V, obtained by varying the parameters, is an upper bound for the ground state energy ($E_V \geq E_0$). In order to apply the Monte Carlo method to the calculation of the previous integral, we have to rewrite the integrand as a product of a new function and of the corresponding probability distribution (which represents its weight in the space of variables):

$$E_V = \min_c \frac{\int \psi_c^*(\mathbf{R}) \langle \mathbf{R} \mid \hat{H} \mid \psi \rangle_c d\mathbf{R}}{\int |\psi_c(\mathbf{R})|^2 d\mathbf{R}} = \min_c \int \frac{|\psi_c(\mathbf{R})|^2}{\int |\psi_c(\mathbf{R}')|^2 d\mathbf{R}'} E_L^c(\mathbf{R}) d\mathbf{R} \ . \tag{5.3}$$

The last expression on the right-hand side of (5.3) shows that the local energy $E_L^c(\mathbf{R}) = \langle \mathbf{R} \mid \hat{H} \mid \psi \rangle_c / \psi_c(\mathbf{R})$ is the new function, whose mean value is calculated sampling the probability distribution $p^c(\mathbf{R}) = \frac{|\psi_c(\mathbf{R})|^2}{\int |\psi_c(\mathbf{R})|^2 d\mathbf{R}}$.

We observe that with Variational Monte Carlo, Fermi systems can be treated like the Bose systems because the probability distribution is well defined even when the trial wave function is negative: the probability distribution to be sampled is essentially the square modulus of the variational wave function. The optimization of the set of parameters c is not performed directly by the Monte Carlo simulation but is obtained with standard methods. The more able we are to guess an accurate many-body wave function, the more useful and reliable the Variational Monte Carlo techinique is in the calculation of an upper bound close to the ground state energy.

Diffusion Monte Carlo (DMC) The Diffusion Monte Carlo allows to solve exactly (statistically speaking) the many-body Schrödinger equation in imaginary time, by means of a stochastic procedure. If the initial trial wave function has a non-zero overlap with the ground state, the imaginary time evolution, after a sufficiently large time, projects the trial wave function on the ground state, thanks to a faster exponential decay of all the other components. Let us consider the Schrödinger equation in imaginary time $\tau = \imath t/\hbar$, with the

initial condition $\Psi_i(\mathbf{R})$:

$$\begin{aligned} - \quad & \frac{\partial}{\partial\tau}\Psi(\mathbf{R},\tau) = \left[\hat{H}(\mathbf{R}) - E_{ref}\right]\Psi(\mathbf{R},\tau) \; ; \\ & \Psi(\mathbf{R},\tau=0) = \Psi_i(\mathbf{R}) \; ; \end{aligned} \tag{5.4}$$

where E_{ref} is a convenient reference energy, lower than the ground state energy. The initial state can be written as a linear combination of the eigenstates $\varphi_n(\mathbf{R})$ of the Hamiltonian: $\Psi_i(\mathbf{R}) = \sum_n c_n\varphi_n(\mathbf{R})$ and the solution of (5.4) is given by

$$\Psi(\mathbf{R},\tau) = \sum_n c_n e^{-\tau(E_n - E_{ref})}\varphi_n(\mathbf{R}) \xrightarrow[\tau\to\infty]{} c_0 e^{-\tau(E_0 - E_{ref})}\varphi_0(\mathbf{R}) \; . \tag{5.5}$$

We observe that the effect of the evolution is that the lowest energy components have the largest amplitudes after a long elapsed time and in the $\tau \to \infty$ limit the most important amplitude will correspond to the ground state (if in the initial state $c_0 \neq 0$). The operator $\hat{G}_0$, which gives the time evolution, is called Green's operator and is defined as:

$$\begin{aligned} \Psi(\mathbf{R},\tau) &= \hat{G}_0\Psi(\mathbf{R},0) \\ \hat{G}_0 &= e^{-\tau(\hat{H} - E_{ref})}. \end{aligned} \tag{5.6}$$

If we rewrite the solution (5.5) of the Schrödinger equation in an integral form we can apply the Monte Carlo method interpreting the wave function as a probability density which evolves in time according to the Green's function:

$$c_0 e^{-\tau(E_0 - E_{ref})}\varphi_0(\mathbf{R}') = \int \Psi_i(\mathbf{R}) G_0(\mathbf{R}\to\mathbf{R}',\tau)d\mathbf{R} \; , \quad \left(\tau \gg \frac{1}{E_1 - E_0}\right) \; , \tag{5.7}$$

where the Green's function $G_0(\mathbf{R} \to \mathbf{R}',\tau) = \langle\mathbf{R}'|\hat{G}_0|\mathbf{R}\rangle$. It is possible to estimate the transient time after which only the ground state gives a significant contribution as $\tau_t \approx \frac{1}{E_1 - E_0}$, that is the inverse of the energy gap (which we assume to be different from zero). In general it is not possible to know an explicit analytic expression for the Green's function $\hat{G}_0$, therefore an approximate Green's function is used, by performing a perturbative expansion in terms of a small time step $d\tau$. In this way the approximate Green's function can be written as

$$G_0(\mathbf{R}\to\mathbf{R}', d\tau) \xrightarrow[d\tau\to 0]{} G_K(\mathbf{R}\to\mathbf{R}', d\tau)G_V(\mathbf{R}, d\tau) \tag{5.8}$$

where G_K is the kinetic Green's function, which is used as a conditional transition probability to move the vectors $\mathbf{R}$, called walkers, and G_V the potential Green's function, which gives the probability of destruction or creation of copies of the same walker and can be interpreted as a branching factor. This is the idea behind the importance sampling algorithm applied to the DMC (see [Kal74, Cep77]). In the Diffusion Monte Carlo method the calculation of the energy is performed with a mixed estimator as follows:

$$E_M = \frac{\langle \psi_T | \hat{H} | \varphi_0 \rangle}{\langle \psi_T | \varphi_0 \rangle} = \frac{\int \psi_T^*(\mathbf{R}) E_L^T(\mathbf{R}) \varphi_0(\mathbf{R}) d\mathbf{R}}{\int \psi_T^*(\mathbf{R}) \varphi_0(\mathbf{R}) d\mathbf{R}} \,, \tag{5.9}$$

where ψ_T is the trial wave function and φ_0 is the ground state. The basic idea behind the Diffusion Monte Carlo method is the following: after having found an appropriate approximation for the short time Green's function and a starting state has been determined, the DMC algorithm consists in representing the starting state by a collection of walkers, and letting them evolve in time, i.e. obtaining a new collection of walkers from the old one, up to a time sufficiently large (transient time) so that only the ground state amplitude gives a significant contribution. For time intervals smaller than the transient one, the estimated energy is still decreasing towards an asymptotic value. For times greater than the transient one the estimated energy starts to fluctuates around such asymptotic value and the corresponding distribution of walkers has reached the convergence (i.e. the walkers are still varying but with a stable probability distribution). It is then possible to estimate the ground state energy by sampling the integral of Eq.(5.9) within such collection of walkers, as described by the following expression

$$E_M \approx \frac{\sum_i^M \psi_T(\mathbf{R_i}) E_L^T(\mathbf{R_i}) \varphi_0(\mathbf{R})}{\sum_i^M \psi_T(\mathbf{R_i})} \,, \tag{5.10}$$

where the sum runs over the whole population M of walkers at all times subsequent to the transient time. The index i associated to $\mathbf{R}$ indicates that the configuration is evolving from one time-step to another.

We observe that contrary to the VMC, in the DMC the ground state wave function and the Green's function have to be positive defined to be interpreted as a probability density

and a probability transition matrix. Another important difference is that in the VMC the probability distribution function that has to be sampled is known, because it is essentially the square of the trial wave function; in the DMC the probability distribution is not known, because it is evolving, but we know how to sample it following its evolution, thanks to the Green's function operator. According to the importance sampling algorithm, the quantity to sample is now $p(\mathbf{R}) = \psi_T^* \Psi$, where Ψ is the evolved wave function: this choice makes it necessary to treat the fermionic systems in a different way, since $\psi_T^* \Psi$ is not necessary ≥ 0. One of the possible approaches, that allows to apply the DMC also to antisymmetric (real) wave functions, is the Fixed Node approximation. This technique consists in fixing the nodal surface of the wave function Ψ to be equal to that of the trial wave function ψ_T, so that the nodal pockets of Ψ and ψ_T coincide. The probability distribution $p(\mathbf{R}) = \psi_T \Psi$ turns to be everywhere positive, except on the nodal surface, so that the usual bosonic algorithm can be applied, provided that the nodal surface is never crossed. This method provides an upper bound for the energy of the lowest lying state with the same symmetries of the trial wave function [Cep80, Rey82]. In the general case, when the wave function is not real, it is possible to use an analogous techinique called Fixed-phase approximation.

Trial wave functions An important step in the implementation of a Quantum Monte Carlo simulation for the study of a dilute system is the choice of a good trial wave function, which has to be as closer as possible to the ground state solution, especially when considering fermionic systems. The trial wave function used to describe a dilute system of bosons in the ground state is the Jastrow wave function [McM65, Gio99]. For fermions, the Slater [Cep77] or the BCS determinants [Bou88, Car03, Ast04] provide an accurate description of the nodal surface. The Jastrow wave function is a symmetrized product of few-body wave functions; in the simplest case we consider only the two-body terms and we have: $\Psi_J(\mathbf{R}) = \prod_{i<j} f(r_{ij})$, where $r_{ij} = |r_i - r_j|$ is the relative coordinate and in the case of short range interactions, f is the solution of the two-body problem.

The simplest antisymmetric wave function describing an ideal Fermi gas is the Slater determi-

nant, namely an antisymmetric product of non-interacting single-particle wave functions. In order to take into account the effect of interaction, a more refined wave function is used: the Jastrow-Slater. For a system of spin-up and spin-down fermions, for example, the Jastrow-Slater wave function is given by the product of the Slater determinants of the spin-up and of the spin-down ideal Fermi gases and the Jastrow function, representing the interaction between a spin-up and spin-down fermion. Another more accurate description of attractive fermionic systems is obtained with the BCS wave function, which provides a nodal surface able to account for pairing effects. The BCS wave function is given by the determinant of the matrix composed by all the possible pair orbitals, depending on the relative coordinate of two different scattering fermions. In the case of a polarized system of spin-up and spin-down fermions a generalized BCS wave function, with both two-body wave functions and plane waves as matrix elements, has been successfully used in the context of ^{3}He [Bou88] and for studying ultracold gases [Car03, Pil08].

5.2 Quantum Monte Carlo formalism for a resonant Bose-Fermi mixture

We consider a three-dimensional homogeneous Bose-Fermi gas described by the Hamiltonian

$$H = -\frac{\hbar^2}{2m_F}\sum_{i=1}^{N_F}\nabla_i^2 - \frac{\hbar^2}{2m_B}\sum_{i'=1}^{N_B}\nabla_{i'}^2 + \sum_{i,i'}V_{BF}(r_{ii'}) + \sum_{i'<j'}V_{BB}(r_{i'j'})\ , \tag{5.11}$$

where $i, j, ...$ and $i', j', ...$ label, respectively, the fermions and the bosons. We consider equal masses $m_B = m_F = m$ and model the interspecies boson-fermion (BF) interaction using an attractive square-well (SW) potential: $V_{BF}(r) = -V_{BF}^0$ for $r < R_{BF}$ ($V_{BF}^0 > 0$), and $V_{BF}(r) = 0$ otherwise.

The intra-species boson-boson interaction, which is not contained in the Hamiltonian (2.1) of the T-matrix approach, is modeled by a repulsive soft-sphere (SS) potential: $V_{BB}(r) = V_{BB}^0$ for $r < R_{BB}$ ($V_{BB}^0 > 0$), and $V_{BB}(r) = 0$ otherwise.

The scattering lengths of the BF and BB interactions are given, respectively, by $a_{BF} = R_{BF}(1-\tan(\kappa_{BF})/\kappa_{BF})$, where $\kappa_{BF} = \sqrt{mV^0_{BF}R^2_{BF}/\hbar^2}$, and $a_{BB} = R_{BB}(1-\tanh(\kappa_{BB})/\kappa_{BB})$, with $\kappa_{BB} = \sqrt{mV^0_{BB}R^2_{BB}/\hbar^2}$. In order to eliminate any dependence on the range of the BF interaction potential we have taken R_{BF} such that $n_F R^3_{BF} = 10^{-7}$, where n_F is the fermion number density, or equivalently $k_F R_{BF} = 0.0181$ in terms of the Fermi wave vector $k_F = (6\pi^2 n_F)^{1/3}$.[Note that in this chapter k_F is defined with the density of the fermions and not with the total density of the system, as in the previous chapters.] Therefore the only dependence on the BF interaction potential is given by the scattering length a_{BF}. As in previous chapters, the BF coupling strength is conveniently described in terms of the dimensionless parameter $g = (k_F a_{BF})^{-1}$.

Some BB repulsion is expected to be necessary to ensure the mechanical stability of the Bose-Fermi mixture across the BF resonance [Lud11, Yu11]. Contrary to the T-matrix calculation developed in the previous chpaters, in which the boson-boson repulsion has been neglected (provided that the compressibility remains positive), the QMC simulation requires to be applied in a mechanically stable regime to reach the convergence. In our calculations we have chosen a boson-boson repulsion $\zeta \equiv k_F a_{BB} = 1$, twice the critical value for stability found in [Yu11] at unitarity. Such a constant BB repulsion has guaranteed the stability for all values of the boson concentration $x = n_B/n_F$, from $x = 0$ to $x = 1$, and all BF couplings across the resonance. We did not try to minimize the BB repulsion necessary for stability, due to computational time constraints. This question is however definitively relevant for experiments with ultracold atoms, since typical values of a_{BB} and k_F correspond to values of ζ smaller by at least one order of magnitude than the value considered here (unless a resonance in the boson-boson channel would be accidentally close to that in the BF channel). In addition, a smaller value of ζ would extend the universal region of the phase diagram. With $\zeta = 1$ we expect in fact a dependence on the specific choice of the BB potential to show up at $x \gtrsim 0.2$, based on previous studies of bosonic systems [Gio99, Pil08b]. In this work we set $R_{BB} = 1.086 a_{BB}$.

In the weakly interacting regime we expect the ground state to be the coexistence of a con-

densate of N_B bosons and a Fermi sphere containing the N_F bare fermions, characterized by the Fermi momentum k_F. In the strongly interacting regime, we expect that each boson is bound to a fermion into a fermionic molecule, so that two Fermi spheres emerge: one composed by $N_M = N_B$ molecules and characterized by a Fermi momentum $K_M = (6\pi^2 n_M)^{1/3}$ and the other one by the remaining $N_U = N_F - N_B$ unpaired fermions, with a Fermi momentum $k_U = (6\pi^2 n_U)^{1/3}$. In this molecular regime the condensate fraction of the bosons is zero by definition, due to the molecular Pauli principle. Thus we expect a quantum phase transition (QPT) from a phase with a condensate to a phase without, occurring at an intermediate coupling.

Simulations are carried out in a cubic box of volume $L^3 = N_F/n_F$ with periodic boundary conditions, using the Fixed-Node Diffusion Monte Carlo (FN-DMC) method. The boundary condition is enforced using a trial function that we choose of the general form $\psi_T(\mathbf{R}) = \Phi_S(\mathbf{R})\Phi_A(\mathbf{R})$. Φ_S is a positive function of the particle coordinates $\mathbf{R} = (\mathbf{R_F}, \mathbf{R_B}) = (\mathbf{r}_1, ..., \mathbf{r}_{N_F}, \mathbf{r}_{1'}, ..., \mathbf{r}_{N'_B})$ and is symmetric in the exchange of particles of the same species, while Φ_A satisfies the fermionic antisymmetry condition and determines the nodal surface of ψ_T. The symmetric part is chosen of the Jastrow form $\Phi_S(\mathbf{R}) = \prod_{i,i'} f_{BF}(r_{ii'}) \prod_{i'j'} f_{BB}(r_{i'j'})$, where two-body correlation functions of the interparticle distance have been introduced.
In order to describe the condensate and the molecular ground states, we have chosen two different Φ_A components, one for the weakly- and one for the strongly-interacting regimes introduced above.

5.2.1 Weak and strong-coupling trial wave functions for a resonant Bose-Fermi mixture

The weak-coupling trial wave function (JS), describing the condensate ground state, is a Slater determinant for the bare fermions $\Phi_A^S(\mathbf{R}_F) = \mathcal{A}\left(\psi_{k_1}(1)\psi_{k_2}(2)...\psi_{k_{N_F}}(N_F)\right)$, where $\mathcal{A}$ indicates the antisymmetrizer operator and $\psi_{k_\alpha}(i)$ indicates the plane-wave states in the

simulation box, with $k_\alpha = 2\pi(n_{\alpha x}\hat{x} + n_{\alpha y}\hat{y} + n_{\alpha z}\hat{z})/L$.

The strong-coupling trial wave function (JMS), describing the molecular ground state, is the antisymmetrized product of a Slater determinant for the molecules and a Slater determinant for the unpaired fermions

$$\Phi_A^{MS}(\mathbf{R}) = \det \begin{pmatrix} \varphi_{K_1}(1,1') & \cdots & \varphi_{K_1}(N_F,1') \\ \vdots & \ddots & \vdots \\ \varphi_{K_{N_M}}(1,N_M{}') & \cdots & \varphi_{K_{N_M}}(N_F,N_M{}') \\ \psi_{k_1}(1) & \cdots & \psi_{k_1}(N_F) \\ \vdots & \ddots & \vdots \\ \psi_{k_{N_U}}(1) & \cdots & \psi_{k_{N_U}}(N_F) \end{pmatrix}. \tag{5.12}$$

The molecular orbitals are defined as $\varphi_{K_\alpha}(i,i') = f_b(|\mathbf{r}_i - \mathbf{r}_{i'}|)\exp\left(i\mathbf{K}_\alpha(\mathbf{r}_i + \mathbf{r}_{i'})/2\right)$ and consist of the relative motion orbitals f_b times the molecular center-of-mass plane-waves with $|K_\alpha| \leq K_M$, $n_M = K_M^3/6\pi^2$, while for the unpaired fermions $|k_\alpha| \leq k_U$, $n_U = k_U^3/6\pi^2$. The functions f_b, as f_{BB} and f_{BF}, are taken to be the solutions of the appropriate two-body problems, modified at long distance so as to fulfill periodic boundary conditions. The many-body wave function (5.12) is not symmetric under the exchange of the bosonic coordinates, since each boson i corresponds to a definite molecular orbital K_α, but it is well known that the DMC method gives the exact ground state energy for bosons, necessarily corresponding to a symmetric wave function (provided the trial wave function has some overlap with the ground state). Moreover the many-body wave function (5.12) is the analogous of the Nosanow-Jastrow wave function [Nos64, Han68], which has been successfully used in studies of the equation of state of solid Helium [Whi79, Caz09].

In order to explicitly enforce the bosonic symmetry one should sum the wave function (5.12) over all the permutations of bosonic coordinates. Contrary to the calculation of the energy, the many-body wave function Φ_A^{MS} has to be symmetrized with respect to the bosonic coordinates for the calculation of "non-pure" estimators, as the momentum distributions and correlation functions. In this way the exact strong-coupling trial wave function becomes the

sum of all the $N_B!$ possible wave functions $\Phi_A^{MS^{(b)}}$, where (b) indicates a different permutation of the N_B bosons in the determinant of (5.12). The use of a trial wave function composed by such a large number of Slater determinants is too computationally demanding. For this reason, for the calculation of non-pure estimators, we have resorted to an approximate strong-coupling wave function (5.13), where the sum over the bosonic coordinates has been included inside the molecular orbitals of a unique Slater determinant:

$$\tilde{\Phi}_A^{MS}(\mathbf{R}) = \det \begin{pmatrix} \varphi_{K_1}(1,\mathbf{R}_B) & \cdots & \varphi_{K_1}(N_F,\mathbf{R}_B) \\ \vdots & \ddots & \vdots \\ \varphi_{K_{N_M}}(1,\mathbf{R}_B) & \cdots & \varphi_{K_{N_M}}(N_F,\mathbf{R}_B) \\ \psi_{k_1}(1) & \cdots & \psi_{k_1}(N_F) \\ \vdots & \ddots & \vdots \\ \psi_{k_{N_U}}(1) & \cdots & \psi_{k_{N_U}}(N_F) \end{pmatrix} \tag{5.13}$$

where $\varphi_{K_\alpha}(i,\mathbf{R}_B) = \sum_{i'} \varphi_{K_\alpha}(i,i')$.

This approximate wave function takes into account all the possible dispositions with repetition of the bosonic coordinates, therefore it contains all the terms of the exact antisymmetrized strong-coupling wave function plus some spurious terms that are negligible in the very strong-coupling regime (in general they could be forced to be negligible by adding a fictious repulsive Fermi-Fermi Jastrow factor). We have checked that, despite the presence of such spurious terms, the FN-DMC energy calculated with the approximate trial wave function (5.13) is compatible with that of (5.12), within error-bars.

5.3 Quantum Phase Transition and Phase Separation

Thanks to the results obtained with QMC simulations, we will try to understand the nature of the quantum phase transition and discuss the existence of phase separation in resonant Bose-Fermi mixtures.

5.3.1 Equation of state

In Fig. 5.1 we report the Fixed-Node Diffusion Monte Carlo (FN-DMC) results for the total energy (divided by N_F) at a small boson concentration $x = 0.175$ as a function of the interaction parameter g in units of the energy per particle of the free Fermi gas $E_{\rm FG} = 3\hbar^2 k_F^2/10m = 3\varepsilon_F/5$, where ε_F is the Fermi energy. We have performed calculations with $N_F = 57$, $N_B = 10$ for the JS nodal surface and with $N_F = 40$, $N_B = 7$ with the JMS wave function, in order to have almost the same boson-fermion concentration and closed shells in the two regimes. For the JS (JMS) nodal surface finite-size effects are considerably reduced by using closed shells for the number of fermions (molecules and unpaired fermions) and profiting of Fermi liquid theory. The energy difference between the finite and infinite system, is assumed to be the same as for the noninteracting case, to lowest order in the effective mass (see [Lin01] for details). This correction has been used to assess also the error-bars, on top of the statistical error.

In the weak-coupling limit we recover the perturbative results of Refs.[Viv02, Alb02], which can be further expanded in powers of x, leading to the energy functional $E = E_{\rm FG} N_F \left[\mathcal{E}_{BF}(g,\zeta,x) + \mathcal{E}_{BB}(\zeta,x)\right]$, where

$$\mathcal{E}_{BF}(g,\zeta,x) = 1 + \frac{20}{9\pi g} x \left(1 + \frac{1}{\pi g}\right) + \frac{10\zeta x^2}{9\pi g^2}\left(1 + \frac{4}{\pi^2}\right) \tag{5.14}$$

and $\mathcal{E}_{BB}$ is the energy of a weakly interacting Bose gas (Lee-Huang-Yang expansion [Gio99]) given by

$$\mathcal{E}_{BB}(\zeta,x) = \frac{10\zeta x^2}{9\pi}\left(1 + \sqrt{x}\zeta^{3/2}\frac{128}{15\pi\sqrt{6\pi}}\right) . \tag{5.15}$$

More generally, the condensate phase can be described in terms of a *polaronic* picture, where bosons are dressed by fermions. These polarons are characterized by an effective binding energy A and an interaction term F. Similarly to [Yu11] one can thus introduce the following polaronic equation of state (EOS) $E_{pol} = N_F E_{FG} \mathcal{E}_P$ where

$$\mathcal{E}_P = 1 - A(g)x + F(g,\zeta)x^2 . \tag{5.16}$$

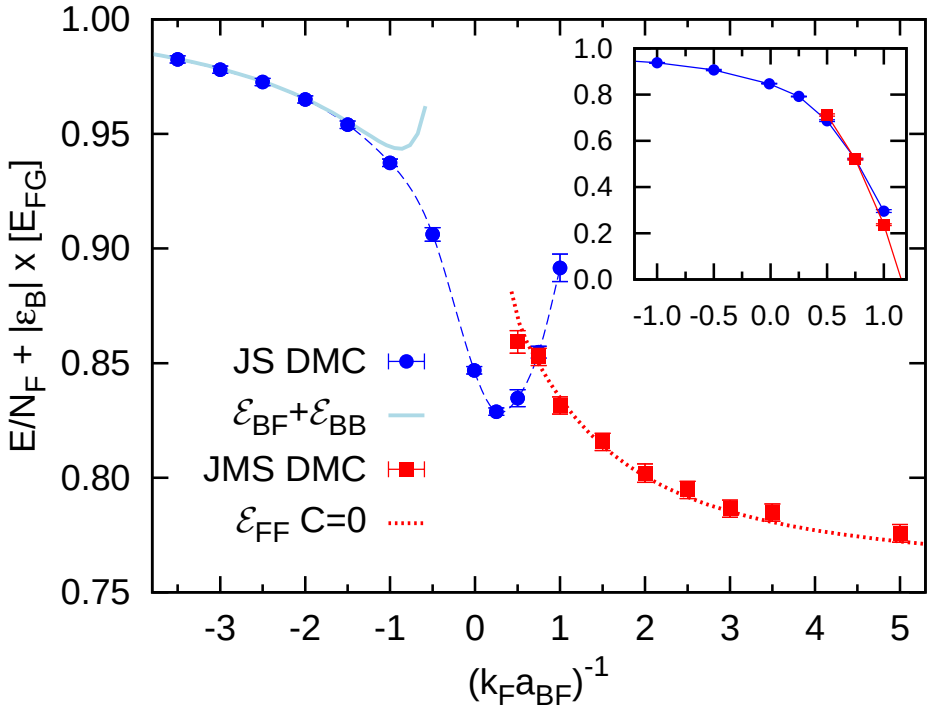

Figure 5.1: Energy of a BF mixture at $x = 0.175$ and $\zeta = 1$, with the contribution of the bare binding energy of the molecules subtracted for $a_{BF} > 0$. Circles: JS FN-DMC results. The solid line corresponds to eqs. (5.14)- (5.15) and the dashed line is a guide to the eyes. Squares: JMS FN-DMC results. The dotted line corresponds to eq. (5.17) with M^* and α from [Com09] and $C = 0$. Inset: Energy without subtracting the bare binding energy.

The polaron binding energy $A(g) = -\mu_B/E_{FG}|_{x\to 0}$ is calculated by using the one-boson limit of our T-matrix theory (see section 3.4), μ_B being the chemical potential of the bosons, while $F(g,\zeta) = \frac{10\zeta}{9\pi}(1 + D(g,\zeta))$. An analogous (x^2) interaction term has been considered in the context of polarized Fermi gases [Mor10, Yu10, Gir12]. As a simple assumption one can take $D(g,\zeta) = \frac{9}{100}\left(1 + \frac{\pi^2}{4}\right)(2A - A'g)^2$, as a generalization of the perturbative limit where $D = \frac{1}{g^2}\left(1 + \frac{4}{\pi^2}\right)$ and $2A - A'g \simeq 20/3\pi g$. This approximate EOS compares rather well with the FN-DMC data for $x = 0.175$ also in the strongly interacting regime, as can be seen in Fig. 5.1. When constructing the phase diagram (see section 5.4) we will however fit the coefficient D directly from our numerical results obtained for several values of x in the

relevant regime of couplings $0 \leq g \leq 1$.

Results for the polaronic branch are shown in the inset of Fig. 5.2; in Table 5.1 we report the fitted values for D. The agreement with the polaronic EOS is rather good even at large concentrations. Some discrepancies start to appear at large x for $g = 0.75$.

Moreover in Fig. 5.1 we compare the FN-DMC results with the JMS wave function to the energy functional (normalized to $N_F E_{FG}$) $\mathcal{E}_{mol}(g, \zeta, x) = -\frac{10x}{3g^2} + \mathcal{E}_{FF}(g, x)$, where the first contribution comes from the bare binding energy of the molecules and

$$\mathcal{E}_{FF} = \frac{m}{M^*(g)}[1 + xC(g, \zeta)]x^{5/3} + (1 - x)^{5/3} + x(1 - x)\frac{5\alpha(g)}{3\pi g} , \tag{5.17}$$

which is expected to hold for large values of g. Here, the first term corresponds to the kinetic energy of the molecules, whose effective mass is given by $M^*(g)$, taken from the analytic treatment of [Com09] for a single molecule in a Fermi sea, corrected by a term proportional to the coefficient C for finite values of x. This higher order $x^{8/3}$ contribution could also embody a p-wave interaction between the molecules, which is expected to be significant for $\zeta = 1$. The second and third terms correspond instead to the kinetic energy of the unpaired fermions and to the interaction energy of the two fermionic components which, at the level of mean-field theory, is proportional to the ratio $\alpha = a_{ad}/a_{BF}$ of the atom-dimer to the BF scattering length; the $g-$dependence of this coefficient is taken from [Com09] and in the strong coupling limit correctly reduces to the value $\alpha = 1.18$ obtained from the solution of the three-body problem [Sko56, Pet04]. At the small value of $x = 0.175$ shown in Fig. 5.1, the FN-DMC results well compare with the EOS (5.17) with $C = 0$.

Analogously to the polaronic branch, we perform simulations using the JMS wave function for $g \geq 0.6$ and different concentrations of the bosons. Results of the molecular FF mixture are shown in Fig. 5.2. For the three largest values of g we find that the EOS in eq. (5.17), including the correction to M^* linear in x, accurately describes the dependence of the energy on the concentration of bosons up to $x = 1$. The corresponding best fitted values of the coefficient C are reported in Table 5.1. For $g = 0.6$, our results start showing some deviations from the functional form (5.17) in the regime of intermediate concentrations $0.5 \leq x \leq 0.8$.

For even smaller values of g a number of effects worsen the agreement with the FN-DMC data: i) the molecular effective mass from [Com09] diverges for $g \simeq 0.5$, indicating that a molecular picture is not valid anymore, ii) beyond mean-field interaction terms for the FF mixture are probably relevant and iii) the composite nature of the molecules should start to play a major role.

Table 5.1: $D(g,\zeta)$ coefficient of the polaronic EOS (5.16) and $C(g,\zeta)$ coefficient of the molecular EOS (5.17) for $\zeta = 1$.

g	D	g	C
0.00	0.99(1)	0.60	12.39(10)
0.25	1.33(5)	0.75	3.37(2)
0.50	1.75(5)	1.00	1.54(2)
0.75	1.95(5)	5.00	0.60(1)
1.00	1.25(1)		

5.3.2 Condensate fraction

The calculation of the condensate fraction n_0 has been developed both with the JS and the JSM trial wave functions. For the polaronic phase one can calculate n_0 by extrapolating the long-tail part of the bosonic one-body density matrix from FN-DMC and VMC simulations. The results for $x = 0.175$ are reported in Fig. 5.3 and show a constant decrease of n_0 from the weakly interacting regime, where the only contribution to depletion comes from the BB repulsion, to the strongly interacting regime, where the BF interaction dominates. In this region however the extrapolation starts to become inaccurate so that it is not possible to assess whether n_0 goes exactly to zero; it is reasonable to assume that a small but finite condensate fraction is always present in this branch. The calculation of n_0 for the JMS nodal surface is even more delicate, since this trial wave function is not symmetric under

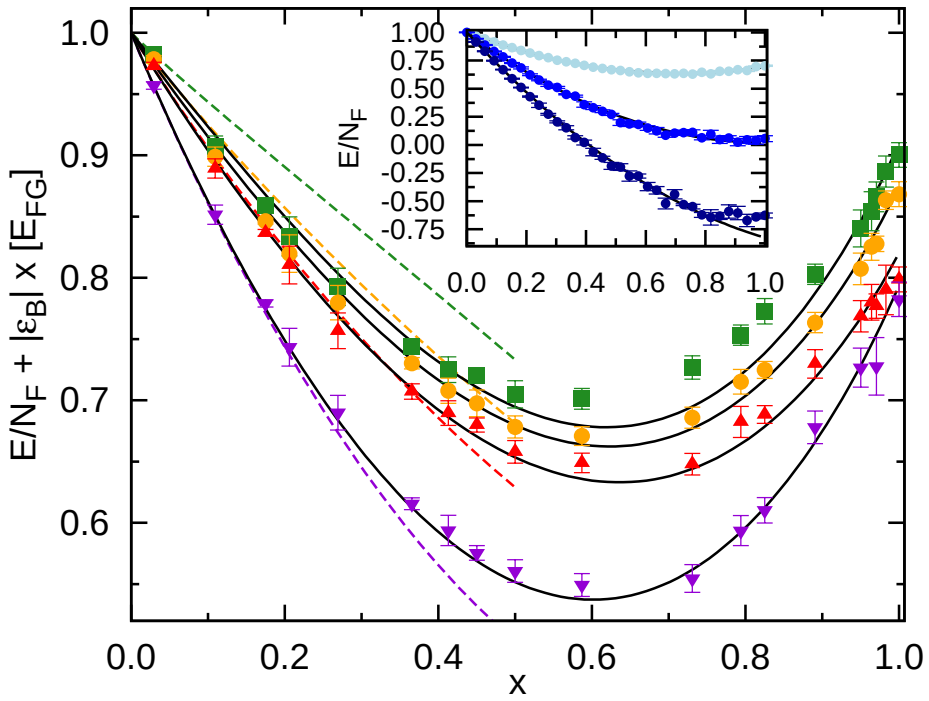

Figure 5.2: Energy as a function of x, for $\zeta = 1$. Main figure, from top to bottom: energy of the FF mixture at $g = 0.6$, $g = 0.75$, $g = 1$ and $g = 5$, with the bare binding energy of the molecules subtracted. Dashed lines: eq. (5.17) with $C = 0$, $M^* = 2m$ and $\alpha = 1.18$. Solid lines: best fit using eq. (5.17) with M^* and α from [Com09]. Inset, from top to bottom: energy of the polaronic phase at $g = 0$, $g = 0.5$ and $g = 0.75$. Solid lines: best fit using eq. (5.16).

boson permutation. Since a sum of (5.12) over all possible permutations of bosons is out of numerical reach, we resorted to a sum over all dispositions with repetition of the bosons (5.13), which is equivalent to symmetrizing the molecular orbitals over the bosons within the same determinant. The FN-DMC energy of this new nodal surface is compatible with that of (5.12), within error-bars. Spurious delocalizing terms are however introduced by such approximate procedure, which are negligible in the very strong coupling regime, where we get indeed $n_0 = 0$ within error-bars, but become important close to the transition, where we cannot therefore determine n_0 properly. We consider however the validation of eq. (5.17), which is not compatible with a finite condensate fraction, as an indirect indication that

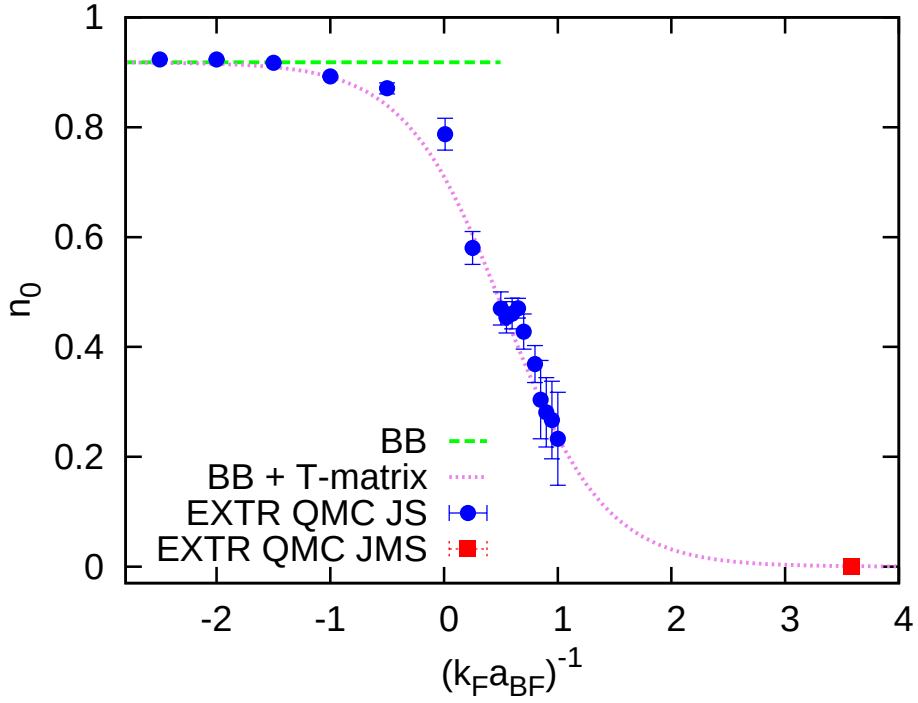

Figure 5.3: Condensate fraction n_0 for $x = 0.175$. Circles: extrapolated results for the polaronic phase, from JS FN-DMC and VMC simulations. Dashed line: weakly-interacting Bose gas result $n_0^B = 1 - 8/3\sqrt{(x\zeta^3)/(6\pi^3)}$. Dotted line: quasiparticle weight of the polaron at $x = 0$, calculated within T-matrix approximation [Pun09] times n_0^B. The large error-bars for $g > 0.5$ are due to the extrapolation method. The square indicates the result for n_0 at $g = 3.58$ for the symmetrized molecular JMS nodal surface (see text).

$n_0 = 0$ in the molecular phase, as also expected on physical grounds.

5.3.3 Phase diagram

The two phases studied with our QMC simulations are the superfluid (polaronic) and normal (molecular) phase. In this section we will use the equations of state of both such phases to determine for which values of the boson-fermion coupling g and concentration x the system is in one phase or the other, or if the two phases coexist in phase separation.

We use the equation of state (5.18) (equivalent to (5.16)) to describe the **superfluid phase (SF)**, composed by a gas of bosonic polarons immersed in a Fermi sea. The expression for the energy density ε^{SF}, obtained from an expansion up to the second order in the concentration of the bosons x, is given by:

$$\varepsilon^{SF} = \frac{3}{5}\varepsilon_F n_F \left\{1 - A(g)x + \frac{10}{9\pi}\zeta x^2 \left[1 + D_{SF}(g,\zeta)\right]\right\} , \tag{5.18}$$

where $A(g)$ is the binding energy of the polarons calculated in the T-matrix approximation. The coefficient $D_{SF}(g,\zeta)$ is extrapolated from the QMC data as it follows.
We consider a fixed value of the boson-boson scattering length $\zeta = 1.0$, large enough to guarantee stability to the system. By fitting the QMC results for the equation of state of mixtures at different couplings $g = 0.5,\ 0.75,\ 1.0$, we get the corresponding values of D_{SF} (see Table 5.1). In order to obtain an expression depending on g for the coefficient D_{SF}, we express it as the product of two functions of g: $D_{SF}(g) = C_{SF}(g)F(g)$. The function $F(g) = \left(1 + \frac{\pi^2}{4}\right)\frac{9}{100}\left[A'(g)g - 2A(g)\right]^2$ represents the induced term coming from the coupling to the Fermi sea, in a gas of bosonic polarons. We assume that the behavior of the function $D_{SF}(g)$ is similar to $F(g)$, then we express the ratio between $D_{SF}(g)$ and $F(g)$ with the function $C_{SF}(g)$. By calculating such ratio for the three coefficients D_{SF}, obtained from the QMC data, and fitting them with a parabolic function, we get an expression for $C_{SF}(g)$. Starting from $D_{SF}(0.5) = 1.75(5)$, $D_{SF}(0.75) = 1.95(5)$, $D_{SF}(1.0) = 1.25(1)$ we obtain

$$D_{SF}(g) = \frac{9}{100}\left(1 + \frac{\pi^2}{4}\right)\left(-1.35g^2 + 1.836g - 0.352\right)\left[A'(g)g - 2A(g)\right]^2 . \tag{5.19}$$

In the **normal phase (N)** the system can be described as a mixture of fermionic molecules and unpaired fermions and we assume that the condensate fraction is zero. For sufficiently large values of the boson-fermion coupling we observe that the QMC data for the energy density are well fitted by an equation of state of the following form

$$\begin{aligned}\varepsilon^N \;=\; & \frac{3}{5}\varepsilon_F n_F \left\{\varepsilon_b(g)x + \frac{m}{M^*(g)}x^{5/3}\left[1 + C_N(g,\zeta)x\right] + \right. \\ & \left. (1-x)^{5/3} + x(1-x)\frac{5}{3\pi}\frac{\alpha(g)}{g}\right\} ,\end{aligned} \tag{5.20}$$

where the first term is the bare binding energy of the molecules where $\varepsilon_b(g) = -\frac{10}{3}g^2$. As we have already seen in eq.(5.17), the energy of the Fermi sea of the molecules is composed by two terms: the first one has a basic $x^{5/3}$ dependence, while the second one is proportional to $x^{8/3}$ and embodies a possible p-wave interaction between the molecules.
The effective mass of the molecules M^* depends on g as $\frac{m_F}{M^*(g)} = \frac{1}{2} + \frac{m_0}{(g-g_0)^3}$, where $m_0 = -0.670124$ and $g_0 = -0.55755$. Such expression, taken from the results of [Com09], is valid at concentration $x = 0$. It is therefore necessary to introduce a x dependence to the effective mass, in order to bring it from the value at zero concentration to the value $M^* \sim 2$ at $x = 1$.
Also the expression for the $g-$dependence of the coefficient α is taken from [Com09] and it is approximated by $(1.18g^3 + a_2 g + a_3)/(g^3 + b_1 g^2 + b_2 g)$, where $a_2 = 3.00408$, $a_3 = -0.444911$, $b_1 = -0.35545$ and $b_2 = 2.48564$.
By fitting QMC results with the equation of state (5.20) at different couplings ($g = 0.6,\ 0.75,\ 1.0$) and always with a fixed boson-boson interaction $\zeta = 1.0$, we obtain three values for the coefficient C_N (see Table 5.1). Then we include in the same coefficient $N(g)$ both the dependence of the molecular mass and of C_N on g at $x = 1$: $N(g) = (C_N(g) + 1)\frac{m_F}{M*(g)}$. By calculating $N(g)$ for $g = 0.6,\ 0.75,\ 1.0$ and fitting such points with two lines, we get an expression for $N(g)$. We can now express the coefficient C_N as:

$$C_N(g) = N(g)\frac{M^*(g)}{m_F} - 1\ . \tag{5.21}$$

Starting from $C_N(0.6) = 12.39(10)$, $C_N(0.75) = 3.37(2)$, $C_N(1.0) = 1.54(2)$ we get:
$N(g) = -0.232(g - 0.6) + 0.9098 \qquad$ if $g \leq 0.75$,
$N(g) = -0.222(g - 0.75) + 0.875 \qquad$ if $g > 0.75$.

In the **phase separated (PS)** region the two phases coexist: a part of the system is in the normal phase, the remainder in the superfluid phase. If the total volume is V and V_N is the volume occupied by the normal phase, we call v_N their ratio: $v_N = \frac{V_N}{V}$. The fraction of the volume occupied by the superfluid phase is $(1 - v_N)$. The total energy density of the system with phase separation is therefore given by the sum of the superfluid and normal

energy densities:

$$\varepsilon^{PS}(g,x) = min\left[(1-v_N)\varepsilon^{SF}(g_{SF},x_{SF}) + v_N\varepsilon^{N}(g_N,x_N)\right] \ , \tag{5.22}$$

where ε^{SF} and ε^{N} are respectively given by (5.18) and (5.20). For each fixed value of the coupling g and concentration x there are infinitely many phase separated states with local couplings and concentrations of the superfluid and normal coexisting phases, respectively given by $g_{SF} = (k_F^{SF}a_{BF})^{-1}$, $x_{SF} = \frac{n_B^{SF}}{n_F^{SF}}$, $g_N = (k_F^N a_{BF})^{-1}$ and $x_N = \frac{n_B^N}{n_F^N}$. If a phase separated state exists, its energy density has to assume the minimum value among all the possible phase separated configurations. In principle the energy density of such separated configurations depends on five variables: v_N, g_{SF}, x_{SF}, g_N, x_N, or equivalently on v_N and the bosonic and fermionic densities in the two coexisting phases. By introducing the constraints on the total number of bosons and fermions in the total volume V, which correspond to certain fixed values of $g = (k_F a_{BF})^{-1}$ and $x = \frac{n_B}{n_F}$, we get an expression for the energy density depending only on three variables. We express the local couplings g_{SF} and g_N as a function of v_N, x_{SF} and x_N:

$$g_{SF} = g(1-v_N)^{\frac{1}{3}}\left(\frac{x_{SF}-x_N}{x-x_N}\right)^{\frac{1}{3}} \tag{5.23}$$

$$g_N = g(v_N)^{\frac{1}{3}}\left(\frac{x_{SF}-x_N}{x_{SF}-x}\right)^{\frac{1}{3}} \ , \tag{5.24}$$

with two constraints: $x_{SF} \leq x \leq x_N$ or $x_N \leq x \leq x_{SF}$, which guarantee that the arguments within the cubic roots are positive and correspond to the positivity of the local densities. Then we minimize the energy density of the phase separated state with respect to v_N, x_{SF} and x_N. In order to obtain a phase diagram in the g-x plane, we calculate the superfluid (5.18), the normal (5.20) and the phase separated (5.22) equations of state, increasing g at fixed values of the total concentration of the bosons x. By comparing the energies of the three phases we obtain the phase diagram of Fig. 5.4. In this figure, the x-range of the phase diagram has been limited to $x \leq 0.4$, where we are confident in the validity of the energy functionals (5.18) and (5.20).

We observe the appearence of a narrow region of phase separation between the superfluid

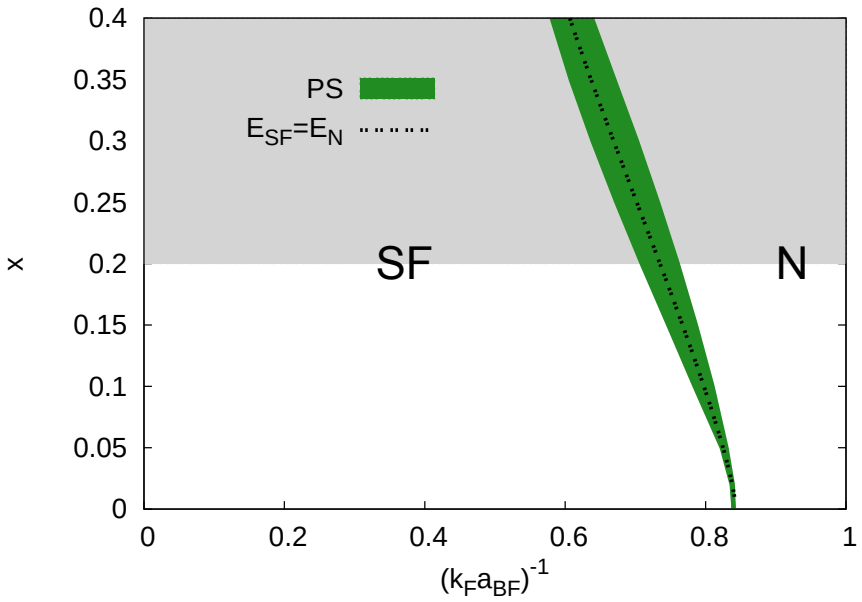

Figure 5.4: Phase diagram in the g-x plane, for $\zeta = 1.0$. The green area represents the region with phase separation. Along the black dotted line the energy of the system in the superfluid phase is equal to the energy of the system in the normal phase. The gray area above $x \simeq 0.2$ indicates the non-universal region for $\zeta = 1.0$.

(SF) and normal (N) phase. The dotted curve corresponds to the energy-crossing between these two phases. We have checked that, also in the phase separated region, at equilibrium, the resulting local couplings and concentrations lie in the respective regions of validity of the two energy functionals. The upper part of the phase diagram in gray, above $x \simeq 0.2$, represents the region of non-universality, where, for $\zeta = 1.0$, our results depend on the choice of the specific boson-boson potential.

Our FN-DMC calculations support then the scenario of a first-order quantum phase transition, with a phase separation region intervening between the condensed and molecular phase. The quite narrow width of the phase separation region that we found could however indicate also that, by improving the choice of the trial wave functions, phase separation could eventually disappear and the quantum phase transition become second order, a scenario that

thus we do not exclude at present.

In any event, the width of the phase separation region shrinks to zero in the limit $x \to 0$, where the transition line tends to the critical coupling for the polaron-molecule transition, previously studied in the context of polarized Fermi gases. In the present case, the polaron-molecule transition is thus not masked by a large phase separation region, with finite width even in the limit $x \to 0$, as it occurs instead in Fermi gases. In our system, the polaron-molecule transition is connected then continuously to a quantum phase transition occurring at *finite* boson concentration, thus making it really relevant and observable in the many-body system.

Boson-boson coupling effect In the previous calculations the boson-boson scattering length has been fixed at $\zeta = 1.0$ in all the equations of state. In the phase separated case the superfluid and normal energy densities in (5.22) depend respectively on the local couplings g_{SF} and g_N and not on the global one g, while the boson-boson coupling assumes always the same value $\zeta^{-1} = 1.0$, independently from the local momenta k_{SF} and k_N. In order to justify such approximation we have verified that the local boson-boson couplings $(k_{SF}a_{BB})^{-1}$ and $(k_N a_{BB})^{-1}$ are very close to the global one, with a maximum error of 3%. Both the coefficients D_{SF} and C_N depend on the coupling g and on the boson-boson coupling ζ^{-1}. In order to observe the effect of the boson-boson coupling dependence of such coefficients on the phase diagram, we consider the case $\zeta = 0.25$. By introducing the corresponding new coefficients $D_{SF}(g, \zeta = 0.25)$ and $C_N(g, \zeta = 0.25)$, we get the energy-crossing line ($E_{SF} = E_N$) represented by the green curve in Fig. 5.5. The expression for the coefficient $C_N(g, \zeta = 0.25)$ has been obtained with a linear extrapolation from QMC data at $\zeta = 1.0$ and the values at $\zeta = 0$ (where $N(g)$ is fixed to 0.5). On the other hand, for the coefficient $D_{SF}(g, \zeta = 0.25)$, we have introduced a reasonable $\frac{1}{\zeta}$ dependence, observed with a QMC simulation at $g = 0.5$. The green curve of Fig.5.5, obtained in this way, is quite close to the blue one, which represents the energy-crossing line for $\zeta = 1.0$. By fixing $\zeta = 0.25$ but neglecting the dependence of D_{SF} on ζ, we obtain the curve in red: we observe that

the dependence of D_{SF} on ζ has a crucial effect in determining the behavior of the curve. Finally the pink line comes from an approximate solution for small values of x, in which we have neglected the second (and higher) order terms in x, in the equations of state (5.18) and (5.20). Such curve, independent from ζ, has a completely different behavior from the blue and green ones, where the dependence on ζ has been taken into account.

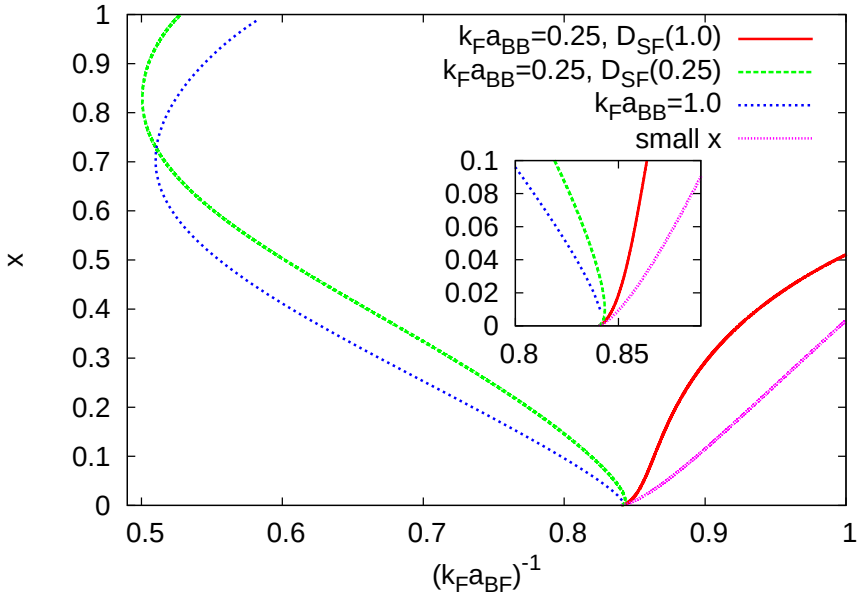

Figure 5.5: Coexistence curves of the superfluid and the normal phases ($E_{SF} = E_N$). In red and green the curves with $\zeta = 0.25$, where the red one has been obtained neglecting the ζ dependence of D_{SF}. The blue line represents the case with $\zeta = 1.0$. The pink curve shows the asymptotic behavior for small values of x, which is independent from ζ.

Errors Finally it is necessary to point out that the phase diagram in Fig. 5.4 has been obtained with the QMC coefficients D_{SF} and C_N, without errors. In order to take into account the uncertainty in such coefficients and then the error propagation in the derivation of the phase diagram, we have repeated the calculation getting two other phase diagrams. By using the smallest coefficients D_{SF} and the largest coefficients C_N within the errorbars,

we obtain a phase diagram where the superfluid phase is favored at most. Viceversa, with the largest D_{SF} and the smallest C_N, we get a phase diagram where the normal phase is favored at most. We have observed that the introduction of the uncertainty in the QMC coefficients D_{SF} and C_N determines a small effect on the phase diagram: the region of phase separation is shifted to larger couplings (in the first case) or to smaller ones (in the second), but in both cases it mantains the same shape and a large overlap with the original phase separated region. For this reason in Fig 5.4 we represent only one phase diagram, without the errors.

Itinerant ferromagnetism Another possible scenario, that has to be taken into account, is the appearance of a phase separation in the normal phase: when all the bosons are paired with a fermion we can have a homogeneous gas composed by fermionic molecules and unpaired fermions, described by the equation of state (5.20), or the coexistence of a gas of molecules in a fraction of the total volume and a gas of unpaired fermions in the remainder. When the system is in the latter configuration, we can speak about an itinerant ferromagnetic phase, generalized to the case in which the two fermionic species have a different mass. The equation of state used to describe such itinerant ferromagnetic phase is the following:

$$\varepsilon^{IF} = min\left[(1-v_N)\varepsilon^{SF}(x_{SF}=0) + v_N\varepsilon^{N}(x_N=1)\right] \ , \tag{5.25}$$

where we assume that the superfluid phase with $n_B^{SF}=0$ corresponds to the gas of unpaired fermions, while the gas of molecules can be represented by the normal phase with $n_B = n_F$. By calculating the equation of state of the non-homogeneous normal phase and comparing it with the energy of the corresponding homogeneous normal phase, we find that $\varepsilon^N(g,x) < \varepsilon^{IF}(g,x)$. We can therefore exclude the presence of the itinerant ferromagnetism in the normal phase, close to the phase separated region.

5.4 Comparison between QMC and T-matrix results

The T-matrix approach developed in chapters 2 and 3 predicts a quantum phase transition from a condensed to a normal phase in resonant Bose-Fermi mixtures with different density and mass imbalances. The critical coupling g_C derived within this formalism in the zero-temperature limit, represents, for each value of the density imbalance (or equivalently of the bosonic concentration x) the smallest value of the boson-fermion attraction at which the system is still in the normal phase, i.e. without a Bose-Einstein condensate. We can therefore interpret the curve $x(g_C)$ represented in Fig 5.6 as a line of separation between the normal and superfluid phase and compare it with the phase diagram obtained with the QMC simulations. In Fig. 5.6 we present the QMC phase diagram of Fig. 5.4 extending the x-range up to $x = 1$, in order to have a wider picture of the comparison with the T-matrix results, even if the validity of the QMC energy functionals is guaranteed only up to $x = 0.4$. The data of the curve $x(g_C)$ have already been shown in Fig. 3.2, where the critical coupling, measured in unity of $(3\pi^2 n)^{1/3}$, is represented as a function of the density imbalance $(n_F - n_B)/n$ for a mixture with $m_B = m_F$. The two lines of separation in Fig 5.6, the dotted black and the solid red one, are visibly different: the first one goes towards smaller critical couplings increasing the concentration, the second has the opposite behavior. We can attribute this different trend to the effect of the boson-boson interaction. While the QMC data are obtained with a large boson-boson repulsion $\zeta = 1.0$, the T-matrix results describe a mixture with $\zeta = 0$. As a matter of fact, if we consider the pink curve represented in Fig. 5.5, derived within an approximation valid for small x and independent from ζ, we observe the same increasing trend of the T-matrix red curve of Fig 5.6. Moreover the critical coupling derived within the T-matrix approach is always larger than the corresponding QMC value, because the T-matrix formalism overestimates the repulsion between the composite fermions and the unpaired fermions, by keeping the "Born" approximation value of $8/3a_{BF}$ for the dimer-atom scattering length.

In Fig. 5.7 we report the bosonic momentum distribution in the strong-coupling regime

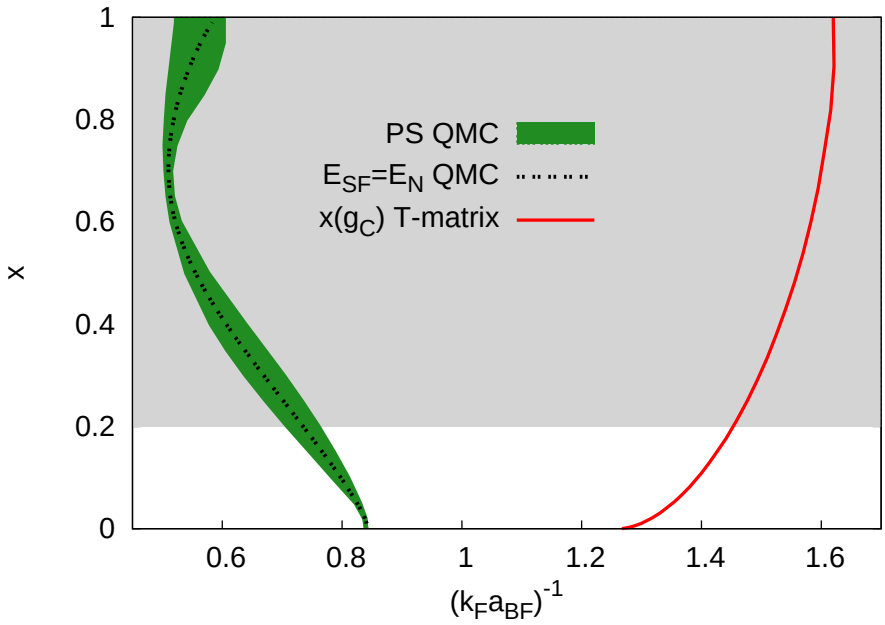

Figure 5.6: Phase diagram in the g-x plane. The region of phase separation (in green) and the energy-crossing line $E_{SF} = E_N$ (black dotted) are obtained with the equations of state from the QMC data, for $\zeta = 1.0$. The curve in red represents the concentration x as a function of the critical coupling g_C, derived within the T-matrix formalism in the zero-temperature limit for $\zeta = 0$ (see chapter 3).

for the same mixture of Fig.5.1. For this value of the density imbalance the T-matrix calculations predict an empty region, as discussed previously in section 3.3.

We observe an excellent agreement between the QMC results and the corresponding curve calculated within the T-matrix approximation (dashed curve). This shows that the T-matrix is quite accurate in describing the internal structure of the molecule forming in the medium (while it is less accurate in describing the interaction between the molecule and the unpaired fermions, yielding the "Born" approximation value $8/3a_{BF}$ for the dimer-atom scattering length instead of the value $1.18a_{BF}$ in the strong-coupling regime).

These two representative comparisons between T-matrix and QMC results lead us to con-

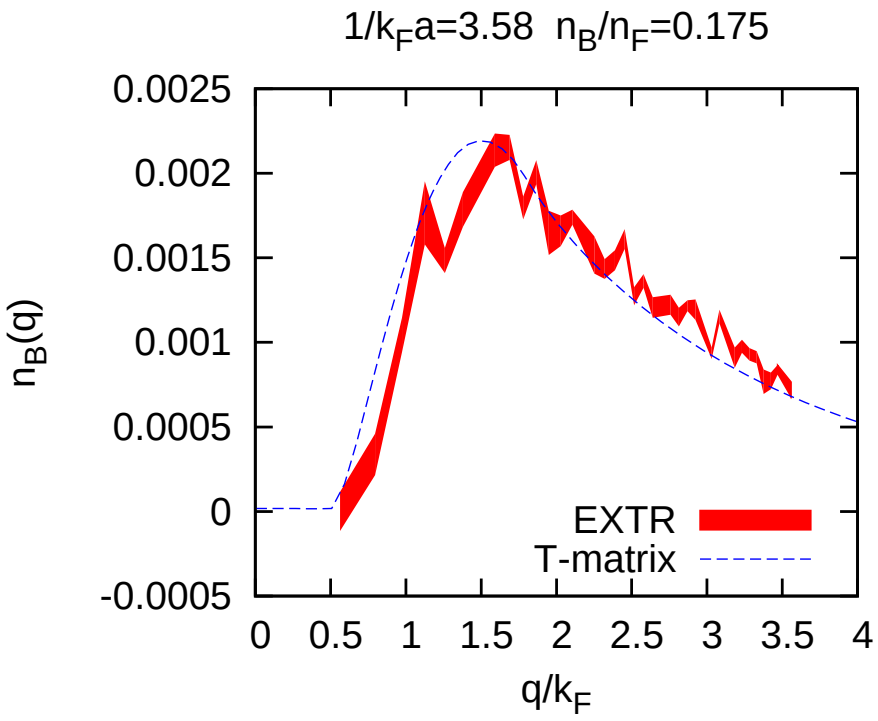

Figure 5.7: Bosonic momentum distribution function in the strong-coupling regime, for a mixture with boson-fermion concentration $x = 0.175$ and coupling $g = 3.58$. The QMC extrapolated results (solid line) are compared with the corresponding T-matrix curve (dashed line).

clude that the two approaches developed in this thesis work are both useful and complementary, in order to study resont Bose-Fermi mixtures. Starting from a simpler model valid only in the normal phase, the diagrammatic calculation shows us the presence of a quantum phase transition, providing a good qualitative description of the behavior of the system close to criticality. Then the introduction of a boson-boson repulsion, which guarantees stability to the system, provides a more refined model for the system and the use of the QMC method allows the calculation of the equation of state both in the condensate and normal phase. The improvements introduced by the QMC approach are based on a good prior knowledge of the qualitative behavior of the system. The calculation of important quantities as the

condensate fraction or the momentum distributions are strictly related to the choice of good trial wave functions, whose nodal surfaces have to be as close as possible to the real ground state. For this reason, it is necessary to have a comparison between QMC data and other expressions or results, in order to validate and eventually improve the choice of the trial wave function. Moreover in some cases, the QMC simulation seems to be more numerically demanding and less accurate than the T-matrix calculation, as it has been previuosly shown for the bosonic momentum distribution.

Conclusions

This thesis' work investigates theoretically the behavior of a novel interesting system in the field of ultracold gases: the resonant Bose-Fermi mixture. Two substantially different approaches have been used to study homogeneous resonant Bose-Fermi mixtures with density and mass imbalances: the many-body diagrammatic theory in T-matrix approximation and the Quantum Monte Carlo method with Fixed Node approximation. Both theoretical frameworks have provided good models and reliable calculations, allowing us to explore in detail the system.

The T-matrix and QMC results are in agreement, although they should be interpreted within their confidence limits. While the diagrammatic calculation explores the normal phase, both at finite and zero-temperature, the QMC study is developed at zero-temperature from the weakly- to the strongly-interacting regime, i.e. from the condensed to the normal phase.

The goal reached in this thesis' work is to address some fundamental issues about the physical behavior of resonant Bose-Fermi mixtures. What is the effect on the condensation temperature of the attractive interaction between the bosons and the fermions? Is there a quantum phase transition between the condensed and the normal phase? Of which order? How does such critical point depend on the density and mass imbalances? What is the behavior of the bosons and the fermions close to criticality and in the strongly-interacting regime?

The presence of a quantum phase transition from a condensed to a normal phase is an evidence confirmed by both the calculations, even if the specific values of the critical coupling are different because of the different approximations considered. From the T-matrix results we can conclude that when increasing the boson-fermion attraction the condensation temperature decreases until the condensate is completely depleted by pairing, at a critical

coupling and zero-temperature. For couplings larger than the critical one, all the bosons are paired with a fermion and the system can be described by two Fermi spheres, one for the molecules and one for the unpaired fermions. The value of the critical coupling has a weak dependence on the density imbalance and a strong dependence on the mass ratio. In the weakly-interacting regime the system can be described in terms of bosonic polarons. The equation of state is derived with QMC simulations in both the regimes.

The condensate fraction decreases when increasing the coupling strength, but the QMC results do not allow to assess whether it goes exactly to zero. By comparing the energies of the superfluid (polaronic) and normal (molecular) phases as a function of the boson-fermion coupling g and bosonic concentration x, we have derived a phase diagram in the g-x plane. A very narrow region of phase separation emerges between the two phases and its width shrinks to zero in the limit of $x \to 0$. This means that, contrary to what happens in two-component Fermi gases, the polaron-molecule transition is not masked by a phase separation region. Even if our QMC results seems to indicate the presence of a first order quantum phase transition between the two phases described above, we cannot exclude that, by improving the choice of the trial wave functions, the condensate fraction could vanish to zero and the phase separation region could eventually disappear.

Moreover we have observed a remarkable phenomenon, which can be defined as a Pauli exclusion effect on bosons, induced by the presence of the two Fermi surfaces. In the normal phase at zero-temperature, for bosonic concentrations x smaller than 0.5, i.e. when the number of the molecules is smaller than the number of unpaired fermions, the bosonic momentum distribution function is completely depleted for momenta smaller than a critical value. We believe that an experimental evidence of the Pauli exclusion on bosons could be found with the Bose-Fermi mixtures currently under study at the MIT [Heo12, Wu12].

Finally, the derivation of the spectral weight functions and dispersions carried out in this thesis' work, represents another important step in the exploration of resonant Bose-Fermi mixtures. Thanks to this calculation, derived within the T-matrix approximation at zero-temperature, a comparison with the experiments could be realized, by applying the radio-

frequency spectroscopy technique to probe the single-particle excitation spectrum and the energy dispersions of strongly-interacting Bose-Fermi mixtures.

In order to deeply understand the nature of the quantum phase transition and the effect of the boson-boson repulsion, further work is needed. The T-matrix results could be improved by developing a self-consistent calculation, while the QMC simulation could become more reliable by introducing an intermediate trial wavefunction between the two regimes. In conclusion the results obtained with this thesis' work open new interesting issues, that could be considered in the near future both from the theoretical and experimental point of view.

Bibliography

[Alb02] A. P. Albus, S. A. Gardiner, F. Illuminati, and M. Wilkens, *Quantum field theory of dilute homogeneous Bose-Fermi-mixtures at zero temperature*, Phys. Rev. A **65**, 053607 (2002).

[And75] J.B. Anderson, *A random-walk simulation of the Schrödinger equation:* H_3^+, The Journal of Chemical Physics, 63(4):1499, 1975.

[And95] M.H. Anderson, J.R. Ensher, M.R. Matthews, C.E. Wieman, and E.A. Cornell, *Observation of Bose-Einstein condensation in a dilute atomic vapor*, Science 269, 198 (1995).

[Ast04] G. Astrakharchik, J. Boronat, J. Casulleras, and S. Giorgini, *Equation of State of a Fermi Gas in the BEC-BCS Crossover: A Quantum Monte Carlo Study*, Phys. Rev. Lett., 93(20):200404, November 2004.

[Avd06] A. V. Avdeenkov, D. C. E. Bortolotti, and J. L. Bohn, *Stability of fermionic Feshbach molecules in a Bose-Fermi mixture*, Phys. Rev. A **74**, 012709 (2006).

[Bar08] X. Barillier-Pertuisel, S. Pittel, L. Pollet, and P. Schuck, *Boson-fermion pairing in Bose-Fermi mixtures on one-dimensional optical lattices*, Phys. Rev. A **77**, 012115 (2008).

[Ber12] G. Bertaina, E. Fratini, S. Giorgini, and P. Pieri, *Quantum Monte Carlo study of a resonant Bose-Fermi mixture*, arXiv:1211.6011 (2012).

[Bor08] D. C. E. Bortolotti, A. V. Avdeenkov, and J. L. Bohn, *Generalized Mean Field Approach to a Resonant Bose-Fermi Mixture*, Phys. Rev. A **78**, 063612 (2008).

[Bou88] J.P. Bouchaud, A. Georges, and C. Lhuillier, *Pair wave functions for strongly correlated fermions and their determinantal representation*, Journal de Physique, 49(4):553, 1988.

[Bra06] E. Braaten, H. W. Hammer, *Universality in few-body systems with large scattering length*, Phys. Rep. **428**, 259 (2006).

[Car03] J. Carlson, S.-Y. Chang, V.R. Pandharipande, and K.E. Schmidt, *Superfluid Fermi Gases with Large Scattering Length*, Phys. Rev. Lett., 91(5):050401, July 2003.

[Caz09] C. Cazorla, G. Astrakharchick, J. Casulleras, and J. Boronat, *Bose-Einstein Quantum Statistics and the Ground State of Solid 4He*, New J. Phys. **11**, 013047 (2009), 0804.1851.

[Cep77] D. Ceperley, G.V. Chester, and M.H. Kalos, *Monte Carlo simulation of a many-fermion study*, Phys. Rev. B, 16(7):3081, October 1977.

[Cep80] D.M. Ceperley and B.J. Alder. *Ground State of the Electron Gas by a Stochastic Method*, Physical Review Letters, 45(7):566, August 1980.

[Che06] F. Chevy, *Universal phase diagram of a strongly interacting Fermi gas with unbalanced spin populations*, Phys. Rev. A **74**, 063628 (2006).

[Com07] R. Combescot, A. Recati, C. Lobo and F. Chevy, *Normal State of Highly Polarized Fermi Gases: Simple Many-Body Approaches*, Phys. Rev. Lett. **98**, 120402 (2007).

[Com09] R. Combescot, S. Giraud, and X. Leyronas, *Analytical theory of the dressed bound state in highly polarized Fermi gases*, Europhys. Lett **88**, 60007 (2009).

[Cor12] M. Correggi, G. Dell'Antonio, D. Finco, A. Michelangeli, and A. Teta, *Stability for a System of N Fermions Plus a Different Particle with Zero-Range Interactions*, Rev. Math. Phys. 24, 1250017 (2012).

[Dav95] K.B. Davies, M.-O. Mewes, M.R. Andrews, N.J. van Druten, D.S. Durfee, D.M. Kurn, and W. Ketterle, *Bose-Einstein condensation in a gas of Sodium atoms* Phys. Rev. Lett. 75, 3969 (1995).

[Dic05] D. B. M. Dickerscheid, D. van Oosten, E. J. Tillema, and H. T. C. Stoof, *Quantum phases in a resonantly-interacting Bose-Fermi mixture*, Phys. Rev. Lett. **94**, 230404 (2005).

[Fet71] A. Fetter and J. D.Walecka, *Quantum theory of many-particle systems*, Mc-Graw Hill, New York (1971),

[Fra10] E. Fratini and P. Pieri, *Pairing and condensation in a resonant Bose-Fermi mixture*, Phys. Rev. A **81**, 051605 (2010).

[Fra12] E. Fratini and P. Pieri, *Mass imbalance effect in resonant Bose-Fermi mixtures*, Phys. Rev. A **85**, 063618 (2012).

[Gae10] J.P. Gaebler, J.T. Stewart, T.E. Drake, D.S. Jin, A. Perali, P. Pieri, and G.C. Strinati, *Observation of pseudogap behaviour in a strongly interacting Fermi gas*, Nature Phys.**6**, 569 (2010).

[Gio99] S. Giorgini, J. Boronat, and J. Casulleras *Ground state of a homogeneous Bose gas: A diffusion Monte Carlo calculation*, Phys. Rev. A, 60(6):5129, (1999)

[Gio08] S. Giorgini, L. Pitaevskii, and S. Stringari, *Theory of ultracold Fermi gases*, Rev. Mod. Phys. **80**, 1215 (2008)

[Gir12] S. Giraud and R. Combescot, *Interaction between polarons and analogous effects in polarized Fermi gases*, Phys. Rev. A **85**, 013605 (2012)

[Gua98] R. Guardiola, *Monte Carlo methods in quantum many-body theories*, Springer (1998).

[Gun06] K. Günter, T. Stoferle, H. Moritz, M. Kohl, and T. Esslinger, *Bose-Fermi mixtures in a Three dimensional Optical lattice*, Phys. Rev. Lett. **96**, 180402 (2006).

[Has70] W.K. Hastings, *Monte Carlo Sampling Methods Using Markov Chains and Their Applications*, Biometrika, 57(1):97, 1970.

[Han68] J.-P. Hansen and D. Levesque, *Ground State of Solid Helium-4 and -3* Phys. Rev. **165**, 293 (1968)

[Heo12] M.-S. Heo, T. T. Wang, C. A. Christensen, T. M. Rvachov, D. A. Cotta, J.-H. Choi, Y.-R. Lee, W. Ketterle, *Formation of Ultracold Fermionic NaLi Feshbach Molecules*, Phys. Rev. A **86**, 021602(R) (2012).

[Hol03] M. Holzmann, J. N. Fuchs, G. Baym, J. P. Blaizot, F. Laloë, *Bose-Einstein transition temperature in a dilute repulsive gas*, C. R. Physique **5**, 21 (2004).

[Isk07] M. Iskin and C. A. R. Sa de Melo, *Mixtures of ultracold fermions with unequal masses*, Phys. Rev. A **76**, 013601 (2007)

[Kag04] M.Y. Kagan *et al.*, *Composite fermions, trios, and quartets in a Fermi-Bose mixture*, Phys. Rev. A **70**, 023607 (2004).

[Kal62] M. Kalos, *Monte Carlo Calculations of the Ground State of Three-and Four-Body Nuclei*, Physical Review, 128(4):1791, November 1962.

[Kal70] M. Kalos, *Energy of a Boson Fluid with Lennard-Jones Potentials*, Physical Review A, 2(1):250, July 1970.

[Kal74] M. Kalos, D. Levesque, and L. Verlet,

Helium at zero temperature with hard-sphere and other forces, Physical Review A, 9(5):2178, May 1974.

[Kar07] O. I. Kartavtsev and A. V. Malykh, *Low-energy three-body dynamics in binary quantum gases*, J. Phys. B **40**, 1429 (2007).

[Lew04] M. Lewenstein, L. Santos, M. A. Baranov, and H. Fehrmann, *Atomic Bose-Fermi mixtures in an optical lattice*, Phys. Rev. Lett. **92**, 050401 (2004).

[Lin01] C. Lin, F. Zong, and D. Ceperley, *Twist-averaged boundary conditions in continuum quantum Monte Carlo algorithms*, Phys. Rev. E **64**, 016702 (2001).

[Liu03] X.-J. Liu, M. Modugno, and H. Hu, *Finite temperature effects on the collapse of trapped Bose-Fermi mixtures*, Phys. Rev. A **68**, 053605 (2003).

[Lud11] D. Ludwig, S. Floerchinger, S. Moroz, and C. Wetterich, *Quantum phase transition in Bose-Fermi mixtures*, Phys. Rev. A **84**, 033629 (2011).

[Lut60] J. M. Luttinger and J. C. Ward, *Ground-state energy of a many-fermion system*, Phys. Rev. **118**, 1417 (1960).

[Mar09] F. M. Marchetti, T. Jolicoeur, and M. M. Parish, *Stability and pairing in quasi-one-dimensional Bose-Fermi mixtures*, Phys. Rev. Lett. **103**, 105304 (2009).

[Mar08] F. M. Marchetti, C. J. M. Mathy, D. A. Huse, and M. M. Parish, *Phase separation and collapse in Bose-Fermi mixtures with a Feshbach resonance*, Phys. Rev. B **78**, 134517 (2008).

[Mas08] P. Massignan, G. M. Bruun, and H. T. C. Stoof, *Spin polarons and molecules in strongly interacting atomic Fermi gases*, Phys. Rev. A **78**, 031602(R) (2008).

[Mat11] C. J. M. Mathy, M. M. Parish, and D. A. Huse, *Trimers, Molecules and Polarons in Mass-Imbalanced Atomic Fermi Gases*, Phys. Rev. Lett. **106**, 166404 (2011).

[McM65] W. McMillan, *Ground State of Liquid ^4He*, Physical Review, 138(2A):A442, April 1965.

[Met53] N. Metropolis, A.W. Rosenbluth, M.N. Rosenbluth, A.H. Teller, and E. Teller, *Equation of State Calculations by Fast Computing Machines*, The Journal of Chemical Physics, 21(6):1087, 1953.

[Mod02] G. Modugno, G. Roati, F. Riboli, F. Ferlaino, R. J. Brecha, and M. Inguscio, *Collapse of a degenerate Fermi gas*, Science **297**, 2240 (2002).

[Mor09] C. Mora and F. Chevy, *Ground state of a tightly bound composite dimer immersed in a Fermi sea*, Phys. Rev. A **80**, 033607 (2009).

[Mor10] C. Mora and F. Chevy, *Normal Phase of an Imbalanced Fermi Gas*, Phys. Rev. Lett **104**, 230402 (2010).

[Ni08] K.-K. Ni, S. Ospelkaus, M. H. G. de Miranda, A. Pe'er, B. Neyenhuis, J. J. Zirbel, S. Kotochigova, P. S. Julienne, D. S. Jin, and J. Ye, *A high phase-space-density gas of polar molecules*, Science **322**, 231 (2008).

[Nos64] L. Nosanow, *Theory of Crystalline He^3 at 0° K*, Phys. Rev. Lett. **13**, 270 (1964)

[Osp06] C. Ospelkaus, S. Ospelkaus, L. Humbert, P. Ernst, K. Sengstock, and K. Bongs, *Ultracold heteronuclear molecules in a 3D optical lattice*, Phys. Rev. Lett. **97**, 120402 (2006).

[Osp06b] S. Ospelkaus, C. Ospelkaus, L. Humbert, K. Sengstock, and K. Bongs, *Tuning of heteronuclear interactions in a 3D optical lattice*, Phys. Rev. Lett. **97**, 120403 (2006).

[Osp06c] S. Ospelkaus, C. Ospelkaus, L. Humbert, K. Sengstock, and K. Bongs, *Interaction-Driven Dynamics of ^{40}K-^{87}Rb Fermion-Boson Gas Mixtures in the Large-Particle-Number Limit*, Phys. Rev. Lett. **96**, 020401 (2006).

[Pap06] S.B. Papp, C.E. Wieman, *Observation of Heteronuclear Feshbach Molecules from a $85^Rb - 87^Rb$ Gas*, Phys. Rev. Lett. 97, 180404 (2006).

[Par11] M. M. Parish, *Polaron-molecule transition in a two-dimensional Fermi gas*, Phys. Rev. A **83**, 051603 (2011).

[Park12] J. W. Park, C.-H. Wu, I. Santiago, T. G. Tiecke, S. Will, P. Ahmadi, and M. W. Zwierlein, *Quantum degenerate Bose-Fermi mixture of chemically different atomic species with widely tunable interactions*, Phys. Rev. A **85**, 051602 (2012).

[Pet04] D. Petrov, C. Salomon, and G. Shlyapnikov, *Weakly Bound Dimers of Fermionic Atoms*, Phys. Rev. Lett. **93**, 090404 (2004).

[Pie00] P. Pieri and G.C. Strinati, *Strong-coupling limit in the evolution from BCS conductivity to Bose-Einstein condensation*, Phys. Rev. B **61**, 15370 (2000).

[Pil08] S. Pilati and S. Giorgini, *Phase Separation in a Polarized Fermi Gas at Zero Temperature*, Phys. Rev. Lett., 100(3):030401, January 2008.

[Pil08b] S. Pilati, S. Giorgini and N. Prokof'ev, *Critical temperature of interacting Bose gases in two and three dimensions*, Phys. Rev. Lett. **100**, 140405 (2008).

[Pol08] L. Pollet, C. Kollath, U. Schollwöck, and M. Troyer, *Mixture of bosonic and spin-polarized fermionic atoms in an optical lattice*, Phys. Rev. A **77**, 023608 (2008).

[Pop87] V. N. Popov, *Functional Integrals and Collective Excitations*, Cambridge Univ. Press, Cambridge (1987), (see, e.g., chap. 6).

[Pow05] S. Powell, S. Sachdev, and H. P. Buchler, *Depletion of the Bose-Einstein condensate in Bose-Fermi mixtures*, Phys. Rev. B **72**, 024534 (2005).

[Pro08] N. V. Prokof'ev and B. V. Svistunov, *Bold diagrammatic Monte Carlo: A generic sign-problem tolerant technique for polaron models and possibly interacting many-body problems*, Phys. Rev. B **77**, 125101 (2008).

[Pun09] M. Punk, P. T. Dumitrescu, and W. Zwerger, *Polaron to molecule transition in a strongly imbalanced Fermi gas* Phys. Rev. A **80**, 053605 (2009).

[Rey82] P.J. Reynolds, *Fixed-node quantum Monte Carlo for molecules*, The Journal of Chemical Physics, 77(11):5593, 1982.

[Riz08] M. Rizzi and A. Imambekov, *Pairing of one-dimensional Bose-Fermi mixtures with unequal masses*, Phys. Rev. A **77**, 023621 (2008).

[Rot02] R. Roth and H. Feldmeier, *Mean-field instability of trapped dilute boson-fermion mixtures*, Phys. Rev. A **65**, 021603(R) (2002).

[Sch09] A. Schirotzek, , C.-H. Wu, A. Sommer, and M. W. Zwierlein, *Observation of Fermi Polarons in a Tunable Fermi Liquid of Ultracold atoms*, Phys. Rev. Lett. **102**, 230402 (2009).

[Sko56] G.V. Skorniakov and K.A. Ter-Martirosian, Zh. Eksp. Teor. Fiz. **31**, 775 (1956) [Sov. Phys. JETP **4**, 648 (1957)].

[Sim05] S. Simonucci, P. Pieri, and G.C. Strinati, *Broad vs. narrow Fano-Feshbach resonances in the BCS-BEC crossover with trapped Fermi atoms*, Europhys. Lett. **69**, 713 (2005).

[Song11] J.-L. Song and F. Zhou, *Anomalous Dimers in Quantum Mixtures near Broad Resonances: Pauli Blocking, Fermi Surface Dynamics and Implications*, Phys. Rev. A **84**, 013601 (2011).

[Ste08] J.T. Stewart, J.P. Gaebler and D.S. Jin, *Using photoemission spectroscopy to probe a strongly interacting Fermi gas*, Nature **454**, 744 (2008).

[Sto05] A. Storozhenko, P. Schuck, T. Suzuki, H. Yabu, and J. Dukelsky, *Boson-fermion pairing in a boson-fermion environment*, Phys. Rev. A **71**, 063617 (2005).

[Tan08] S. Tan, *Energetics of a strongly correlated Fermi gas* Ann. Phys. **323**, 2952 (2008); *Large momentum part of a strongly correlated Fermi gas*, *ibidem*, 2971 (2008).

[Tit09] I. Titvinidze, M. Snoek, and W. Hofstetter, *Generalized Dynamical Mean-Field Theory for Bose-Fermi Mixtures in Optical Lattices*, Phys. Rev. B **79**, 144506 (2009).

[Vei08] M. Veillette *et al.*, *Radio-frequency spectroscopy of a strongly imbalanced Feshbach-resonant Fermi gas*, Phys. Rev. A **78**, 033614 (2008).

[Viv00] L. Viverit, C.J. Pethick, and H. Smith, *Zero-temperature phase diagram of binary boson-fermion mixtures*, Phys. Rev. A **61**, 053605 (2000).

[Viv02] L. Viverit and S. Giorgini, *Ground state properties of a dilute Bose-Fermi mixture*, Phys. Rev. A **66**, 063604 (2002).

[Wat08] T. Watanabe, T. Suzuki, and P. Schuck, *Bose-Fermi pair correlations in attractively interacting Bose-Fermi atomic mixtures*, Phys. Rev. A **78**, 033601 (2008).

[Web08] C. Weber, G. Barontini, J. Catani, G. Thalhammer, M. Inguscio, and F. Minardi, *Association of ultracold double-species bosonic molecules*, Phys. Rev. A 78 (2008) 061601(R).

[Whi79] P.A. Whitlock, D.M. Ceperley, C.V. Chester, and M.H. Kalos, *The properties of liquid and solid 4He*, Phys. Rev. B **19**, 5598 (1979).

[Wu11] C.-H. Wu, I. Santiago, J. W. Park, P. Ahmadi, and M. W. Zwierlein, *Strongly Interacting Isotopic Bose-Fermi Mixture Immersed in a Fermi Sea*, Phys. Rev. A **84**, 011601 (2011).

[Wu12] C.-H. Wu, J. W. Park, P. Ahmadi, S. Will, M. W. Zwierlein, *Ultracold Fermionic Feshbach Molecules of* ^{23}Na-^{40}K, Phys. Rev. Lett. **109**, 085301 (2012).

[Yi01] X. X. Yi and C. P. Sun, *Phase separation of a trapped Bose-Fermi gas mixture: Beyond the Thomas-Fermi approximation*, Phys. Rev. A **64**, 043608 (2001).

[Yu10] Z. Yu, S. Zöllner and C. J. Pethick, *Comment on 'Normal Phase of an Imbalanced Fermi Gas'*, Phys. Rev. Lett. **105**, 188901 (2010).

[Yu11] Z.-Q Yu, S. Zhang and H. Zhai, *Stability condition of a strongly interacting boson-fermion mixture across an interspecies Feshbach resonance*, Phys. Rev. A **83**, 041603(R) (2011).

[Zir08] J. J. Zirbel, K.-K. Ni, S. Ospelkaus, J. P. D'Incao, C. E. Wieman, J. Ye, and D. S. Jin, *Collisional stability of Fermionic Feshbach molecules*, Phys. Rev. Lett. **100**, 143201 (2008).

E se dormiste, e se nel sonno sognaste,
e se nel sogno andaste in paradiso
e là coglieste un fiore strano e bellissimo
e se svegliandovi, aveste il fiore in mano?
Che direste allora?
S.T. Coleridge

Anche il viandante dal pendio della cresta del monte,
non porta a valle una manciata di terra,
terra a tutti indicibile, ma porta una parola conquistata,
pura, la genziana
gialla e blu. Forse noi siamo qui per dire: casa,
ponte, fontana, porta, brocca, albero da frutti, finestra,
al più: colonna, torre... Ma per dire comprendilo bene
oh, per dirle le cose così, che a quel modo, esse stesse,
nell'intimo,
mai intendevano d'essere.
R. M. Rilke, *Elegie duinesi, Nona elegia*

Ringraziamenti

Come il viandante che discende dal monte non porta con sé una manciata di terra ma una parola conquistata, anche io vorrei concludere questo percorso, scrivendo alcune parole conquistate. Saranno poche parole, qualche 'grazie' e solo qualche nome. Ma ogni grazie e ogni nome racchiudono una scoperta e una conquista. Forse siamo qui per dirle le cose, così, perché è in questo modo che gli diamo un significato.

In questi tre anni di dottorato mi sono accorta di avere un fiore strano e bellissimo in mano, ho fatto esperienza di questo fiore e ho tentato di conoscerlo e dargli un nome. Studiare e fare ricerca, pur nella limitatezza delle mie capacità e dei miei strumenti, rappresentano tra gli altri, il mio modo di dare importanza a questo fiore. Non sarà la fisica a dirmi se questo fiore viene o no dal paradiso, ma è anche con la fisica che riesco a cogliere la stranezza e la

bellezza del fiore che mi sono trovata in mano.
Grazie Pierbiagio Pieri, grazie Vincenzo Savona, grazie Gianluca Bertaina, grazie Stefano Giorgini. Con voi ho condiviso questo lavoro di ricerca. Voi mi avete seguita, aperto nuove strade, ascoltata, valorizzata. Mi avete insegnato tanto (anche che ho ancora tanto da imparare) e trasmesso la passione per la fisica (per questo non voglio smettere di imparare e sono contenta di continuare questo percorso). Grazie ad Andrea Guidini, perché lavorando insieme, mi sono scoperta anche io capace di insegnare e trasmettere qualcosa e ne ho compreso la bellezza.
Un grazie ugualmente importante è anche per chi non mi ha insegnato la fisica, ma mi ha insegnato tante altre cose. Grazie ai miei genitori Agnese ed Euro, perché ho sperimentato cosa significa avere qualcuno che mi vuole bene sempre.
Grazie ai miei amici. Siete stati i punti di riferimento, un'isola felice, una boa a cui aggrapparsi per tirare il fiato, la mia maschera da sub e il mio boccaglio, i riflessi dell'acqua, le correnti calde e fredde, le perle, i coralli e i pesci dalle mille forme e dai mille colori, in questo mare aperto, in cui mi sono buttata.